Fabrication and Characterization of Monocrystalline Sesquioxide Waveguide Lasers

Dissertation

zur Erlangung des Doktorgrades
des Departments Physik
der Universität Hamburg

vorgelegt von

Andreas Kahn

aus Hamburg

Hamburg
2009

Gutachter der Dissertation: Prof. Dr. G. Huber
Prof. Dr. D. Heitmann

Gutachter der Disputation: Prof. Dr. G. Huber
Priv.-Doz. Dr. V. M. Baev

Datum der Disputation: 21.10.2009

Vorsitzender des Promotionsausschusses: Dr. K. Petermann

Dekan der Fakultät für Mathematik,
Informatik und Naturwissenschaften: Prof. Dr. H. Graener

Abstract

ANDREAS KAHN:
Fabrication and Characterization of Monocrystalline Sesquioxide Waveguide Lasers

The development of integrated optical devices based on rare-earth doped sesquioxides is very promising for applications that require lasers with high frequency stability. Thus, the subject of this work is the fabrication of rare-earth doped sesquioxide waveguiding films by pulsed laser deposition (PLD) and their characterization as well as the realization of rib-channel waveguide lasers based on these films.

Nd^{3+} and Er^{3+} doped sesquioxide films with thicknesses of 1 to 3 µm were deposited on sapphire as well as sesquioxide substrates. The growth was monitored using reflection high-energy electron diffraction. The structure of the films was characterized by use of X-ray diffraction and atomic force microscopy, and their fluorescence lifetimes as well as their absorption and emission cross-sections were determined.

Highly-textured polycrystalline Sc_2O_3 and Y_2O_3 films with surface roughnesses as low as 2 nm and spectroscopic properties similar to those of bulk crystals were fabricated on sapphire substrates. Epitaxial two-dimensional growth up to a film thickness of 3 µm has been realized for lattice matched $(Gd, Lu)_2O_3$ films deposited on Y_2O_3 substrates. The surface structure of these monocrystalline films consists of nearly atomically flat terraces and step edges with typical heights of a single monolayer. The fluorescence lifetimes of the lattice matched $(Gd, Lu)_2O_3$ films are comparable to those of correspondingly doped Y_2O_3 bulk crystals, whereas their emission and absorption spectra are slightly broadened.

Using a newly developed loss-measurement technique, the propagation losses within the waveguiding films have been determined to be between 1.4 dB/cm and 14.8 dB/cm at wavelengths of approximately 800 nm. These relatively high losses can be explained by scattering at parasitic particulates, which typically occur during PLD.

Several films were structured by Ar-ion etching, resulting in 2 to 5 µm wide and 6 to 7 mm long rib-channel waveguides. Gain measurements performed with the 0.6 at.% doped $Er{:}(Gd, Lu)_2O_3$ rib-channel waveguides resulted in signal enhancements up to 5.9 dB/cm at 1536 nm upon in-band pumping at 1480 nm. While room-temperature continuous-wave laser emission at 1.58 µm has been demonstrated for a 0.2 at.% doped $Er{:}Sc_2O_3$ bulk crystal pumped at either 975 nm or 1536 nm, laser experiments performed with the Er^{3+} doped waveguides have not been successful.

Continuous-wave laser emission at 1075 nm and 1080 nm has however been realized with a monocrystalline $Nd(0.5\,at.\%){:}(Gd, Lu)_2O_3$ rib-channel waveguide upon pumping at 820 nm. The experiments were performed at room temperature and the waveguide end-facets were directly coated with reflective mirrors, which resulted in an output coupling of about 1 to 2 %. A laser threshold of 1 mW and a slope efficiency of 0.5 %, each with respect to the incident pump power, have been obtained. For an incident pump power of 410 mW, a maximum output power of 1.8 mW has been achieved. While the laser performance is yet to be improved, laser action has for the first time been demonstrated in a rare-earth doped sesquioxide waveguide.

Kurzfassung

Andreas Kahn:
Herstellung und Charakterisierung von einkristallinen Sesquioxid-Wellenleiterlasern

Die Entwicklung von integriert-optischen Bauelementen aus Seltenerd-dotierten Sesquioxiden ist vielverspechend für Anwendungen, die Laser hoher Frequenzstabilität erfordern. Gegenstand dieser Arbeit ist daher die Herstellung von Seltenerd-dotierten Sesquioxid-Wellenleiterschichten mittels *Pulsed Laser Deposition* (PLD) und deren Charakterisierung sowie ihre Verwendung für Rippenwellenleiter-Laser.

Nd^{3+}- und Er^{3+}-dotierte Sesquioxidschichten mit Schichtdicken von 1 bis 3 µm wurden sowohl auf Saphir- als auch auf Sesquioxid-Substrate aufgewachsen und das Wachstum mit *Reflection High-Energy Electron Diffraction* verfolgt. Die hergestellten Schichten wurden mittels Röntgendiffraktometrie und Rasterkraftmikroskopie untersucht. Weiterhin sind ihre Fluoreszenzlebensdauern sowie die Wirkungsquerschnitte für stimulierte Emission und Absorption bestimmt worden.

Auf Saphir-Substraten wurden hochtexturierte polykristalline Sc_2O_3- und Y_2O_3-Schichten mit Oberflächenrauigkeiten bis unter 2 nm hergestellt, deren spektroskopische Eigenschaften nahezu identisch mit denen von Volumeneinkristallen sind. Auf Y_2O_3-Substraten konnte hingegen zweidimensionales epitaktisches Schichtwachstum von gitterangepassten $(Gd,Lu)_2O_3$-Schichten realisiert werden. Die Oberflächenstruktur dieser bis zu 3 µm dicken einkristallinen Schichten besteht aus nahezu atomar glatten Terrassen, deren Stufenkanten typischerweise Höhen von nur einer Monolage aufweisen. Während die Fluoreszenzlebensdauern der gitterangepassten Schichten mit denen von entsprechend dotierten Y_2O_3-Volumeneinkristallen vergleichbar sind, zeigte sich eine leichte Verbreiterung ihrer Emissions- und Absorptionsbanden.

Die Wellenleiterverluste in den hergestellten Schichten wurden mittels einer eigens dafür entwickelten Messmethode bei Wellenlängen um 800 nm bestimmt. Die relativ hohen Verluste von 1,4 dB/cm bis 14,8 dB/cm werden auf Partikel zurückgeführt, die üblicherweise beim PLD-Prozess entstehen.

Mittels Ar-Ionen wurden in einige dieser Schichten 2 bis 5 µm breite und 6 bis 7 mm lange Rippenwellenleiter geätzt. Bei einer Wellenlänge von 1536 nm ist für einen 0,6 at.% dotierten $(Gd,Lu)_2O_3$-Streifenwellenleiter eine Signalerhöhung um 5,9 dB/cm durch Pumpen bei 1480 nm gemessen worden. Während mit einem Er(0,2 at.%):Sc_2O_3-Volumeneinkristall sowohl durch Pumpen bei 975 nm als auch bei 1536 nm Dauerstrichlaser mit Emissionswellenlängen von 1,58 µm realisiert worden sind, waren die Laserexperimente mit den Erbium-dotierten Wellenleitern nicht erfolgreich.

Mit einem einkristallinen Nd(0,5 at.%):$(Gd,Lu)_2O_3$ Rippenwellenleiter ist hingegen Lasertätigkeit im Dauerstrichbetrieb erzielt worden. Die Experimente wurden bei Raumtemperatur, mit direktverspiegelten Wellenleiterendflächen und einem Auskoppelgrad von ungefähr 1 bis 2 % durchgeführt. Der Laser emittierte bei Wellenlängen von 1075 nm und 1080 nm. Es ergab sich eine Schwellpumpleistung von 1 mW und ein differenzieller Wirkungsgrad von 0,5 %, jeweils bezogen auf die eingestrahlte Pumpleistung. Die maximale Ausgangsleistung betrug 1,8 mW bei einer eingestrahlten Pumpleistung von 410 mW. Während die Lasereffizienz noch zu steigern ist, ist hiermit erstmals Lasertätigkeit in einem Seltenerd-dotierten Sesquioxidwellenleiter erzielt worden.

Contents

List of Figures

List of Tables

1 Introduction

1.1 Motivation

Optical communications contribute significantly to coping with the exponentially increasing amount of data we are facing in the information society. Huge bandwidths can be achieved with optical signals, which possess extremely high carrier frequencies.[1] Furthermore, parallel transmission of several optical signals with different wavelengths in a single transmission medium is possible. By use of wavelength division multiplexing (WDM), a transfer rate of 32 Tb/s in a single fiber has recently been achieved [ATT09]. In order to maintain such high capacities, most of the signal processing should also be performed in the optical domain. Hence, the combination of multiple passive and active optical elements on a single substrate is advantageous, a concept which is termed integrated optics [Mil69].

A multitude of integrated optical devices has already been realized, most notably in semiconductors, which allow a monolithic integration of the components [Kor82, Hol98]. However, several applications require lasers with a high frequency stability. Thus, the employment of materials featuring small linewidths in their emission spectra are promising. One possible application for integrated optical devices based on such materials is in optical communications between satellites. Due to the reduced power consumption in comparison to the use of amplitude modulation, inter-satellite communications often rely on phase modulation [Dic01]. The transmitters are generally based on the master oscillator power amplifier (MOPA) principle; a single-mode laser with high frequency stability is amplified, resulting in a high-power diffraction-limited laser beam. Prior to amplification, the phase of the low-power signal is modulated, usually by use of integrated optical devices featuring high modulation rates. It is advantageous to employ master oscillators which are also based on integrated optics and thus allow for an excellent frequency stability. The resulting miniaturization is another significant advantage of such devices, as size is a critical parameter in satellite technology.

Rare-earth (RE) doped dielectric oxides are promising laser materials for that purpose, since their sharp emission peaks are advantageous for a stabilization of the laser frequency. As bulk crystals, dielectric oxides are well established host materials for the realization of lasers with high (peak) power. However, compared to the highly advanced deposition and structuring techniques for semiconductors, the fabrication techniques for crystalline dielectric integrated optical devices are not yet well developed. Hence, the deposition of thin dielectric oxide films with high crystallinity and high optical quality has been the first objective of this work. Pulsed laser deposition (PLD) was used for film preparation,

---

[1] The frequency of light in the C-band [Raj02] of single-mode optical fibers is approximately 200 THz, a frequency about 10^6 times higher than that of radio waves in the very-high-frequency (VHF) band [IEE03] used for electrical transmission.

since it is an extremely flexible method and suitable for the fabrication of complex oxide films [Rij97]. As film materials, RE doped sesquioxides have been chosen, due to their advantageous properties, such as their relatively low phonon energies among the oxides as well as their high thermal conductivities and damage thresholds.

Based on such dielectric films, planar waveguide lasers [Gil96, Mac07] can be realized and the films can be structured in order to fabricate integrated optical devices. The main objective of this work has been the realization of channel waveguide lasers based on RE doped sesquioxides. Due to two-dimensional light confinement in a waveguide channel, high pump intensities can be obtained with relatively low pump powers and an excellent mode overlap of pump and laser light is given. Thus, channel waveguide lasers generally exhibit high optical gain and a low laser threshold [Lal89, Fie91]. Although growth of RE doped sesquioxide films has been investigated by many groups in recent years [Gri08], laser action in such waveguides has not been reported prior to this work. Indeed, waveguide lasers based on dielectric binary oxide films have so far only been demonstrated with Ti:Al_2O_3 [Pol07] and Nd:Ta_2O_5 [Gri08].

1.2 Structure of this Thesis

This thesis has been realized within the European specific targeted research project *Photonic Integrated Devices in Activated Amorphous and Crystalline Oxides* (PI-OXIDE).[2] Several diploma theses [Gue07a, Han07, Fec07b, Hei09] are associated with this work, which is structured in three main parts.

First, in chapter 2, some basic concepts of waveguide theory as well as fundamental principles of the interaction of light with RE ions in ionic crystals are introduced. An overview of the investigated host and substrate materials as well as the RE dopants Nd^{3+} and Er^{3+} is given in chapter 3. Furthermore, first bulk-laser experiments proving the suitability of Er^{3+} doped sesquioxides as laser materials are described. Chapter 4 introduces the basic mechanisms of film growth and describes the film fabrication using PLD. The analytical techniques used for film characterization are treated in chapter 5.

In the second part of this thesis, the structural and spectroscopic characterization of the deposited films is described. Several combinations of film and substrate materials are investigated in section 6.1 regarding their suitability for the fabrication of crystalline waveguiding films by PLD. The spectroscopic properties of the Nd^{3+} and Er^{3+} doped films are examined in section 6.2 and compared to those of correspondingly doped bulk crystals.

The third part of this work deals with planar and channel waveguide experiments. In chapter 7, the structuring process and the end-facet polishing are outlined, rib-channel waveguiding is demonstrated and several waveguide properties, such as the losses and the gain are determined. Finally, in chapter 8, the laser experiments performed with the Nd^{3+} and Er^{3+} waveguides are described. A summary of the experimental results and an outlook on further improvements as well as possible experiments and devices are given in chapter 9.

---

[2] Sixth framework programme, contract number 017501

2 Fundamentals

2.1 Theory of Waveguiding

As outlined in the introduction, the realization of active integrated optical devices is very promising. Based on planar waveguides allowing light confinement in one dimension, more complex waveguiding structures can be realized by use of various structuring techniques. The basic concepts of waveguide theory are outlined in the following sections. A more detailed description is given in [Oka00].

2.1.1 Planar Waveguides

Ray-optical Treatment

The basic principle of a planar waveguide can be described by ray optics. Light confinement in a waveguiding layer is possible if the surrounding media possess lower refractive indexes. A schematic of a planar waveguide is displayed in Fig. 2.1.

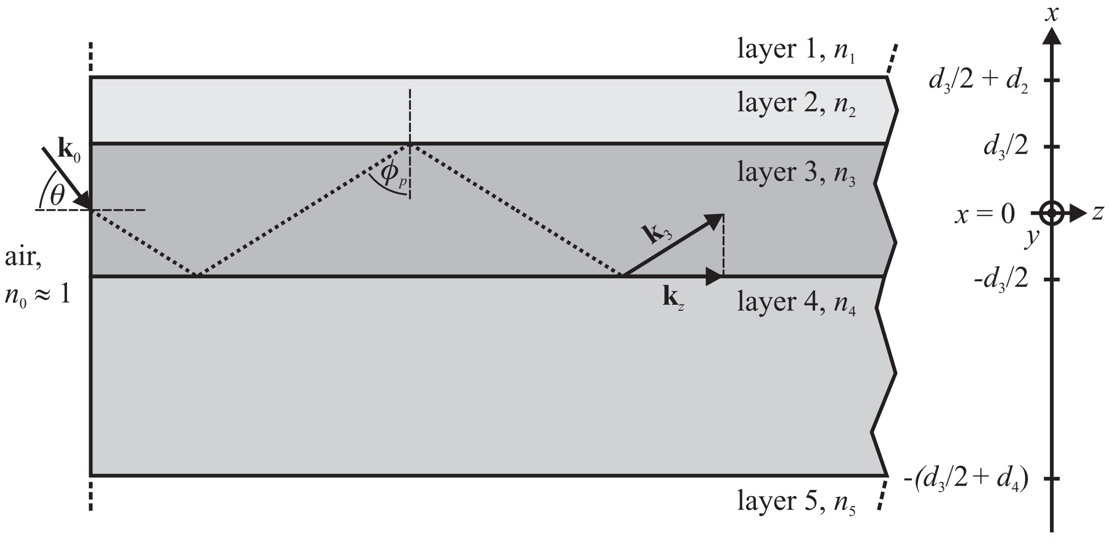

Figure 2.1: Profile view of a planar 5-layer waveguide. The waveguiding layer (layer 3) with thickness d_3 and refractive index n_3 is surrounded by media with lower refractive indexes n_m ($m = 0, 1, 2, 4, 5$).

For the following ray-optical description, only the waveguiding layer with refractive index n_3 and the two adjacent layers with lower refractive indexes n_2 and n_4 are considered.

At the interfaces between these layers, total internal reflection of light takes place for incidence angles ϕ_p between a critical angle ϕ_{crit} and $\pi/2$. The interface with the lower refractive index difference is considered when calculating ϕ_{crit}, since light confinement is limited by this interface. In the following, it is assumed that $n_4 \geq n_2$. The critical angle ϕ_{crit} can then be derived from Snell's law [Sal91] as follows:

$$\phi_{\text{crit}} = \arcsin\left(\frac{n_4}{n_3}\right) \tag{2.1}$$

In order to couple light from a medium with refractive index n_0 into the waveguide, as illustrated in Fig. 2.1, the incoupling angle θ may not exceed a critical angle

$$\theta_{\text{crit}} = \arcsin\left(\frac{\sqrt{n_3^2 - n_4^2}}{n_0}\right). \tag{2.2}$$

The product $n_0 \sin\theta_{\text{crit}}$ is defined as numerical aperture (NA) and depends only on the refractive indexes n_3 and n_4 of the waveguiding system:

$$\text{NA} := n_0 \sin\theta_{\text{crit}} = \sqrt{n_3^2 - n_4^2} \tag{2.3}$$

Wave-optical Treatment

As described in the previous section, light confinement by total internal reflection is possible for propagation angles ϕ_p between ϕ_{crit} and $\pi/2$. However, only a discrete number of modes is guided and ϕ_p takes discrete values. This can be explained by considering light as an electromagnetic field instead of rays. Light propagating in an isotropic charge-free medium with permittivity ϵ and permeability μ obeys the following Maxwell equations [Yar76]:

$$\nabla \cdot (\epsilon \mathbf{E}) = 0 \tag{2.4}$$

$$\nabla \times \mathbf{H} = \epsilon \frac{\partial}{\partial t} \mathbf{E} \tag{2.5}$$

$$\nabla \times \mathbf{E} = -\mu \frac{\partial}{\partial t} \mathbf{H} \tag{2.6}$$

$\mathbf{E}$ and $\mathbf{H}$ are the electric and magnetizing field, respectively. For a non-magnetizable medium with refractive index n, the following wave equation can be obtained [Bur02]:

$$\triangle \mathbf{E} = \left(\frac{n}{c_0}\right)^2 \frac{\partial^2}{\partial t^2} \mathbf{E} \tag{2.7}$$

Therein, c_0 is the speed of light in vacuum and t is the time.

In the following, this wave equation is solved for the different regions of a planar waveguide, consisting of five layers $m = 1, 2, 3, 4, 5$ with thicknesses d_m (in x-direction) and refractive indexes n_m:

$$n_3 > \max\{n_2, n_4\} \quad \wedge \quad n_2 \geq n_1 \quad \wedge \quad n_4 \geq n_5 \tag{2.8}$$

The layers are arranged as illustrated in Fig. 2.1 and are assumed to be of infinite dimension in y and z direction. The thicknesses d_1 and d_5 of the outer layers are assumed to be infinite as well. In order to solve Eq. (2.7), the ansatz of a time-harmonic electromagnetic wave propagating in z-direction is applied:

$$\begin{aligned}\mathbf{E}(x, y, z, t) &= \mathbf{E}'(x, y) \exp\left[i(\omega t - k_z z)\right] && (2.9)\\ \mathbf{H}(x, y, z, t) &= \mathbf{H}'(x, y) \exp\left[i(\omega t - k_z z)\right] && (2.10)\end{aligned}$$

The electromagnetic wave has a vacuum wavelength λ, angular frequency $\omega = 2\pi c_0/\lambda$ and the wave vector $\mathbf{k}_m$ in the layer m. $\mathbf{E}'$ and $\mathbf{H}'$ are the separated parts of $\mathbf{E}$ and $\mathbf{H}$ depending on x and y only. Since guided modes are considered and the transverse field profile of a guided mode remains constant during propagation in z-direction, the z-component $k_{z,m}$ of $\mathbf{k}_m$ is equal in all layers. Thus, the propagation constant $k_z := k_{z,m}$ of a waveguide mode is introduced. It defines the angle of propagation ϕ_p in the ray-optical model and vice versa:

$$\begin{aligned}k_z &= k_0\, n_{\text{eff}} && (2.11)\\ n_{\text{eff}} &:= n_3 \sin(\phi_p) && (2.12)\end{aligned}$$

Here, $k_0 = 2\pi/\lambda$ is the magnitude of $\mathbf{k}_0$, which is the wave vector of the incoming wave prior to coupling into the waveguide. With n_{eff}, an effective refractive index of the waveguide mode is introduced. Since all layers are of infinite dimension in y-direction, $\mathbf{E}$ and $\mathbf{H}$ are assumed to be independent of y. The following relations for the field components of $\mathbf{E}$ and $\mathbf{H}$ are obtained from the Maxwell equations (2.5) and (2.6) when considering the independency of the fields regarding y (substitution: $\partial/\partial y = 0$) as well as the harmonic dependencies in regard to z (substitution: $\partial/\partial z = -ik_z$) and regarding the time t (substitution: $\partial/\partial t = i\omega$):

$$\begin{aligned}E_y &= -\frac{\omega\mu}{k_z} H_x && (2.13)\\ -ik_z E_x - \frac{\partial E_z}{\partial x} &= -i\omega\mu H_y && (2.14)\\ \frac{\partial E_y}{\partial x} &= -i\omega\mu H_z && (2.15)\\ H_y &= \frac{\omega\epsilon}{k_z} E_x && (2.16)\\ -ik_z H_x - \frac{\partial H_z}{\partial x} &= i\omega\epsilon E_y && (2.17)\\ E_z &= -\frac{i}{\omega\epsilon}\frac{\partial H_y}{\partial x} && (2.18)\end{aligned}$$

The equations (2.13) and (2.15) contain only the field components E_y, H_x and H_z. Since the electric field is restricted to the transverse plane, they describe transverse electric (TE) modes. Similarly, the modes described by equations (2.16) and (2.18), which contain only the field components H_y, E_x and E_z, are called transverse magnetic (TM) modes. In the following, only TE modes are considered. TM modes can be treated in an analogous manner. By using the equations (2.13) and (2.15), the field components H_x and H_z of a TE mode can be derived, once E_y is known. The general solution for the electric field component

$$E_y(x,\, z,\, t) = E_y'(x) \exp\left[i(\omega t - k_z z)\right] \tag{2.19}$$

of a guided mode can be formed as in [Bur02]:

$$E_y'(x) = \begin{cases} E_1 \exp(ik_{x,1}x) \\ E_2 \exp(ik_{x,2}x) + E_2' \exp(-ik_{x,2}x) \\ E_3 \cos(k_{x,3}x + \Psi) \\ E_4 \exp(-ik_{x,4}x) + E_4' \exp(ik_{x,4}x) \\ E_5 \exp(-ik_{x,5}x) \end{cases} \quad \text{for} \quad \begin{cases} d_3/2 + d_2 \le x \\ d_3/2 \le x \le d_3/2 + d_2 \\ -d_3/2 \le x \le d_3/2 \\ -(d_3/2 + d_4) \le x \le -d_3/2 \\ x \le -(d_3/2 + d_4) \end{cases} \tag{2.20}$$

For the x-components $k_{x,m}$ of the wave vectors $\mathbf{k}_m$, one has the following relations:

$$k_{x,m} = k_0\, n_m \cos(\phi_p) = k_0 \sqrt{n_m^2 - n_{\text{eff}}^2} \tag{2.21}$$

Since $n_{\text{eff}} < n_3$, the constant $k_{x,3}$ is real and $E_y'(x)$ oscillates with x in the waveguiding layer. The constants $k_{x,1}$ and $k_{x,5}$, however, are imaginary and $E_y'(x)$ decays exponentially in the outer layers 1 and 5. The amplitudes E_1, E_2, E_2', E_3, E_4, E_4', E_5 and the phase Ψ can be determined as in [Bur02] by considering the continuity conditions of $E_y'(x)$ and $\partial E_y'(x)/\partial x$ at the interfaces between the layers as well as the intensity of the guided light. This also results in the *mode guidance condition equation* of a mode $p \in \mathbb{N}$ [Bur02]:

$$\begin{aligned} p\pi = k_{x,3}\, d_3 &- \arctan\left(\frac{k_{x,1}k_{x,2} + k_{x,2}^2 \tanh[-ik_{x,2}d_2]}{ik_{x,3}(k_{x,2} + k_{x,1}\tanh[-ik_{x,2}d_2])}\right) \\ &- \arctan\left(\frac{k_{x,4}k_{x,5} + k_{x,4}^2 \tanh[-ik_{x,4}d_4]}{ik_{x,3}(k_{x,4} + k_{x,5}\tanh[-ik_{x,4}d_4])}\right) \end{aligned} \tag{2.22}$$

The waveguiding films produced in the framework of this thesis were deposited on substrates with thicknesses of 0.5 mm, which exceed the wavelength of the guided near-infrared light by several orders of magnitude. The substrate is thus approximated to be infinitely thick ($\tanh[-ik_{x,4}d_4] \approx 1$) and Eq. (2.22) is simplified to describe a 4-layer waveguide:

$$p\pi = k_{x,3}\, d_3 - \arctan\left(\frac{k_{x,1}k_{x,2} + k_{x,2}^2 \tanh[-ik_{x,2}d_2]}{ik_{x,3}(k_{x,2} + k_{x,1}\tanh[-ik_{x,2}d_2])}\right) - \arctan\left(\frac{k_{x,4}}{ik_{x,3}}\right) \tag{2.23}$$

In case of waveguides without top cladding ($d_2 = 0$), one has a 3-layer structure and the *mode guidance condition equation* can be further simplified:

$$p\pi = k_{x,3}\, d_3 - \arctan\left(\frac{k_{x,1}}{ik_{x,3}}\right) - \arctan\left(\frac{k_{x,4}}{ik_{x,3}}\right) \tag{2.24}$$

Applying the relations (2.21) to substitute the constants $k_{x,m}$ in the *mode guidance condition equation*, it can be solved numerically and the number of guided modes as well as the effective refractive index n_{eff} of a mode p can be determined. Once n_{eff} is known, the field components of the mode can be calculated, as described in [Bur02].

2.1.2 Channel Waveguides

While the one-dimensional light confinement in planar waveguides can already result in quite high light intensities and a good overlap between pump and laser modes, light confinement in two dimensions is required for most integrated optical devices. This requirement can be fulfilled by several types of waveguide structures fabricated with different methods, such as ion implantation [Sta72], direct laser writing [Dav96] and various etching techniques [Leh86]. In the framework of this thesis, rib-channel waveguides were investigated, which were fabricated by reducing the thickness of a waveguiding film at certain regions. Elevated stripes remain, such as those displayed in Fig. 7.1. Light confinement below and within these stripes (see Fig. 7.4) can be explained by the effective index method described in [Oka00]. It allows an analytical treatment of the guided modes by introducing an effective refractive index profile. Since the effective refractive index below the stripes is higher than in the other film regions, light confinement in two dimensions is possible. The intensity distributions within the rib-channel waveguides investigated in this work were simulated by use of the software *FieldDesigner* developed by *PhoeniX BV*. It is based on numerical methods, such as the finite element method (FEM) described in [Oka00].

2.2 Rare-Earth Ions

The emphasis of this work was put on active waveguides for laser applications. Therefore, waveguiding films doped with the common laser ions Nd^{3+} and Er^{3+} were investigated. These ions belong to the lanthanides, which consist of the elements with the atomic numbers 57 (lanthanum) to 71 (lutetium). The electron configuration is of the form $[\text{Xe}](4f)^m(5d)^x(6s)^2$. Except for lanthanum ($m = 0$), gadolinium ($m = 7$) and lutetium ($m = 14$) for which x equals 1, m runs from 2 (cerium) to 14 (ytterbium) and x is 0. In general, lanthanides are incorporated into a crystal matrix in their trivalent form with the electron configuration $[\text{Xe}](4f)^{m+x-1}$. Due to their completely filled $5s$ and $5p$ shells, the $4f$ electrons are effectively shielded from the crystal field. Therefore, the crystal field has only a small influence on the $4f$ energy levels and the intraconfigurational $4f$-$4f$ transitions possess quite narrow linewidths [Hen89]. Furthermore, the $4f$ energy levels can be derived from those of the free ion, with the influence of the crystal field added as a small perturbation. This approach is described in the following.

2.2.1 Energy Levels of Free Ions

The electronic states of a free ion possessing a nuclear charge $Z \cdot e$ as well as N electrons of mass m_e and charge $-e$ can be derived by solving the Schrödinger equation with the following Hamiltonian[1]:

$$H = \sum_{i=1}^{N} \left(-\frac{\hbar^2}{2m_e} \nabla^2_{r_i} - \frac{Ze^2}{4\pi\varepsilon_0 r_i} \right) + \sum_{i<j=1}^{N} \frac{e^2}{4\pi\varepsilon_0 r_{ij}} \tag{2.25}$$

Here, h is the Planck constant and one has $\hbar = h/2\pi$. The distance between the electron i and the nucleus is r_i, and $r_{ij} = |\mathbf{r}_i - \mathbf{r}_j|$ is the distance between the electrons i and j. H consists of three parts, the kinetic energy of the electrons, their energy in the nuclear potential, and a part describing the electrostatic repulsion between them. All spin-orbit and spin-spin interactions as well as other small corrections have been neglected so far, but can later be incorporated as perturbations.

Due to the term describing the electron-electron interaction, a separation in N one-particle problems and thus an analytical solution of the Schrödinger equation is impossible. Therefore, the central field approximation can be made. Each electron is assumed to be situated in an effective spherically symmetric potential $V(r_i)$, describing the nuclear potential and the shielding by the remaining $(N-1)$ electrons. The resulting Hamiltonian H_0 is now separable.

$$H_0 = \sum_{i=1}^{N} \left(-\frac{\hbar^2}{2m_e} \nabla^2_{r_i} + V(r_i) \right) \tag{2.26}$$

Thus, a solution of the time independent Schrödinger equation

$$H_0 \Psi_0 = E_0 \Psi_0 \tag{2.27}$$

can be found by applying the Hartree-Fock method [Bra03]. The resulting wave function Ψ_0 can be written as Slater determinant of one-electron states $u_{\alpha,\beta,\ldots,\nu}(q_i)$. Each $\alpha, \beta, \ldots, \nu$ represents all four quantum numbers $(n,\ l,\ m_l,\ m_s)$ of an independent electronic state. The space and spin coordinates of the electron i are represented as q_i.

$$\Psi_0(q_1, q_2, ..., q_N) = \frac{1}{\sqrt{N!}} \sum_P \mathrm{sign}(P)\, P\, u_\alpha(q_1)\, u_\beta(q_2) \ldots u_\nu(q_N) \tag{2.28}$$

All possible permutations P of the coordinates q_i have to be considered in the summation, with sign(P) equaling $+1$ for even and -1 for odd permutations. The eigenvalue E_0 of the Hamiltonian H_0 in the central field approximation is the sum of the one-electron energies

---

[1] The equations in this section can be found in a similar notation in various textbooks of atomic physics, for example [Bra03].

$E_{n_i l_i}$. These energy eigenvalues depend only on the main quantum number n_i as well as the quantum number of the orbital angular momentum l_i. They are degenerated with respect to the magnetic m_l and spin quantum number m_s.

The non spherically symmetric part H_{ee} of the electron-electron interaction, as well as the spin-orbit coupling H_{so} of the electrons with spins $\mathbf{s}_i$ and orbital angular momenta $\mathbf{l}_i$ can be incorporated into the model as perturbations.

$$H_{ee} = \sum_{i<j=1}^{N} \frac{e^2}{4\pi\varepsilon_0 r_{ij}} - \sum_{i=1}^{N} \left(\frac{Ze^2}{4\pi\varepsilon_0 r_i} + V(r_i) \right) \tag{2.29}$$

$$H_{so} = \sum_{i=1}^{N} \frac{1}{2m_e^2 c^2} \cdot \frac{1}{r_i} \cdot \frac{dV(r_i)}{dr_i} \cdot (\mathbf{l}_i \cdot \mathbf{s}_i) \tag{2.30}$$

Other perturbations like spin-spin and orbit-orbit interactions, or perturbations resulting from the finite mass, dimension and magnetic dipole moment of the nucleus are some orders of magnitude smaller than H_{ee} and H_{so}, and can thus be neglected. More crucial is the influence of the crystal field, which will be discussed in section 2.2.2.

The relative strength of the corrections incorporated by H_{ee} and H_{so} defines the character of coupling between spins and orbital angular momenta.

One extreme is termed jj-coupling, being characterized by the domination of H_{so}. The spin and orbital angular momentum of each electron first couple to the individual angular momentum $\mathbf{j}_i = \mathbf{s}_i + \mathbf{l}_i$ and then result in a total angular momentum $\mathbf{J} = \sum_i \mathbf{j}_i$. The opposite case is termed LS coupling or Russel-Saunders coupling. H_{ee} being the dominant part, the individual spins and orbital angular momenta couple to the total spin $\mathbf{S} = \sum_i \mathbf{s}_i$ and total orbital angular momentum $\mathbf{L} = \sum_i \mathbf{l}_i$, respectively, before resulting in the total angular momentum $\mathbf{J} = \mathbf{L} + \mathbf{S}$.

For the lanthanides both corrections are of about the same order of magnitude, resulting in an intermediate coupling scheme. The eigenstates can be interpreted as linear combinations of different LS-states with the same quantum number J. It is common to label them as ${}^{2S+1}L_J$, following the Russel-Saunders approximation.

2.2.2 Influence of the Crystal Field

The degeneracy regarding the magnetic quantum number M_J of the free lanthanide ion is repealed, as its spherical symmetry is destroyed by the interactions of the $4f$-electrons with the electrostatic field of the ligands. This so-called Stark effect (see [Bra03]) can be described by the Hamiltonian

$$H_{\text{Stark}} = -e \sum_{k=1}^{N} \mathbf{E}(\mathbf{r}_k) \cdot \mathbf{r}_k, \tag{2.31}$$

representing the influence of the local electric field $\mathbf{E}$. Incorporating H_{Stark} as perturbation results in a Stark splitting of the $^{2S+1}L_J$ levels. For lanthanide ions with an odd number of optical electrons the theorem of Kramers asserts a splitting in $(2J + 1)/2$ twofold degenerate Stark levels. This is the case for the ions Nd^{3+} and Er^{3+}, which are investigated in this thesis. For lanthanide ions possessing an even number of optical electrons, the degeneracy in respect of M_J is completely nullified and a splitting in $(2J + 1)$ levels occurs. An overview of the energy levels of Nd^{3+} and Er^{3+} doped sesquioxides is given in section 3.2.

2.3 Radiative Transitions

This section discusses some aspects of the interaction between radiation and the active ions in a crystal lattice. The phenomena of absorption as well as spontaneous and stimulated emission are introduced and described by rate equations.

2.3.1 Absorption and Emission

An ion occupying a level with energy E_1 can be excited to a level with higher energy E_2 by absorption of a photon possessing an energy $E_\gamma = h\nu$ equal to $E_2 - E_1$. An excited ion can also spontaneously decay into a lower level by emission of a photon possessing the energy difference between the two levels. The emission of a photon by an excited ion can as well be stimulated by the presence of another photon with an energy corresponding to the transition. In this case the emitted photon not only possesses the same frequency ν as the original one, but also the same direction of propagation, polarization and phase. The processes mentioned above can be described by rate equations.[2]

Energy levels i with populations[3] N_i and the time derivatives (dN_i/dt) related to the rates of absorption, spontaneous emission and stimulated emission are considered. The decay rate of an energy level due to spontaneous emission is proportional to its population and the positive Einstein coefficient A:

$$\left(\frac{dN_i}{dt}\right)_{\text{sp}} = -A\,N_i \tag{2.32}$$

From A, the radiative lifetime $\tau_{\text{rad}} = 1/A$ of the energy level can be derived. Equation (2.33) describes the stimulated processes of absorption and emission:

$$\left(\frac{dN_i}{dt}\right)_{\text{st}} = -W_{ij}\,N_i \tag{2.33}$$

---

[2] In this section, merely an overview is given and the notations used within this thesis are introduced. A more detailed description of the above mentioned processes, the corresponding rate equations and the laser principle is given in [Sve98].

[3] N_i denotes the number of ions per unit volume occupying the energy level i.

W_{ij} is the stimulated rate of the transition $i \to j$ from the level i with energy E_i to the level j with energy E_j. The process is termed absorption for $E_i < E_j$ and stimulated emission for $E_i > E_j$. In contrast to the rate of spontaneous emission A, the stimulated rates W_{ij} do not only depend on the particulate transition, but also on the intensity I of the incident electromagnetic wave:

$$W_{ij} = g_j \, \sigma_{ij} \, F \tag{2.34}$$

$F = I/h\nu$ is the photon flux of the wave and g_j the degeneracy of the level j. The coefficients σ_{ij} are called emission or absorption cross-sections, depending on whether the process is absorption or stimulated emission. It has been shown in [Ein16] that:

$$g_i \, W_{ij} = g_j \, W_{ji} \tag{2.35}$$

W_{ij} and W_{ji} are the stimulated rates of the transitions between the energy levels i and j, which are g_i-fold and g_j-fold degenerate, respectively. From the equations (2.34) and (2.35) follows:

$$\sigma_{ij} = \sigma_{ji} \tag{2.36}$$

In the following, these cross sections, which are equal for absorption and stimulated emission, are termed atomic cross-sections σ_{at}.

2.3.2 Effective Cross-Sections

Since most of the investigated radiative transitions take place between two different manifolds consisting of thermally coupled Stark levels, it is practical to introduce effective absorption σ_{abs} and emission cross-sections σ_{em}, by taking the populations of the different Stark levels according to Maxwell-Boltzmann statistics into account. The effective cross-sections can be derived from the corresponding atomic cross-sections σ_{at} by incorporating the degeneracies g_{l} and g_{u} as well as the Boltzmann factors f_{l} and f_{u} of the lower and upper Stark level, respectively:

$$\sigma_{\mathrm{abs}} = f_{\mathrm{l}} \, g_{\mathrm{u}} \, \sigma_{\mathrm{at}} \tag{2.37}$$

$$\sigma_{\mathrm{em}} = f_{\mathrm{u}} \, g_{\mathrm{l}} \, \sigma_{\mathrm{at}} \tag{2.38}$$

The Boltzmann factor for $f_{m,n}$ for a $g_{m,n}$-fold degenerate Stark level n within a manifold m is, according to Maxwell-Boltzmann statistics,

$$f_{m,n} = \frac{g_{m,n} \, \exp\left(-\frac{E_{m,n}}{k_{\mathrm{B}} T}\right)}{Z_m}. \tag{2.39}$$

T is the temperature, k_B the Boltzmann constant, and $E_{m,n}$ the energy of the Stark level with respect to the lowest Stark level of all considered manifolds. The partition function Z_m of the manifold m is obtained by summing over all Stark levels i within m as follows:

$$Z_m = \sum_i g_{m,i} \exp\left(-\frac{E_{m,i}}{k_\mathrm{B}T}\right) \tag{2.40}$$

By introducing effective cross-sections, the equations (2.33) and (2.34) can be applied to entire manifolds:

$$\begin{aligned} \left(\frac{dN_\mathrm{l}}{dt}\right)_\mathrm{abs} &= -W_\mathrm{abs}(\lambda)\, N_\mathrm{l} && (2.41)\\ \left(\frac{dN_\mathrm{u}}{dt}\right)_\mathrm{em} &= -W_\mathrm{em}(\lambda)\, N_\mathrm{u} && (2.42) \end{aligned}$$

$$\begin{aligned} W_\mathrm{abs}(\lambda) &= \sigma_\mathrm{abs}(\lambda)\, F && (2.43)\\ W_\mathrm{em}(\lambda) &= \sigma_\mathrm{em}(\lambda)\, F && (2.44) \end{aligned}$$

N_l and N_u denote the total populations of the lower and upper manifold, respectively. $W_\mathrm{abs}(\lambda)$ and $W_\mathrm{em}(\lambda)$ are the effective rates for absorption and emission of radiation with the wavelength λ.

McCumber Relation

From the equations (2.37) to (2.40) follows a correlation[4] between the effective absorption and emission cross sections of transitions between two different manifolds consisting of thermally coupled Stark levels:

$$\sigma_\mathrm{em}(\lambda) = \sigma_\mathrm{abs}(\lambda)\, \frac{Z_\mathrm{l}}{Z_\mathrm{u}} \exp\left(-\frac{hc_0}{\lambda \cdot k_\mathrm{B}T}\right) \tag{2.45}$$

Z_l and Z_u are the partition functions of the lower and upper manifold, respectively. If those partition functions are known, Eq. (2.45) allows to derive the emission spectra of transitions between the two manifolds from the corresponding absorption spectra and vice versa.

---

[4] The correlation is based on [McC64] and thus termed McCumber relation.

2.3.3 Absorption and Gain Coefficients

In order to describe the effect of absorption and emission on the photon flux F of a plane wave propagating in z-direction through a medium, a two-level system is considered. N_l and N_u are the populations of the lower and upper energy level, respectively. Considering stimulated emission and absorption only, the infinitesimal change dF of the photon flux along the infinitesimal length dz can be described as follows [Sve98]:

$$dF = (W_\mathrm{em}(\lambda)\, N_\mathrm{u} - W_\mathrm{abs}(\lambda)\, N_\mathrm{l})\, dz \tag{2.46}$$

With the equations (2.43) and (2.44), the following relation is obtained:

$$dF = F\,(\sigma_\mathrm{em}(\lambda)\, N_\mathrm{u} - \sigma_\mathrm{abs}(\lambda)\, N_\mathrm{l})\, dz \tag{2.47}$$

By introducing an absorption coefficient $\alpha_\mathrm{abs}(\lambda)$ and a gain coefficient $g(\lambda)$

$$\begin{aligned} \alpha_\mathrm{abs}(\lambda) \quad &:= \quad \sigma_\mathrm{abs}(\lambda)\, N_\mathrm{l} - \sigma_\mathrm{em}(\lambda)\, N_\mathrm{u} &(2.48)\\ g(\lambda) \quad &:= \quad \sigma_\mathrm{em}(\lambda)\, N_\mathrm{u} - \sigma_\mathrm{abs}(\lambda)\, N_\mathrm{l}, &(2.49) \end{aligned}$$

Eq. (2.47) becomes

$$dF = -\alpha_\mathrm{abs}(\lambda) F dz = g(\lambda) F dz. \tag{2.50}$$

Since the coefficients $\alpha_\mathrm{abs}(\lambda)$ and $g(\lambda)$ depend on the populations N_l and N_u, they are generally also depending on the intensity I of the electromagnetic wave. However, for ground state absorption and very low intensities, the population of the upper energy level can often be neglected ($N_\mathrm{u} \approx 0$) and the population of the lower level can be approximated to be equal to the total density N_t of active ions. Eq. (2.48) can then be simplified to

$$\alpha_\mathrm{abs}(\lambda) = \sigma_\mathrm{abs}(\lambda)\, N_\mathrm{t}. \tag{2.51}$$

In this case, $\alpha_\mathrm{abs}(\lambda)$ is independent of the intensity and solving[5] Eq. (2.50) results in Beer-Lambert's law:

$$I(\lambda,\, z) = I(\lambda, 0)\, \exp\left[-\alpha_\mathrm{abs}(\lambda)\, z\right] \tag{2.52}$$

---

[5] For this, the photon flux was substituted by $F = I/h\nu$.

2.3.4 Selection Rules

Possible excitations of the lanthanide ions by an oscillating electromagnetic field can be of electric dipole, magnetic dipole or higher order character. Due to their marginal transition probabilities, higher order transitions can usually be neglected [Die68].

According to the Laporte selection rule [Bra03], magnetic dipole transitions are only possible between electron states of the same parity, while electric dipole transitions require a change of parity. Due to the inversion symmetry of the free lanthanide ion, its wavefunctions possess a defined parity and Laporte's rule has to be strictly satisfied. Since all $4f$-electrons are of the same parity, all electric $4f$-$4f$ dipole transitions are parity forbidden. Thus, the generally weaker magnetic dipole transitions, which are parity permitted for all $4f$-$4f$ transitions, become relevant.

The inversion symmetry can, however, be repealed by the crystal field,[6] resulting in states of mixed parity [Die68]. Between such states *forced electric dipole transitions* are permitted, obeying the following selection rules [Kam90]:

- $\Delta l = \pm 1$
- $\Delta S = 0$
- $|\Delta L| \leq 2l = 6$
- $|\Delta J| \leq 2l = 6$

The selection rules for magnetic dipole transitions are the following [Kam90]:

- $\Delta l = 0$
- $\Delta S = 0$
- $\Delta L = 0$
- $|\Delta J| \leq 1 \quad (J = 0 \nrightarrow J' = 0)$

Due to the effective shielding of the $4f$-electrons from the crystal field by the $5s$ and $5p$ electrons, the admixing of states with different parity is quite low. Therefore, the electrical dipole $4f$-$4f$ transitions are only weakly permitted and most $4f$ states possess quite high lifetimes.

---

[6] This effect is considerably small for the C_{3i}-sites of the sesquioxide lattice, showing inversion symmetry, as compared to the C_2-sites without center of symmetry.

3 Waveguide and Laser Materials

Various material systems were investigated regarding their suitability to produce active planar waveguides by pulsed laser deposition. Rare-earth (RE) doped sesquioxides were chosen as film material due to their advantageous properties outlined in the introduction. To allow light confinement in the film, a substrate material with lower refractive index had to be used. The Sellmeier equations of the employed materials, which describe the wavelength dependance of the refractive index, are summarized in Tab. 3.1.

Material	Sellmeier equation	$n(\lambda=0.80)$	$n(\lambda=1.08)$	$n(\lambda=1.55)$
Sc_2O_3	$n^2 = 3.8325 + \frac{0.0493}{\lambda^2 - 0.0238} - 0.0141\,\lambda^2$	1.976	1.964	1.954
Y_2O_3	$n^2 = 3.5387 + \frac{0.0422}{\lambda^2 - 0.0243} - 0.0091\,\lambda^2$	1.898	1.888	1.880
Lu_2O_3	$n^2 = 3.6200 + \frac{0.0413}{\lambda^2 - 0.0239} - 0.0086\,\lambda^2$	1.919	1.909	1.902
Gd_2O_3	$n^2 = 1 + \frac{\lambda^2}{0.364402\,\lambda^2 - 0.0075356}$	1.959	1.948	1.941
α-Al_2O_3	$n_o^2 = 1.5586 + \frac{1.5237\,\lambda^2}{\lambda^2 - 0.0110} + \frac{5.3604\,\lambda^2}{\lambda^2 - 325.66}$	1.760	1.754	1.746
	$n_e^2 = 1.7811 + \frac{1.2762\,\lambda^2}{\lambda^2 - 0.0124} + \frac{0.3394\,\lambda^2}{\lambda^2 - 17.03}$	1.752	1.745	1.734

Table 3.1: Sellmeier equations [Mix99, Bur02, Liu07] for the employed film and substrate materials, as well as the resulting refractive indexes n at various wavelengths λ (in µm). Due to its hexagonal structure, α-Al_2O_3 possesses an ordinary ($n_o \perp$ c-axis) and an extraordinary ($n_e \parallel$ c-axis) refractive index.

In this chapter, the film and substrate materials used for waveguide fabrication as well as the investigated RE dopants are introduced. Afterwards, an overview of laser experiments demonstrating the suitability of Nd^{3+} and Er^{3+} doped sesquioxides as laser materials is given.

3.1 Host and Substrate Materials

3.1.1 Sesquioxides

Sesquioxides are oxide materials with an anion to cation ratio of one and a half (lat. sesqui). The waveguiding films produced in the framework of this thesis consisted of rare-earth sesquioxides, particularly Sc_2O_3, Y_2O_3, Gd_2O_3 and Lu_2O_3. Possessing high thermal conductivities, high damage thresholds, and low phonon energies among the oxides, these sesquioxides are excellent host materials for RE based lasers [Pet07].

At room temperature, the above mentioned sesquioxides crystalize in the cubic C-type Bixbyite structure of the body centered space group $Ia3$ [Gme74]. For Sc_2O_3 and Lu_2O_3, the cubic form is stable up to the melting point. However, Y_2O_3 possesses a hexagonal high temperature phase above 2580 K [Gme74] and Gd_2O_3 changes to a monoclinic form at temperatures above 1530 K [Ric69]. The temperature of the Gd_2O_3 phase transition can be increased if the Gd^{3+} ion is partially substituted by a smaller ion [Cos08]. This is the case for the mixed systems $(Gd, Lu)_2O_3$ and $(Gd, Sc)_2O_3$, which were investigated within this work. The above mentioned sesquioxides can be used as both substrate and film material. However, Gd_2O_3 bulk crystals and thus substrates were not available in the cubic form.[1] While the growth of C-type yttria bulk crystals was possible, small angle grain boundaries, which are most probably caused by phase transitions during crystal growth, resulted in a bad quality of the employed Y_2O_3 substrates.[2] Gd_2O_3 was used as a component in mixed sesquioxide films only. Since the deposition temperatures[3] did not reach the temperature of the phase transition and the cubic form was supported by the substrate structure, only C-type Gd_2O_3 is considered.

Therefore, all investigated sesquioxides are expected to appear in the Bixbyite structure, composed of unit cells containing 16 formula units and a total of 80 atoms [Pau30]. The 32 sixfold oxygen coordinated trivalent cations are situated in two different symmetry sites: 24 sites with C_2 symmetry ($\parallel \langle 100 \rangle$) and 8 sites with C_{3i} symmetry ($\parallel \langle 111 \rangle$). Bonding between the cations and surrounding oxygen ions is mostly ionic with a small covalent contribution.

3.1.2 Sapphire

In addition to the sesquioxides, sapphire was also used as a substrate material. The term sapphire refers to the α-form of undoped Al_2O_3, also known as corundum. Its crystal structure consists of unit cells with trigonal symmetry, each containing two Al_2O_3 units. Alternatively it can be represented as a hexagonal close-packed (hcp) structure of oxygen ions with Al^{3+} ions located in the octahedrally coordinated interstices.

As shown in [Bur02, Bae04, Kuz06] and discussed in section 6.1.1, sapphire is a suitable substrate material for sesquioxide film growth. It offers a wide transparency range, high thermal conductivity, high mechanical as well as chemical stability, and is available at a relatively low cost. Since its refractive index is significantly lower than that of the above mentioned sesquioxides, waveguides with a high NA can be realized by using sapphire as substrate material.

---

[1] Due to the relatively low temperature of the phase transition to the monoclinic form, C-type Gd_2O_3 could not be grown from the melt.

[2] An overview of the relevant phase transitions is given in [Pet09] and the quality of the Y_2O_3 bulk crystals is investigated in [Sch09].

[3] The deposition temperature indicates the substrate temperature obtained by laser heating. An increase of the actual surface temperature for very short time intervals during impact of the ablated material was neglected.

3.1.3 Material Properties

Several important properties of the materials discussed above are summarized in Tab 3.2.

Material	Sc_2O_3	Y_2O_3	Lu_2O_3	Gd_2O_3	α-Al_2O_3
Crystal structure	cubic	cubic	cubic	cubic	hexagonal
Space group	$Ia3$	$Ia3$	$Ia3$	$Ia3$	$R\bar{3}c$
Lattice constants (Å)	9.857	10.603	10.391	10.818	$a = 4.761$ $c = 12.996$
Density ($\frac{\mathrm{g}}{\mathrm{cm}^3}$)	3.85	5.03	9.42	7.61	3.99
Density of RE cations ($10^{22}\,\mathrm{cm}^{-3}$)	3.34	2.69	2.85	2.53	-
Hardness (Mohs)	$6\frac{1}{2}$	$6\frac{1}{2}$	$6 - 6\frac{1}{2}$	6	9
Melting temperature (K)	2680	2650	2670	2600	2310
Thermal conductivity @ 300 K ($\frac{\mathrm{W}}{\mathrm{m\,K}}$)	18.0	13.4	12.6		46.6
Thermal expansion ($10^{-6}\,\mathrm{K}^{-1}$)	9.5	8.9	8.2	8.9	5.3 ($\parallel c$) 4.8 ($\perp c$)
Maximum phonon energy (cm^{-1})	672	597	618	535	950
Transparency range (µm)	0.22 ... 8	0.23 ... 8	0.23 ... 8		0.14 ... 6.5

Table 3.2: Material properties of the sesquioxides Sc_2O_3, Y_2O_3, Lu_2O_3, and cubic Gd_2O_3, as well as those of α-Al_2O_3. The references are listed in appendix A.

3.2 Rare-Earth Doped Sesquioxides

In this thesis, the laser properties of neodymium and erbium doped sesquioxide waveguides were studied. Er^{3+} and Nd^{3+} doped sesquioxide bulk crystals were already investigated by [Pet98] and [For99], respectively. Energy level schemes of Er:Y_2O_3 and Nd:Y_2O_3 are displayed in Fig. 3.1.

Unless stated otherwise, all doping concentrations in this work are given in atomic percent, which is in respect to the cation lattice sites. The density N_d of dopant ions can thus be obtained by multiplying the doping concentration with the corresponding cation density given in Tab. 3.2.

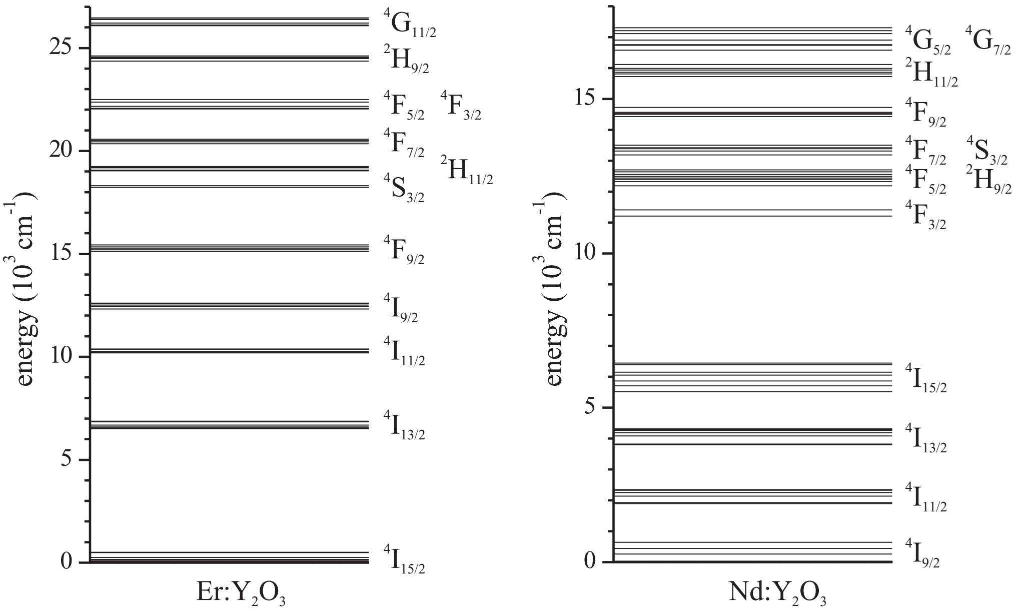

Figure 3.1: Energy level schemes of Er:Y_2O_3 [Pet98] and Nd:Y_2O_3 [For99]

3.2.1 Nd^{3+} Doping

Neodymium is a widely employed solid state laser ion. Especially Nd^{3+} doped $Y_3Al_5O_{12}$ (YAG) is frequently used as a laser material, due to the extremely high emission cross-sections of its $4f$-$4f$ transitions and the relatively high lifetime of its $^4F_{3/2}$ manifold, acting as upper laser level. Furthermore, efficient pumping into the $^4F_{5/2}$ manifold is possible using GaAlAs diode lasers. Both three and four level lasers can be realized with various emission wavelengths in the near infra-red, especially slightly below 1.1 µm ($^4F_{3/2} \rightarrow {}^4I_{11/2}$), at about 0.95 µm ($^4F_{3/2} \rightarrow {}^4I_{9/2}$), and at about 1.3 µm ($^4F_{3/2} \rightarrow {}^4I_{13/2}$). The $^4F_{3/2} \rightarrow {}^4I_{11/2}$ transitions feature extremely high emission cross-sections up to 30×10^{-20} cm^2 in YAG, but also very high ones in the sesquioxides (up to 8×10^{-20} cm^2 in Sc_2O_3) [For99]. Thus, the first rare-earth doped sesquioxide laser was realized with neodymium as active ion. While stimulated emission of Nd:Y_2O_3 at cryogenic temperatures has already been demonstrated in 1963 [Hos64], the first continuous wave (cw) Nd:Y_2O_3 laser at room temperature has been reported in 1977 [Sto78]. Also in this thesis, Nd^{3+} was chosen as most promising dopant ion for first waveguide laser experiments.

3.2.2 Er^{3+} Doping

Erbium lasers are suited for a wide range of applications. The most important erbium laser transitions are the $^4I_{11/2} \rightarrow {}^4I_{13/2}$ and $^4I_{13/2} \rightarrow {}^4I_{15/2}$ ones, emitting radiation at wavelengths of approximately 3 µm and 1.5 µm, respectively. While the former one is especially useful for medical applications, the latter one, which is investigated in this work, is used in the area of telecommunications and for applications requiring eye safety, such as remote sensing [Gra98]. Furthermore, green upconversion lasers emitting at about 550 nm ($^4S_{3/2} \rightarrow {}^4I_{15/2}$) can be realized [Moe97].

The suitability of the sesquioxides as host materials for erbium lasers has already been proven in [Pet98], demonstrating laser action on $^4\mathrm{I}_{11/2} \rightarrow {}^4\mathrm{I}_{13/2}$ transitions of Er:$\mathrm{Sc_2O_3}$ and Er:$\mathrm{Y_2O_3}$. However, laser action on a $^4\mathrm{I}_{13/2} \rightarrow {}^4\mathrm{I}_{15/2}$ transition has not been realized in [Pet98], most probably due to concentration quenching of the $^4\mathrm{I}_{13/2}$ lifetime caused by upconversion processes.

Hence, Er^{3+} concentrations below 0.4 % were chosen for first bulk-laser experiments in the framework of this thesis. As a result, continuous-wave (cw) laser emission at 1.58 µm has been demonstrated for Er:$\mathrm{Sc_2O_3}$ [Fec07a, Fec08]. A Ti:$\mathrm{Al_2O_3}$ laser[4] emitting at a wavelength of 975 nm served as pump source. For a 5.7 mm long Er(0.2 %):$\mathrm{Sc_2O_3}$ bulk crystal ($N_\mathrm{d} = 6.7 \times 10^{19}\,\mathrm{cm}^{-3}$) grown by the heat exchanger method, a slope efficiency of 6.1 % and a maximum output power of 33 mW for 700 mW of absorbed pump power have been achieved.[5] However, the efficiency of the laser was relatively low. Thus, experiments with an in-band pumping scheme were carried out. The use of Yb^{3+} as a sensitizer for crystalline Er^{3+} doped sesquioxides was extensively studied in [Kue09a, Kue09b]. However, the energy transfer between the $^2\mathrm{F}_{5/2}$ manifold of Yb^{3+} and the $^4\mathrm{I}_{11/2}$ manifold of Er^{3+} proved to be very inefficient for the investigated sesquioxides.

In-band Pumping

Instead of pumping into the $^4\mathrm{I}_{11/2}$ manifold of Er^{3+}, in-band pumping, directly into the $^4\mathrm{I}_{13/2}$ manifold, is beneficial. The $^4\mathrm{I}_{15/2} \rightarrow {}^4\mathrm{I}_{13/2}$ transitions feature significantly higher absorption cross-sections (up to $19 \times 10^{-21}\,\mathrm{cm}^2$ in $\mathrm{Sc_2O_3}$ [Pet98]) than the $^4\mathrm{I}_{15/2} \rightarrow {}^4\mathrm{I}_{11/2}$ ones (below $6 \times 10^{-21}\,\mathrm{cm}^2$ in $\mathrm{Sc_2O_3}$ [Pet98]). Furthermore, significant upconversion and excited state absorption from the $^4\mathrm{I}_{11/2}$ manifold are prevented and the quantum defect is much lower. Excited state absorption from the $^4\mathrm{I}_{13/2}$ manifold is not expected for wavelengths between approximately 1250 nm and 1600 nm.[6]

In-band pumping has been demonstrated to be very efficient for Er:YAG [She06]. Also, for the above mentioned Er(0.2 %):$\mathrm{Sc_2O_3}$ bulk crystal, in-band pumping proved to be more efficient than pumping at 975 nm. Using an erbium fiber laser[7] at 1535.6 nm as pump source, cw laser emission at 1.58 µm was observed, as in the case of pumping at 975 nm. However, a significantly higher slope efficiency of 31 % and a maximum output power of 950 mW for 3.4 W of absorbed pump power have been achieved by in-band pumping.[8] Hence, in-band pumping was also used for the gain and laser experiments performed with the Er^{3+} waveguides.

---

[4] Spectra-Physics 3900s, pumped by two Millennia Xs lasers

[5] This experiment was performed at room temperature in a nearly concentric resonator with a length $l_\mathrm{res} \approx 14.5\,\mathrm{cm}$ and radii of curvature $r_\mathrm{in} = 50\,\mathrm{mm}$ and $r_\mathrm{out} = 100\,\mathrm{mm}$ of the incoupling and outcoupling mirror, respectively. The transmission T_oc of the outcoupling mirror at the laser wavelength was 1.5 % and the laser threshold was 220 mW of absorbed pump power.

[6] These wavelengths were determined from the Stark-level energies given in [Pet98] for the $^4\mathrm{I}_{13/2}$, $^4\mathrm{I}_{11/2}$ $^4\mathrm{I}_{9/2}$ and $^4\mathrm{F}_{9/2}$ manifolds of Er^{3+} doped $\mathrm{Sc_2O_3}$, $\mathrm{Y_2O_3}$ and $\mathrm{Lu_2O_3}$.

[7] IPG ELR-10-1535-LP

[8] This experiment was also performed at room temperature. However, a hemispherical resonator with $l_\mathrm{res} \approx 10.6\,\mathrm{cm}$ and $r_\mathrm{out} = 100\,\mathrm{mm}$ was used. The output coupling T_oc was 3.2 % and the corresponding laser threshold was 200 mW of absorbed pump power.

4 Film Preparation by Pulsed Laser Deposition

The waveguides fabricated in the framework of this thesis were produced by pulsed laser deposition (PLD), a physical vapor deposition technique applicable for an abundance of different material systems, which is usually taking place far away from thermodynamic equilibrium. Due to its applicability in an oxidizing ambient and the possibility of stoichometric material transfer, it is well suited for the deposition of arbitrary oxide films. In this chapter, an introduction of the PLD process is given before the employed PLD setup as well as the substrate and target preparation are described. Afterwards, an overview of the mechanisms of film growth is given.

4.1 Pulsed Laser Deposition

The PLD technique is based on the possibility of material ablation by use of laser radiation, which has first been demonstrated in 1962 by Breech and Cross. A few years later the first PLD experiment was carried out by Smith and Turner [Smi65]. However, the intensive development of the technique started not until the late 1980s.

In PLD, a pulsed laser beam is focused onto a target of the material to be deposited. Depending on the properties of the target and the used laser radiation, both thermally and non-thermally induced ablation can take place. If the laser energy density is high enough a highly forward-directed plasma plume is created. It usually contains atoms, molecules, ions, free electrons as well as larger particulates. These species are either created during ablation of the target material or during propagation by collisions between each other or reactions with the background gas. Finally, the material is deposited on a substrate to create the desired film.

Due to the extremely high heating rate provided by the pulsed laser irradiation, the target material can be congruently evaporated before its individual components segregate into low and high vapor pressure components. Therefore, a stoichiometric material transfer from the target to the substrate is possible. This feature is especially advantageous for the deposition of complex systems, like the lattice matched mixed films fabricated in the framework of this thesis. Another advantage of PLD is the high kinetic energy of the particles (up to about 100 eV), which can have beneficial effects on the film properties, such as crystallinity and density.

A more detailed description of the PLD process can be found in various textbooks [Chr94, Eas07], as well as in the two review articles by K. L. Saenger [Sae93a, Sae93b].

4.1.1 The PLD Setup

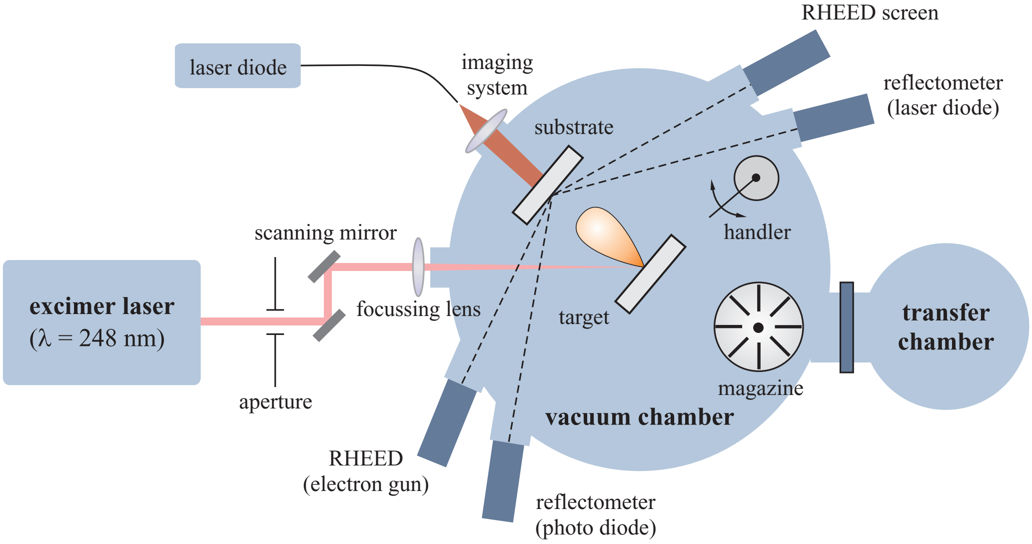

Figure 4.1: Schematic of the PLD setup

A schematic of the PLD setup[1] used for this work can be seen in Fig. 4.1. It has been shown that both ultraviolet radiation, which is strongly absorbed by a small volume of the target material, as well as nanosecond pulses are beneficial for the growth process and can lead to plumes containing mostly low-mass species [Kor89]. Thus, a KrF excimer laser[2] emitting at 248 nm with a pulse length of 20 ns was used.[3] A deflection unit and a convergent lens permitted to focus the laser beam on different positions of the target. The continuous scanning of the laser focus on the target reduced the formation of craters and cones, and allowed for the target surface to remain flat during the ablation process. This supported a plume direction perpendicular to the target surface and counteracted the ablation of large clusters, which are more likely to be produced if the plume is confined in a crater [Bec88].

Deposition took place in the main chamber, allowing for basis pressures as low as 5×10^{-8} mbar. A second vacuum chamber served as an air-lock and permitted to transfer substrates and targets to or from the main chamber while maintaining its high vacuum conditions.[4] However, fabrication of oxide films usually requires an oxidizing atmosphere. The vacuum chamber was thus filled with molecular oxygen as a background gas and the pressure was regulated by use of a flow control. Any type of background gas can influence the shape of the plume, as well as reduce the velocity of the ablated species and the amount of material reaching the substrate [Sae93b]. In the case of an oxygen atmosphere, additional chemical reactions can take place, such as those described in [Dye91] for the deposition of Y_2O_3. There are two main purposes for using an O_2 background gas: Firstly,

---

[1] The PLD setup was installed by Pink GmbH Vakuumtechnik.

[2] Lambda Physik LPX 305i

[3] Pulse repetition rates ν_r up to 50 Hz were possible.

[4] A computer controlled magazine and manipulator arm allowed for the handling of targets and substrates within the main chamber.

to compensate for an oxygen deficiency[5] leading to a non-stoichiometric film composition, and secondly, to influence the plume-dynamics and the velocities of the ablated species by regulating the pressure. In addition to the main flow control, a supplementary oxygen injector in proximity of the substrate was implemented for a better compensation of oxygen deficiencies.

To increase the mobility of the incoming species on the substrate surface, the substrate was heated to temperatures up to 1000 °C. For this, the radiation of seven fiber coupled 20 W infra-red laser diodes was imaged on an absorbing heatspreader (SiC, SiN or AlN), which had been attached to the back side of the substrate.[6]

In-situ monitoring of the film growth was possible using a differentially pumped reflection high-energy electron diffraction (RHEED) system (see section 5.1) and a reflectometer for film thickness control [Kuz06].

4.1.2 Substrate and Target Preparation

Epitaxial grade polished sapphire and sesquioxide substrates with dimensions of 10 mm × 10 mm × 0.5 mm were used for waveguide fabrication. While sapphire substrates were commercially available at CRYSTEC GMBH (Berlin, Germany), the sesquioxide substrates had to be prepared from bulk crystals, which were grown by the heat exchanger method [Vie74, Pet08, Pet09]. They were oriented, cut and polished by CRYSTEC as well.

In order to obtain a crystalline, atomically smooth substrate surface, free of contaminations, most of the substrates were annealed for $1-3$ hours at about $900-1000$ °C before deposition. The thermal treatment took place either in the vacuum chamber (in an O_2 atmosphere) or, for the later films, in a pipe furnace (in air). As shown in [Yos95] for α-Al_2O_3 and in [Gue07a, Gue07b] for Y_2O_3, the annealing leads to a surface structure consisting of atomically smooth terraces.

Sintered powder targets were used for ablation. The appropriate sesquioxide powders[7] were weighed out in the proportions of the desired film composition and pressed into small pellets by applying pressures of about 3 kbar with a hydraulic press. Afterwards, the targets were sintered at 1700 °C (in air) for 80 h, resulting in densities of about $80-90$ % of the corresponding bulk crystals. After the thermal treatment, the pellets had diameters of about 2 cm and heights ranging from 2 to 5 mm.

---

[5] The oxygen deficiency is mostly due to the low mass of the oxygen ions, which are thus strongly scattered out of the plume.

[6] The substrate temperature was measured with a one-color pyrometer.

[7] For the host materials (Sc_2O_3, Y_2O_3, Gd_2O_3 and Lu_2O_3), powders with purities of at least 99.999 % were used. The purities of the dopant materials Nd_2O_3 and Er_2O_3 were 99.99 % and 99.999 %, respectively.

4.1.3 Deposition Parameters

Suitable deposition parameters for the fabrication of sesquioxide films with the PLD setup employed in this work were already determined by [Kuz06]. Some of these parameters were further investigated and optimized for improved film quality.

The substrate temperature has a critical impact on the crystallinity of the deposited films, since it determines the mobility of the atoms on the film surface. Its influence was investigated in [Kuz06] for a set of 500 nm thick Sc_2O_3 films deposited on α-Al_2O_3 at different substrate temperatures T up to 700 °C. Since an increase of the film crystallinity with increasing temperature was shown by X-ray diffraction measurements, substrate temperatures of at least 700 °C were chosen for film growth.

As described in [Die92], the vaporization rate for pulsed laser deposition above the ablation threshold typically increases sublinearly with increasing pulse fluence. Since higher fluences often lead to a higher density of parasitic particulates, working at pulse fluences slightly above the ablation threshold of the target material is beneficial. An ablation threshold slightly below 1.5 J/cm^2 was estimated in [Kuz06] for Sc_2O_3. It has also been shown in [Kei97] that a power density of 7.5×10^7 W/cm^2 was sufficient for ablation of Y_2O_3 from a sintered powder target with an excimer laser at 248 nm. Assuming a homogeneous temporal energy distribution during the 20 ns long laser pulse, this value also corresponds to an ablation threshold of approximately 1.5 J/cm^2. Hence in this work, film fabrication was performed with laser fluences of about 1.5 to 2.5 J/cm^2. A range is given for the laser fluence, as it was changing over time with the beam quality of the excimer laser, the adjustment of the focussing optics and the transmission of the entrance-port window. In order to obtain such laser fluences on the target, the excimer laser was usually operated at a pulse energy of 800 mJ, of which merely about 10 to 20 % was transmitted into the vaccuum chamber and focussed onto a target area of approximately 0.06 cm^2.

The influence of the oxygen pressure p_{O_2} on the film properties was also investigated in [Kuz06]. Sc_2O_3 films with almost identical properties and a good crystallinity were deposited on α-Al_2O_3 for partial oxygen pressures ranging from 10^{-3} mbar to 10^{-2} mbar. Thus, most of the films were fabricated using oxygen pressures in this range.

4.2 Growth Mechanisms

4.2.1 Thermodynamic Approach

Often, thin film growth by physical vapor deposition processes takes place far away from thermal equilibrium. Especially the vapor generated by pulsed laser ablation typically possesses a very high degree of supersaturation. However, due to collisions of the plume species with each other and with the molecules of the background gas, the particles reaching the substrate may in some cases be thermalized. In any case, many of the processes occurring at the surface of the heated sample can be described by a thermodynamic model [Bau58].

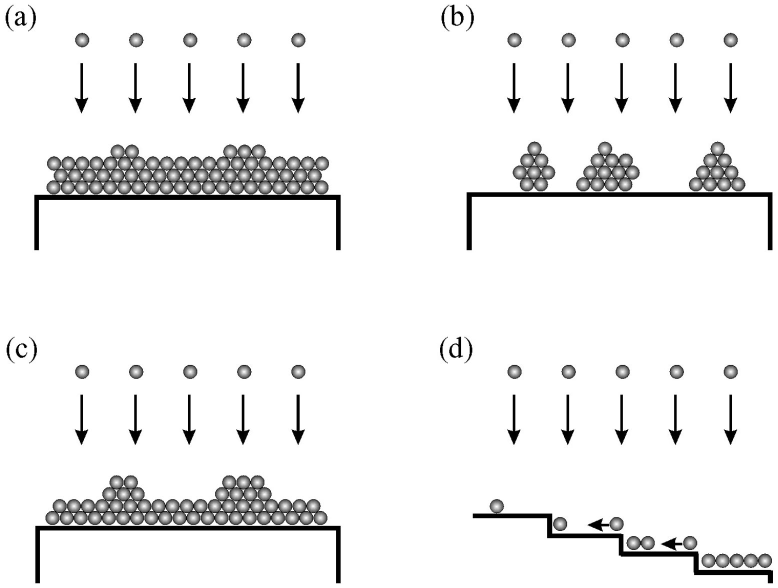

Figure 4.2: Film growth modes: (a) Frank-Van der Merwe, (b) Volmer-Weber, (c) Stranski-Krastanov and (d) step flow

Film growth can be categorized in different growth modes (see Fig. 4.2), depending on the relation between the free energies of the film surface (γ_f), the substrate surface (γ_s), and the interface between film and substrate (γ_i). The relation between these energies during nucleation is given by Young's equation [Kai02]:

$$\gamma_\mathrm{s} = \gamma_\mathrm{i} + \gamma_\mathrm{f} \cos \varphi \tag{4.1}$$

Here, φ is the wetting angle of a liquid nucleus on the substrate. If the interaction between substrate and film atoms is greater than the one between adjacent film atoms ($\gamma_\mathrm{s} > \gamma_\mathrm{f}+\gamma_\mathrm{i}$), layer-by-layer growth takes place, which is also known as Frank-van der Merwe growth or two-dimensional (2D) growth (Fig. 4.2a). In this case, the growth of one monolayer is finished before nucleation of the next monolayer takes place. The opposite case is called island growth, Volmer-Weber growth or three-dimensional (3D) growth (Fig. 4.2b). Since the interaction between film atoms is greater than between adjacent film and substrate atoms ($\gamma_\mathrm{s} < \gamma_\mathrm{f} + \gamma_\mathrm{i}$), separate three-dimensional islands are formed. A hybrid form of the two cases described above is the Stranski-Krastanov growth mode (Fig. 4.2c), which is characterized by a change of growth mode from layer-by-layer to island growth. Stranski-Krastanov growth is usually caused by a lattice mismatch between substrate and film, which results in two dimensional strain and an increase of the elastic energy with the layer thickness. If the film exceeds a critical thickness, misfit dislocations will be introduced to relieve the mismatch strain and the growth mode changes.

4.2.2 Lattice Matching

One aim of this work has been the fabrication of monocrystalline films by epitaxial growth. Epitaxy denotes an ordered film growth on a crystalline substrate. It is characterized by a crystallographic correlation, forcing the film to grow with the orientation given by the substrate. If substrate and film materials are identical the process is called homoepitaxy, otherwise heteroepitaxy. Since a refractive index difference between film and substrate is required for waveguiding, this work focuses on heteroepitaxial growth.

In order to realize epitaxial growth, a high degree of lattice matching between film and substrate is required. Ideal lattice matching is given if film and substrate possess the same crystal structure and lattice constant. Lattice matching in a less strict definition is also possible for materials with different crystal structures but similar lattice planes. In this case, the lattice spacings $a_{0,\mathrm{f}}$ and $a_{0,\mathrm{s}}$ of the film and substrate plane, respectively, have to be integer multiples:

$$n\, a_{0,\mathrm{f}} = m\, a_{0,\mathrm{s}} \qquad n, m \in \mathbb{N}^*,\ n = 1 \vee m = 1 \tag{4.2}$$

Epitaxial growth is not only possible with perfect lattice matching, but also, to a certain degree, with a lattice mismatch f, as defined by the following equation:

$$f = \frac{n\, a_{0,\mathrm{f}} - m\, a_{0,\mathrm{s}}}{n\, a_{0,\mathrm{f}}} \tag{4.3}$$

As long as the lattice mismatch does not exceed a critical value, which is dependent on the film thickness and the material properties, the lattice spacings of the film can fit those of the substrate by inducing elastic deformations [Fra49]. Such a growth process is termed pseudomorph.

4.2.3 Growth Kinetics

During PLD, the growing film is usually not in thermodynamic equilibrium. The vapor possesses a high supersaturation, leading to a large nucleation rate. If the surface diffusion is not sufficient, the deposited material cannot rearrange itself to minimize the surface energy. Thus, the thermodynamic model described in section 4.2.1 cannot be applied and kinetic effects have to be considered. Although homoepitaxial growth is assumed in the following considerations, most of them can be applied to heteroepitaxial systems with perfect lattice matching as well.

Both the intralayer and interlayer mass transport have to be considered to understand the possible 2D growth modes on a surface with atomically flat terraces. Intralayer and interlayer mass transport denote the diffusion of atoms on a terrace and the diffusion to lower terraces, respectively. An important kinetic parameter describing the intralayer mass transport is the diffusion length l_D. It determines the average distance an atom can travel on a flat surface before being trapped.

If l_D is larger than the average terrace width, the adatoms possess a sufficiently high mobility to reach the terrace edges and expand them. This behavior, leading to propagating steps, is illustrated in Fig. 4.2d and is called step flow growth. In case of a slower intralayer mass transport, nucleation on the terraces will take place. At first, new nuclei will be formed, but then, with increasing density, it becomes more and more likely for atoms to attach to existing nuclei, thus forming islands.

In this case, the growth mode strongly depends on the interlayer mass transport, as a steady interlayer mass transport will allow the atoms which are deposited on top of an existing island to diffuse to the lower layer. In the ideal case, termed layer-by-layer growth, each layer is completed before nucleation on the next one takes place. The other extreme is multilayer growth due to second-layer nucleation; as the interlayer mass transport is very limited, nucleation will take place on top of islands before they have merged to form a complete layer. In reality, a growth mode in between those two extreme cases will occur.

5 Analytical Techniques

In this chapter, the analytical techniques used for the structural and spectroscopical characterization of the thin films are introduced. The growth was monitored *in-situ* by use of reflection high-energy electron diffraction (RHEED), the surface morphology was investigated by atomic force microscopy (AFM), and the crystalline structure was examined using X-ray diffraction (XRD). Furthermore, absorption and emission cross-sections as well as fluorescence lifetimes were measured by optical spectroscopy.

5.1 Reflection High-Energy Electron Diffraction

Film growth during pulsed laser deposition was monitored by use of reflection high-energy electron diffraction (RHEED). An electron beam[1] strikes the sample surface at a grazing angle Θ_i, as illustrated in Fig. 5.1. The electrons are scattered from the sample surface and generate a characteristic diffraction pattern on a phosphorescent screen. Due to the grazing angle of incidence, RHEED is an extremely surface sensitive diffraction technique. It allows to monitor the coverage of the sample surface by adsorbates and to reveal changes in the surface structure of the film. In this section, a brief introduction to the basic principles of RHEED is given. A more detailed description can be found in [Bra99].

5.1.1 Diffraction Patterns

The basic principle of RHEED can be described by the kinematic scattering theory, which considers single elastic scattering only. According to the Laue condition (5.1), diffraction only occurs if the difference between the wavevectors $\mathbf{k_0}$ and $\mathbf{k_s}$ of the incident and diffracted wave, respectively, is equal to a reciprocal lattice vector $\mathbf{G}$.

$$\mathbf{k_s} - \mathbf{k_0} = \mathbf{G} \tag{5.1}$$

Since elastic scattering is assumed ($|\mathbf{k_s}| = |\mathbf{k_0}|$), Eq. (5.1) can be illustrated by the Ewald sphere construction. For a 3D lattice, $\mathbf{k_0}$ is drawn in such a way that it ends at a reciprocal lattice point and the Ewald sphere is defined as the sphere with radius $|\mathbf{k_0}|$ around the origin of $\mathbf{k_0}$. The Laue condition is satisfied for all $\mathbf{k_s}$ connecting the origin of the sphere to an arbitrary reciprocal lattice point on the sphere.

---

[1] The beam was generated by an electron gun (EK-2035-R, Staib Instrumente GmbH) within a two-stage differentially pumped vacuum system.

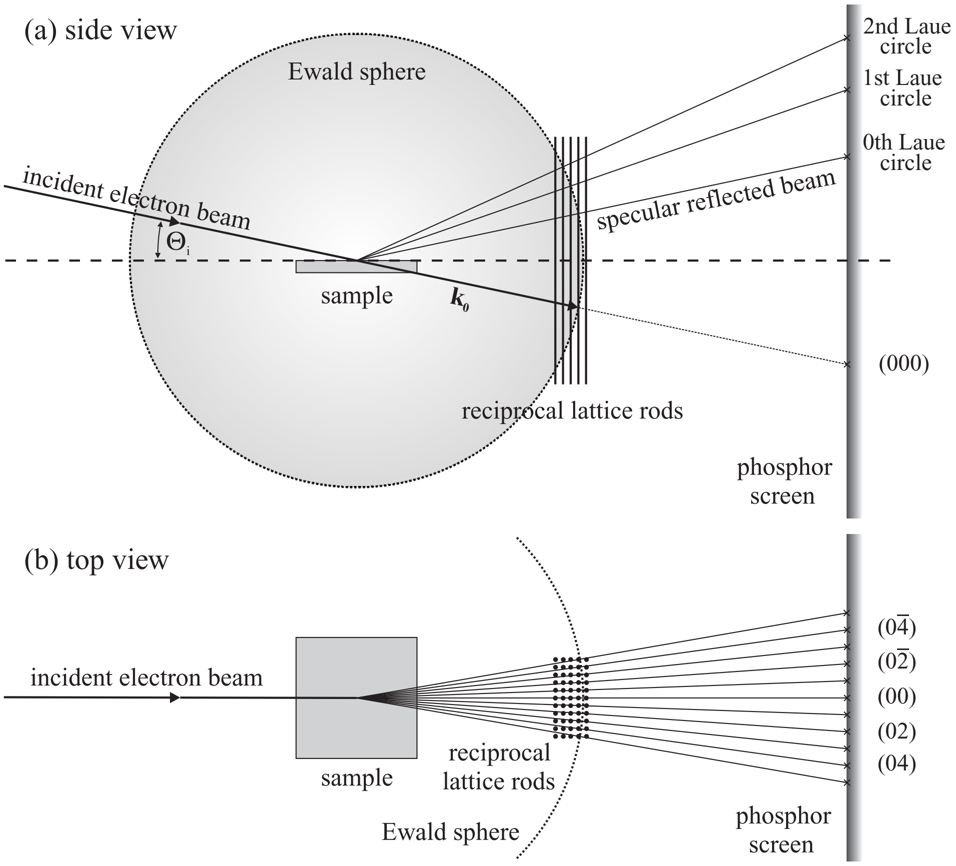

Figure 5.1: Schematic of the RHEED geometry. An electron beam strikes the sample surface at the grazing angle Θ_i and is diffracted. The intensity maximum (hk) on the screen corresponds to the projected intersection of the Ewald sphere with the reciprocal lattice rod (hk).

A schematic of the RHEED geometry is shown in Fig. 5.1. Considering a perfect 2D surface, the reciprocal lattice consists of infinitely thin rods, which are perpendicular to the surface and labeled with the integer indices (hk). The origin of the Ewald sphere is located at a reciprocal lattice rod and reflection high-energy electron diffraction maxima are produced along the direction for which the rods pierce the sphere. The resulting diffraction spots are lying on concentric circles, termed Laue circles. Each spot is classified by the same indices (hk) as the corresponding reciprocal lattice rod intersecting the Ewald sphere. In this notation, the diffraction spot caused by the specular reflected beam is termed (00). The origin of the reciprocal lattice is projected onto a point labeled (000). This point becomes visible if a fraction of the incident beam misses the sample.

The electron beam used in the framework of this thesis consisted of electrons with energies E of 25 keV. According to Eq. (5.2) [Bra99], this corresponds to a $|\mathbf{k_0}|$ of approximately $80\,\text{Å}^{-1}$.

$$|\mathbf{k_0}| = \frac{1}{\hbar}\sqrt{2m_eE + \frac{E^2}{c_0^2}} \tag{5.2}$$

Since $|\mathbf{k_0}|$ is more than two orders of magnitude larger than the reciprocal lattice constants $a^* \approx 0.6\,\text{Å}^{-1}$ of the investigated sesquioxides, the Ewald sphere is very large compared to the reciprocal lattice spacings. Therefore, even at very small diffraction angles, only a few higher order maxima are visible in the RHEED pattern.

Several surface parameters can be derived from the diffraction pattern, such as the in-plane lattice constants, the average crystal potential and the misorientation angle of a tilted surface [Bra99, Eas07]. Furthermore, the diffraction pattern gives information about the texture of the surface, as described in [Hen94] and illustrated in Fig. 5.2.

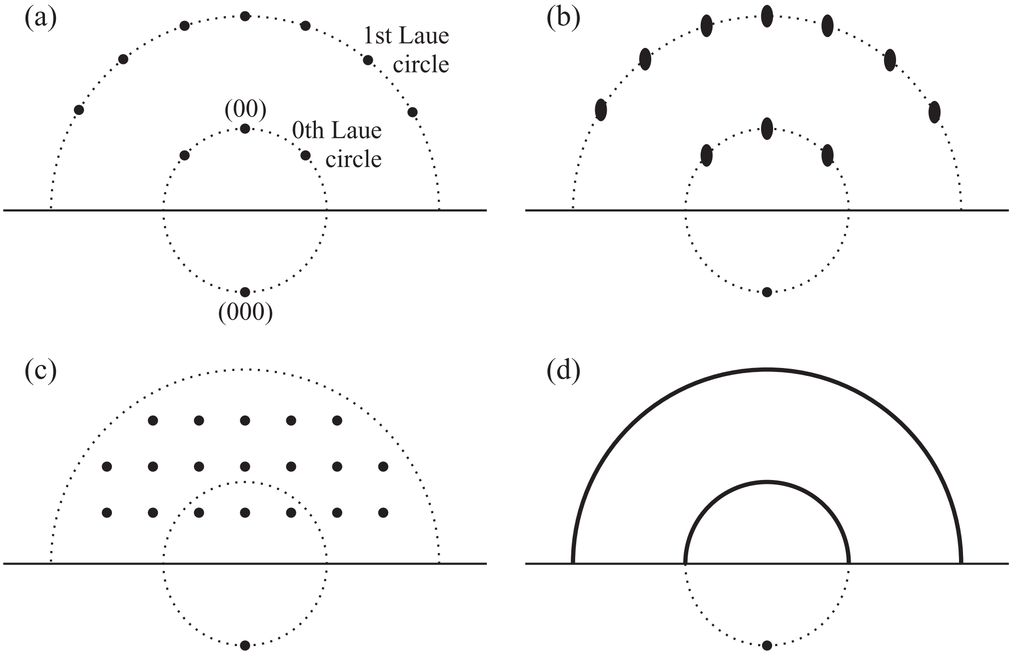

Figure 5.2: Schematic representation of the RHEED patterns resulting from diffraction at different surface types: (a) perfect 2D surface, (b) surface with slight crystal domain tilt or slightly stepped surface, (c) surface with 3D islands and (d) surface of a polycrystalline film

As pointed out above, the reciprocal lattice of a perfect 2D surface consists of infinitely thin rods. The intersections of the Ewald sphere with these rods result in a RHEED pattern consisting of sharp diffraction spots (Fig. 5.2a). For a surface covered with 2D islands, as well as surfaces with a slight step-terrace structure or crystal domain tilt, however, the reciprocal lattice rods are of finite thickness. In this case, instead of sharp spots, the diffraction pattern consists of blurred streaks (Fig. 5.2b). A surface covered by 3D islands possesses a reciprocal lattice comparable to that of a 3D crystal structure and results in diffraction spots similar to those shown in Fig. 5.2c. While the surface of a polycrystalline film consisting of randomly oriented grains results in a series of rings in the RHEED pattern (Fig. 5.2d), a preferential texture in the film leads to broken rings [And96].

5.1.2 RHEED Oscillations

While the shape of the diffraction pattern gives information about the structure and quality of the sample surface, additional information about the growth process can be obtained by monitoring the intensity variations of the diffraction spots. In case of a layer-by-layer growth mode, as described in section 4.2, the periodic variations of the surface morphology due to nucleation and coalescence of 2D islands can lead to intensity oscillations of the diffraction spots. These RHEED oscillations can be described by various theoretical models [Bra99]. It has been shown for several material systems, including the sesquioxides Y_2O_3 and Sc_2O_3, that the period of one oscillation usually corresponds to the growth of one monolayer [Lee91, Bra99, Gue07a, Gue07b]. Thus, RHEED oscillations confirm a layer-by-layer growth mode and can also be used to determine the growth rate.

5.2 Atomic Force Microscopy

The surface morphology of the films was characterized by atomic force microscopy (AFM) [Bin86].[2] In contrast to scanning tunnelling microscopy (STM) and scanning electron microscopy (SEM), the AFM technique is applicable for insulating surfaces and therefore useful for the investigation of oxide films. In this section an overview of the AFM technique is given. A more detailed description can be found in [Erl00].

The basic principle of AFM is illustrated in Fig. 5.3. A small tip mounted on a flexible cantilever serves as a force sensor. In the ideal case, only the tip apex atom interacts with the sample surface. The resulting bend of the cantilever (contact mode) or the change of its effective resonance frequency (non-contact mode) is measured by a deflection sensor, consisting of a laser diode and a 4-quadrant photo diode. To obtain a topographic image, the probe is raster scanned accross the sample surface (x and y direction) using piezoelectric transducers. By varying the distance z between tip and sample and by use of a feedback controller, the measured force is kept at a constant level. It is then assumed that the necessary motion in z direction corresponds to height variations of the sample surface.

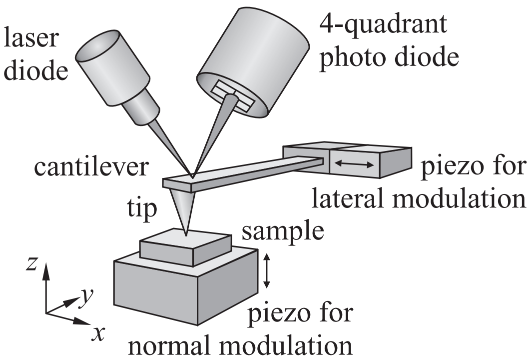

Figure 5.3: AFM setup [Bae04]

The forces between the tip and the surface can be separated into short-range and long-range forces. Usually, the former consist of the repulsive Coulomb force between the ion cores as well as exchange interactions between the electrons. As long-range force, there is usually the Van der Waals interaction. Depending on the experimental conditions, other long-range interactions, such as electrostatic, magnetic and capillary forces, are possible as well.

---

[2] A Veeco Digital Instruments CP-II was used.

In the framework of this thesis two different AFM operation modes were used. They are outlined in the following sections.

5.2.1 Contact Mode

In the contact mode, the tip-to-sample spacing is less than a few angstroms and the repulsive short-range forces cause the cantilever to bend. Assuming that a constant bend corresponds to a constant force, the topography of the sample can be mapped as described above. To obtain a high force sensitivity and to avoid damage to fragile samples, a cantilever with a low spring constant is used[3]. Due to the short range of the repulsive force between the tip apex atom and the sample, a very high resolution should be possible in this operating mode. In reality however, the tip is also subject to the long-range attractive van der Waals force that acts over a large part of the tip [Erl00], and atomic resolution is thus not easily obtained using contact AFM. Hence, the non-contact mode, which is described in the following section, was used whenever atomic resolution was required.

5.2.2 Non-Contact Mode

During non-contact AFM, the cantilever is oscillated at a frequency slightly above its undisturbed resonance frequency[4]. The tip-to-sample distance is usually ranging from tens to hundreds of angstroms were the probe is sensitive to the usually attractive long-range forces, such as the Van der Waals interactions. In such a regime with an attractive force gradient, the effective spring constant of the cantilever and its effective resonance frequency will be lowered when approaching the sample. The resulting decrease of the oscillation amplitude allows to control the tip-sample separation.

5.3 X-Ray Diffraction

The fabricated films were also characterized using X-ray diffraction (XRD), which allowed to examine their orientation, degree of crystallinity, texture and lattice constant. The measurement is based on analyzing the angular intensity distribution of monochromatic X-rays, which are scattered at inner shell electrons of the sample atoms. If the scattering atoms are statistically arranged the X-rays are incoherently scattered and the resulting intensities are proportional to the number of scattering centers N. In case of a regular, periodic arrangement of the scattering atoms, however, interference between scattered X-rays takes place. Constructive interference, resulting in scattering intensities proportional to N^2, occurs at incident angles θ that satisfy Bragg's diffraction law [Cul01]:

$$2\,d\sin\theta = m\lambda \tag{5.3}$$

---

[3] For the contact mode, silicon cantilevers with spring constants $k = 0.9\,\mathrm{N/m}$ and undisturbed resonance frequencies $f_0 = 17 - 21\,\mathrm{kHz}$, as well as silicon nitride cantilevers with $k = 0.05\,\mathrm{N/m}$ and $f_0 = 15 - 30\,\mathrm{kHz}$ were used.

[4] Silicon cantilevers with spring constants $k = 20 - 80\,\mathrm{N/m}$ and undisturbed resonance frequencies $f_0 = 251 - 319\,\mathrm{kHz}$ were used for the non-contact measurements.

Therein, λ is the wavelength of the X-rays, d the distance between periodically arranged atomic planes (see Fig. 5.4a) and m an integer describing the order of diffraction.

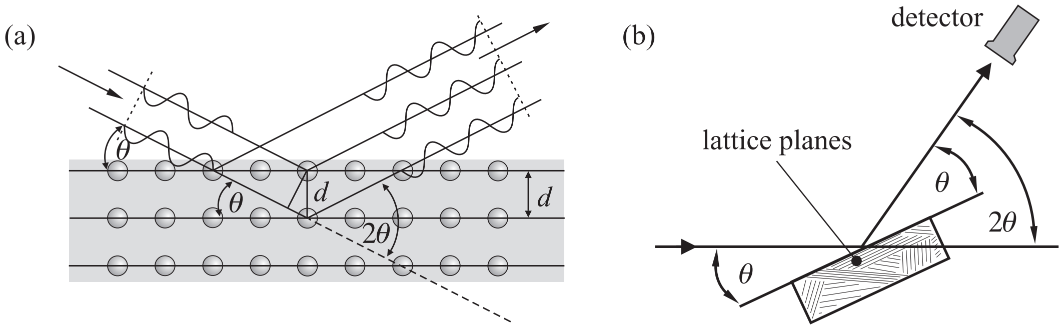

Figure 5.4: (a) illustration of X-ray diffraction at a crystal lattice [Bae04], (b) angle definitions for θ-2θ scans [Rab04]

In the framework of this thesis, both θ-2θ scans and rocking-curve measurements (ω scans) were performed. For the former, θ and 2θ were scanned simultaneously by rotating the sample and the detector in such a manner that the angle θ between the incident beam and the sample surface is equal to the angle between surface and detector (see Fig. 5.4b). Using Eq. (5.3), the spacings d between lattice planes parallel to the sample surface can be derived from the angles 2θ at which diffraction peaks occur. For cubic crystals with a lattice constant a, the distance d_{hkl} between the planes (hkl) with the Miller indices h, k and l is given by [Cul01]:

$$d_{\mathrm{hkl}} = \frac{a}{\sqrt{h^2 + k^2 + l^2}} \tag{5.4}$$

Thus, with a θ-2θ scan it is possible to identify the existing crystallographic orientations[5] and to determine the lattice constants from the positions of diffraction peaks corresponding to known orientations.

Both monocrystalline and polycrystalline films were investigated. The latter consisted of many slightly tilted monocrystalline regions, which are called crystallites in the following. Assuming that the grown films show no stress, the size L of these crystallites[6] can be roughly estimated from the peak width with the Scherrer equation [Cul01]:

$$L = \frac{K\,\lambda}{\omega_{\mathrm{peak}}\,\cos(\theta)} \tag{5.5}$$

ω_{peak} is the full-width at half maximum (FWHM) with respect to 2θ and K is a constant with a value between 0.9 and 1, which depends on the shape of the crystallites and is assumed to be 1 within this work.

---

[5] There is not necessarily a diffraction peak for every occurring crystallographic orientation. Structure-factor calculations [Cul01] show that there are no reflections for planes with odd $(h+k+l)$ in crystals possessing a body-centered lattice, such as the investigated sesquioxides.

[6] L is the crystallite dimension perpendicular to the sample surface. A sufficient broadening can only be observed for $L \gg \lambda$.

In order to investigate the distribution of crystallographic orientations, rocking-curve measurements were performed. The angle 2θ was kept constant to match the position of a diffraction peak, and the angle of incidence ω was scanned in order to obtain diffraction from lattice planes which are not parallel to the surface.

The XRD measurements were performed at the FACHHOCHSCHULE WEDEL, using the same diffractometer[7] as described in [Kuz06]. It was equipped with a copper X-ray source operating at 40 kV and 20 mA. The emission spectrum contained Cu-$K_{\alpha 1}$ ($\lambda = 1.5406\,\text{Å}$), Cu-$K_{\alpha 2}$ ($\lambda = 1.5444\,\text{Å}$) and some residue of Cu-K_β ($\lambda = 1.3922\,\text{Å}$) radiation.[8] Slit sets providing nominal resolutions of 0.15° were used for the θ-2θ overview scans and those providing resolutions of 0.018° for the high-resolution θ-2θ scans and the rocking-curve measurements. An instrumental resolution ω_{inst} of 0.04° has been determined in [Kuz06] for the high-resolution scans. For the estimation of the crystallite size with Eq. (5.5), the instrumental resolution was taken into account by assuming Gaussian peak profiles and correcting the measured peak width ω_{meas} as in [Kuz06]:

$$\omega_{\text{peak}} = \sqrt{\omega_{\text{meas}}^2 - \omega_{\text{inst}}^2} \tag{5.6}$$

5.4 Spectroscopic Measurements

5.4.1 Emission and Excitation Spectroscopy

Both emission and excitation spectra of PLD films and bulk crystals were measured under continuous wave (cw) excitation, as illustrated in Fig. 5.5.

For this, the beam of a tunable Ti:Al_2O_3 laser[9] was focused onto the sample with a grazing angle of incidence. The resulting fluorescence light was imaged onto the entrance slit of a monochromator[10] and detected with an InGaAs photo diode. Either the incident excitation light or the fluorescence light was periodically interrupted with a chopper and the lock-in technique was applied. In order to determine the spectral response function of the set-up and to calibrate the emission spectra, the fluorescence of a tungsten lamp with a filament temperature of 2200 K was measured under comparable experimental conditions and the resulting spectrum was divided by the spectral radiant intensity of tungsten, which had been calculated with

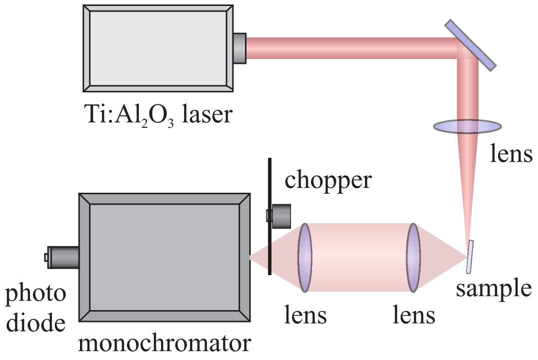

Figure 5.5: Fluorescence spectroscopy setup

---

[7] SIEMENS Kristalloflex 810

[8] The Cu-K_β radiation was suppressed by a Ni-foil serving as filter.

[9] SPECTRA-PHYSICS 3900s, pumped by a Millennia X laser

[10] A 1 m spectrometer (SPEX 1000M) and gratings with 600 lines/mm, optimized for wavelengths of either 1 µm or 1.5 µm, were used.

Planck's law and the emissivity measured in [Dev54]. For excitation spectroscopy, the wavelength of the $\mathrm{Ti{:}Al_2O_3}$ laser was tuned by use of a step-motor and the spectra were corrected by considering the wavelength dependence of the laser output power.

Füchtbauer Ladenburg Equation

The emission cross-sections $\sigma_{UL}(\lambda)$ for stimulated emission of the transition $U \to L$ can be determined from the fluorescence spectra by using the Füchtbauer Ladenburg equation [Web74] as described in [Sch01]:

$$\sigma_{UL}(\lambda) = \frac{\lambda^5}{8\pi\, n^2\, c_0\, \tau_U} \frac{P_{UL}(\lambda)}{\sum_{L^*} \int_{U \to L^*} \lambda^*\, P_{UL^*}(\lambda^*)\, d\lambda^*} \tag{5.7}$$

The refractive index n is assumed to be constant over the entire wavelength range. $P_{UL}(\lambda)$ denote the relative powers of spontaneous emission for the transition $U \to L$ in dependance of the wavelength λ. The integral covers the entire wavelength range of the transition $U \to L^*$ between the upper energy level U with the radiative lifetime τ_U and the lower energy level L^*. Instead of summing up the integrals of all possible radiative transitions from U into a lower level L^*, the branching ratio

$$\eta(U,\, L) := \frac{A(U,\, L)}{\sum_{L^*} A(U,\, L^*)} \tag{5.8}$$

of the transition $U \to L$ with the spontaneous emission rate $A(U,\, L)$ can be incorporated into Eq. (5.7) by use of the following equation [Sch01]:

$$\eta(U,\, L) = \frac{\int_{U \to L} \lambda^*\, P_{UL}(\lambda^*)\, d\lambda^*}{\sum_{L^*} \int_{U \to L^*} \lambda^*\, P_{UL^*}(\lambda^*)\, d\lambda^*} \tag{5.9}$$

The resulting Eq. (5.10) allows to determine the emission cross-sections of a transition in a multi-level system from the fluorescence spectrum of this transition only, provided that the branching ratio is known.

$$\sigma_{UL}(\lambda) = \frac{\lambda^5}{8\pi\, n^2\, c_0\, \tau_U} \frac{\eta(U,\, L)\, P_{UL}(\lambda)}{\int_{U \to L} \lambda^*\, P_{UL}(\lambda^*)\, d\lambda^*} \tag{5.10}$$

In this work, the energy levels U and L denote entire manifolds consisting of thermally coupled energy levels and the determined $\sigma_{UL}(\lambda)$ are effective emission cross sections $\sigma_{\mathrm{em}}(\lambda)$ at room temperature.

5.4.2 Absorption Spectroscopy

In order to determine the cross sections for ground state absorption (GSA), room temperature transmission measurements of bulk crystals were performed with a two-channel spectrophotometer[11]. Attenuation within the crystals was assumed to be due to resonant absorption only. Furthermore, the intensity was assumed to be significantly small enough for the density of excited ions to be negligible in comparison to the density of ions in the ground state[12], which was thus approximated to be equal to the total density N_t of active ions.

The effective absorption cross-sections $\sigma_\mathrm{abs}(\lambda)$ at room temperature were derived from the small-signal absorption coefficients $\alpha_\mathrm{abs}(\lambda)$, as introduced in Eq. (2.51). These absorption coefficients were obtained using Beer-Lambert's law (2.52).

Since the intensities $I(\lambda,\, z)$ within the sample of length l could not be measured directly, the ratio $I(\lambda,\, l)/I(\lambda,\, 0)$ was derived from the measured transmission $T(\lambda)$:

$$\frac{I(\lambda,\, l)}{I(\lambda,\, 0)} = \frac{T(\lambda)}{T_\mathrm{max}} \tag{5.11}$$

T_max is the maximum transmission measured at a wavelength where no absorption takes place. This approach assumes that absorption is the only significant loss mechanism within the sample, which is usually justified for bulk crystals of high optical quality.

5.4.3 Lifetime Measurements

Fluorescence lifetimes of Nd^{3+} and Er^{3+} doped sesquioxide films were determined by time resolved emission measurements, as illustrated in Fig. 5.6.

An optical parametric oscillator (OPO), which was pumped by the third harmonic of a Q-switched Nd:YAG laser,[13] served as excitation source. The excitation light (pulse length ≈ 20 ns, pulse energy ≈ 10 mJ, repetition rate 10 Hz) was slightly focussed onto the sample and the resulting fluorescence light was imaged onto the entrance slit of a monochromator[14]. An InP/InGaAs photo multiplier[15], which was cooled to -60 °C, served as detector. The signal of a few thousand pulses was recorded and averaged with a storage oscilloscope, and the lifetime was determined from the fluorescence decay curves.

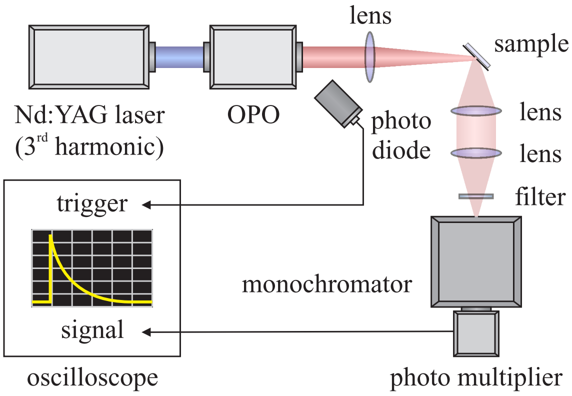

Figure 5.6: Lifetime measurement setup

---

[11] Varian Cary 5000

[12] The ground state is the $^4\mathrm{I}_{13/2}$ or $^4\mathrm{I}_{9/2}$ manifold of Er^{3+} or Nd^{3+}, respectively.

[13] Solar Laser Systems: LQ129, LG103 and either a LP601 or LP603

[14] Spex 0.5 m spectrometer

[15] Hamamatsu Photonics H9170-75

In order to estimate the effect of radiation trapping on the measured lifetimes, series of measurements with varying excitation volumes were performed for some of the samples. This was realized by mounting small pinholes with diameters from 0.5 to 2.5 mm onto the sample surface (pinhole method [Kue07]).

6 Characterization of Sesquioxide Films

Several combinations of film and substrate materials were investigated regarding their suitability for the fabrication of high quality waveguiding films by PLD. Due to their beneficial properties outlined in chapter 3.1.1, film materials were chosen among the sesquioxides. Hence, suitable substrate materials with lower refractive indexes but similar lattice structures and lattice spacings had to be found. Three different types of such film-substrate combinations were investigated within this thesis. The results of the structural and spectroscopic characterization are described in the following sections.

6.1 Structural Characterization

6.1.1 Sesquioxide Films on Sapphire

The use of sapphire as substrate material for the growth of sesquioxide films is promising, due to its commercial availability and the relatively high refractive index differences between film and substrate (see Tab. 6.1).

Materials	f	$\triangle n_{1.55\,\mu\mathrm{m}}$
Sc_2O_3 on α-Al_2O_3	-2.46 %	0.21
Y_2O_3 on α-Al_2O_3	4.75 %	0.14
Lu_2O_3 on α-Al_2O_3	2.80 %	0.16

Table 6.1: Lattice mismatch f for sesquioxide growth in <111> direction on (0001) oriented α-Al_2O_3 as well as refractive index differences $\triangle n_{1.55\,\mu\mathrm{m}}$ at the wavelength $\lambda = 1.55\,\mu\mathrm{m}$

The $\{111\}$ planes of the cubic sesquioxide lattice (with lattice constant a_{cub}) possess a hexagonal symmetry and lattice spacings which are about three times larger than the lattice constants a_{hex} in the hexagonal (0001) plane of α-Al_2O_3. Therefore, lattice matching in a less strict definition ($\sqrt{2}\,a_{\mathrm{cub}} \approx 3\,a_{\mathrm{hex}}$) is possible. This is illustrated in Fig. 6.1. The resulting lattice mismatches f calculated with Eq. (4.3) are given in Tab. 6.1. Pulsed laser deposition of sesquioxide films on sapphire substrates was already investigated by [Bur02, Bae04, Kuz06] and is further examined in this thesis.

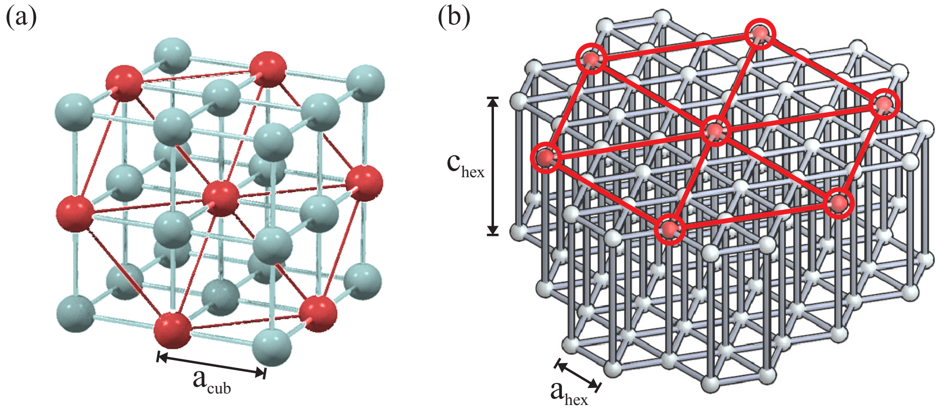

Figure 6.1: Illustration of (a) the cubic sesquioxide lattice [Bae04], (b) the hexagonal α-Al_2O_3 lattice, and the symmetry matching of the {111} planes and (0001) planes

Growth Behavior

The growth behavior during the first 80 nm of film growth was investigated for an Er(0.6 %):Y_2O_3 film[1], deposited on a (0001) oriented α-Al_2O_3 substrate.[2] Figure 6.2a shows the RHEED pattern and surface morphology of the annealed substrate prior to deposition. The diffraction pattern indicates a nearly atomically flat surface, which is confirmed by the AFM image, showing atomic steps and atomically flat terraces.

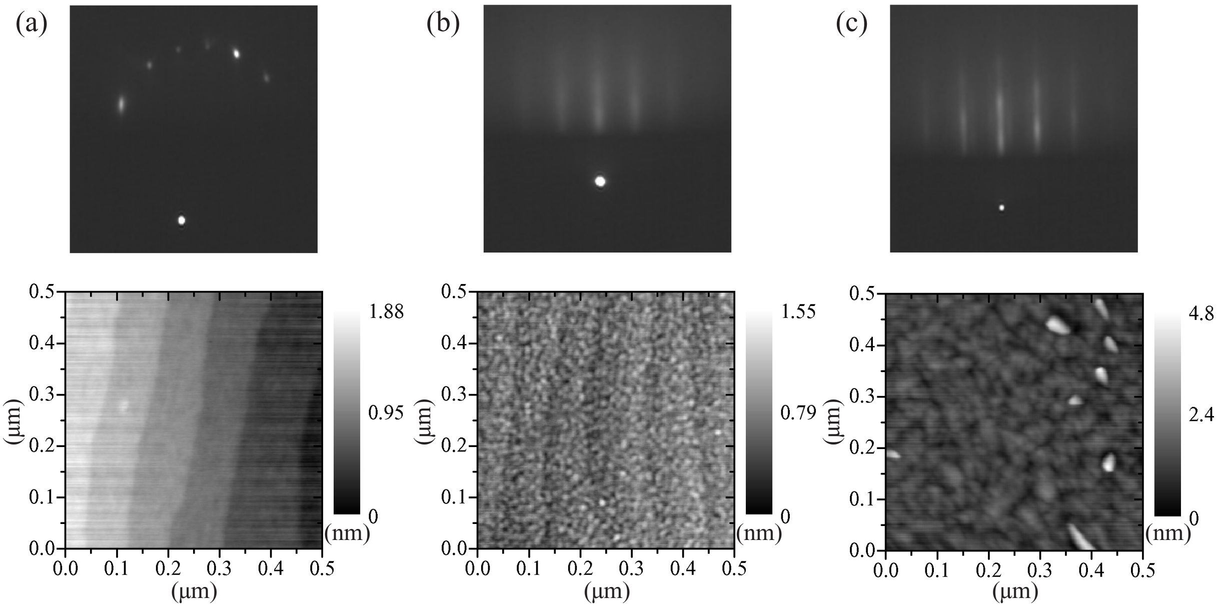

Figure 6.2: RHEED patterns (upper row) and AFM images (lower row) of (a) an annealed α-Al_2O_3 (0001) substrate, (b) after deposition of a 9 nm thick Er(0.6 %):Y_2O_3 film and (c) at a film thickness of 80 nm

---

[1] K67: $T = 900\,°C$, $p_{O_2} = 2.1 \times 10^{-3}$ mbar and $\nu_r = 1$ Hz

[2] In the following, the deposition parameters are specified in the form of the footnote above. The sample name is followed by the parameters not given in the main text.

The growth process was monitored *in-situ* by RHEED (see section 5.1). No change in symmetry and spacing of the diffraction pattern was observed during growth of the first three monolayers[3]. However, the intensity of the diffracted beams decreased and the RHEED pattern finally vanished, as shown in Fig. 6.3. This indicates an amorphous film growth, which might be due to subplantation. The partial intensity relaxation after each pulse and the slight intensity rise after deposition of about one monolayer indicate, however, the presence of pseudomorphically grown regions.

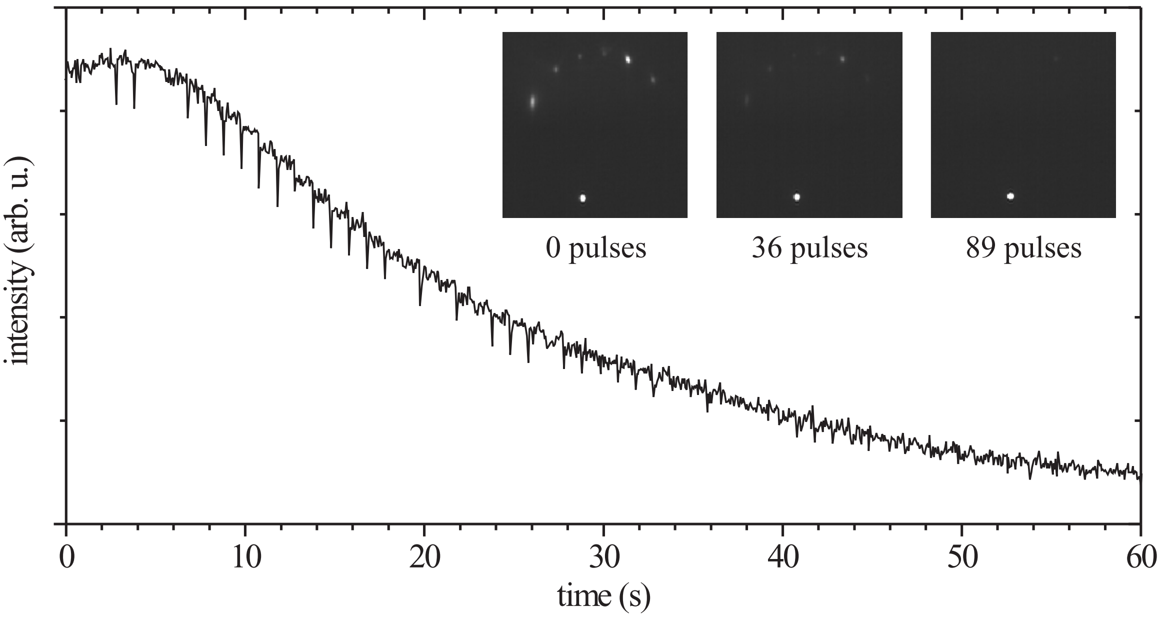

Figure 6.3: RHEED patterns and intensity behavior of the (01) reflex during the growth of Er(0.6 %):Y_2O_3 on (0001) oriented α-Al_2O_3 with a repetition rate of 1 Hz

As the growth continued, crystallization took place and a streaky diffraction pattern indicating a multi-level 2D growth mode appeared (see Fig. 6.2b). The corresponding AFM image shows height variations of only a few monolayers and some remaining indications of the underlying step structure. During the following deposition, a transition to a 3D growth mode took place. This is indicated by the spots appearing in the RHEED pattern (see Fig. 6.2c). The appearance of an amorphous interface and a change in growth behavior was also observed for deposition of Sc_2O_3 on α-Al_2O_3 (see [Gue07a]).

---

[3] A growth rate of 0.011 nm/pulse was calculated from the RHEED oscillations during quasi-homoepitaxial growth of Er:(0.6 %):Y_2O_3 on both {100} and {111} oriented Y_2O_3 substrates (films K68 and K69). The same target and deposition parameters as for the film grown on α-Al_2O_3 were used. The height of an Y_2O_3 monolayer in <111> direction is $a_{\mathrm{cub}}/2\sqrt{3}$ [Gue07a], which corresponds to 28 pulses.

Film Properties

In order to examine the influence of the deposition parameters on the structural film properties, various 1 µm thick Er:Y_2O_3 films were fabricated and investigated. Most of the films for these series of measurements were successively deposited using the same target. New targets were pre-ablated with a few thousand laser pulses to ensure a smooth target surface free of contaminations. However, this treatment was not always sufficient, as using new targets often resulted in films of low crystallinity and without any preferential growth direction. Subsequent targets were thus pre-ablated with at least 10000 pulses, which resulted in a more reproducible film growth.

While the influence of the ambient pressure on the film properties was already examined for Sc_2O_3 films [Kuz06], further investigations for Y_2O_3 were performed in the framework of this thesis. Several 1 µm thick Er(1 %):Y_2O_3 films were fabricated at different ambient pressures, but with otherwise similar deposition parameters[4]. The crystallinity of these films was characterized by XRD measurements. An overview of the θ-2θ scans is displayed in Fig. 6.4. Beside the pronounced intensity maxima[5] corresponding to the (0001) planes of the substrate and {111} planes of the film, only very few other peaks, which are of low intensities, are observable in the XRD spectra. This confirms a highly-textured film growth in <111> direction. However, such a highly-textured growth was also observed in [Ehl05] for Y_2O_3 films deposited on amorphous quartz-glass substrates and is therefore not necessarily due to epitaxial growth on the substrate. Hence, a few 1 µm thick Er(0.5 %):Y_2O_3 films[6] were deposited on quartz-glass substrates and their properties were compared to those of the films grown on α-Al_2O_3. As indicated by Fig. 6.4g, the highly-textured film growth reported in [Ehl05] was confirmed. The surface morphology of the films deposited on amorphous SiO_2 (Fig. 6.6a) and the ones deposited on α-Al_2O_3 at ambient pressures between 1.8×10^{-4} mbar (Fig. 6.6b) and 7×10^{-3} mbar (Fig. 6.6c) is quite similar. A preferred growth of Y_2O_3 in <111> direction was also observed in [Gab00] and explained by the low surface energy of the {111} planes, which are cleavage planes of the crystal structure.

To investigate the influence of the ambient pressure on the film crystallinity, the crystallite dimensions L were determined with Eq. (5.5) from the widths[7] of the Cu-Kα {222} peaks, scanned at high resolution. The peak widths $\triangle\omega$ of corresponding rocking-curve measurements were determined[8] as well, in order to compare the deviations of the crystallite orientations from the <111> direction. Furthermore, the surface roughness r_{RMS} was determined as root mean square (RMS) of 3 µm × 3 µm sized AFM images. The results are summarized in Fig. 6.5. For ambient pressures ranging from 1.8×10^{-4} to 7×10^{-3} mbar, the crystallites have similar dimensions of 50 to 60 nm. Also the rocking-curve widths of about 1.5 to 2° and surface roughnesses of 2 to 4 nm show no strong dependance on the

---

[4] K36 - K41: $T = 800\,^{\circ}\mathrm{C}$ and $\nu_{\mathrm{r}} = 10\,\mathrm{Hz}$

[5] Not only the intensity maxima resulting from Cu-K_α radiation, but also the ones resulting from the not entirely suppressed Cu-K_β radiation are present in the spectra.

[6] K28 - K31: $T = 800\,^{\circ}\mathrm{C}$, $p_{\mathrm{O}_2} = 3.9 \times 10^{-3} - 4.7 \times 10^{-3}$ mbar and $\nu_{\mathrm{r}} = 10\,\mathrm{Hz}$

[7] The widths were determined as in [Kuz06] with double-peak Gaussian fit functions; the instrumental resolution was taken into account by applying Eq. (5.6).

[8] The widths are defined as FWHM of a simple Gaussian fit function.

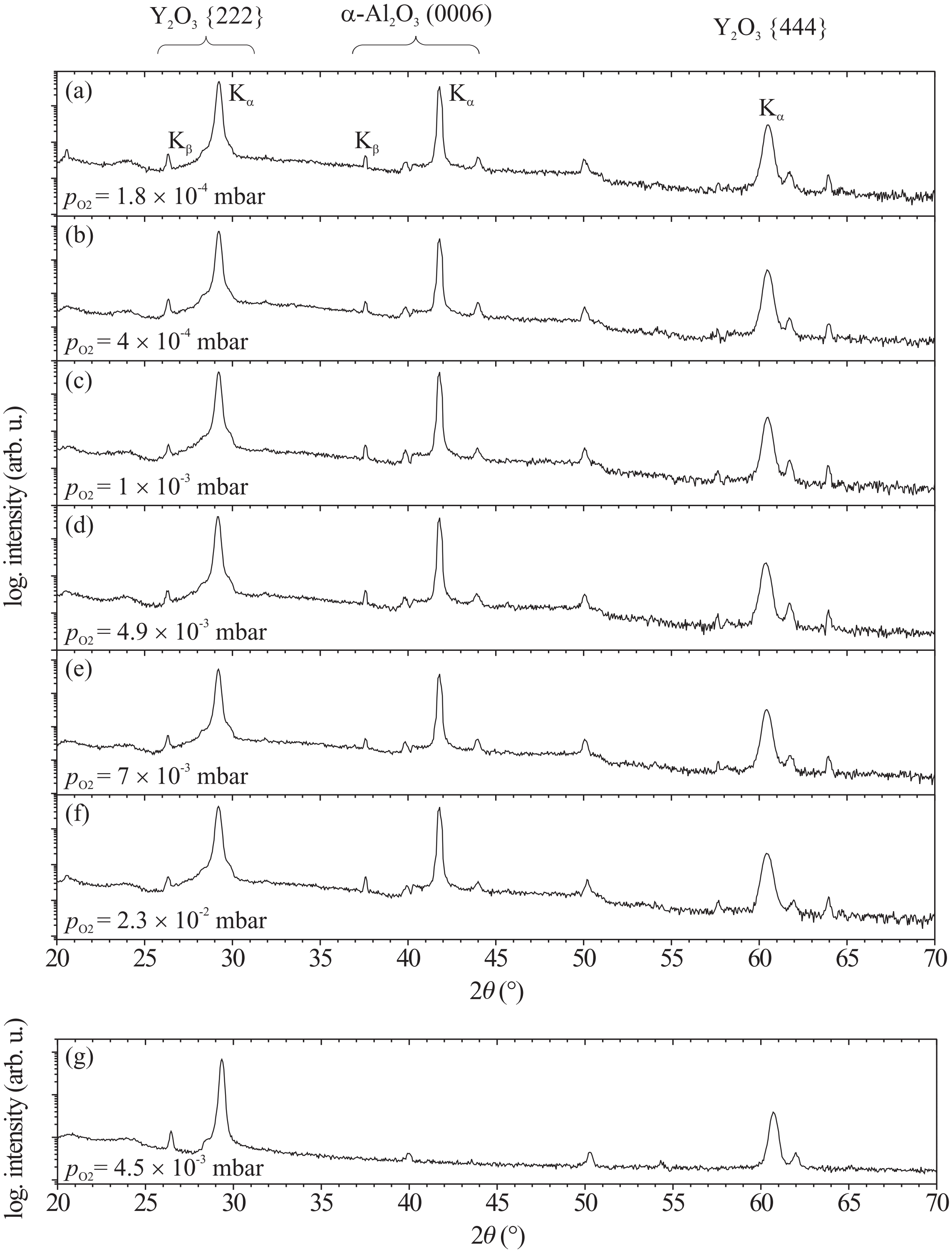

Figure 6.4: Low-resolution XRD spectra: (a)-(f) Er(1 %):Y_2O_3 films, deposited at various ambient pressures p_{O_2} on (0001) oriented α-Al_2O_3 substrates, and (g) an Er(0.5 %):Y_2O_3 film, deposited on amorphous quartz glass

ambient pressure in this pressure range. The films deposited on amorphous SiO_2 possess quite similar properties as well. However, the Y_2O_3 film produced at the highest pressure of 2.3×10^{-2} mbar shows a much higher surface roughness, slightly smaller crystallites and larger deviations of the crystallite orientations from the <111> direction.

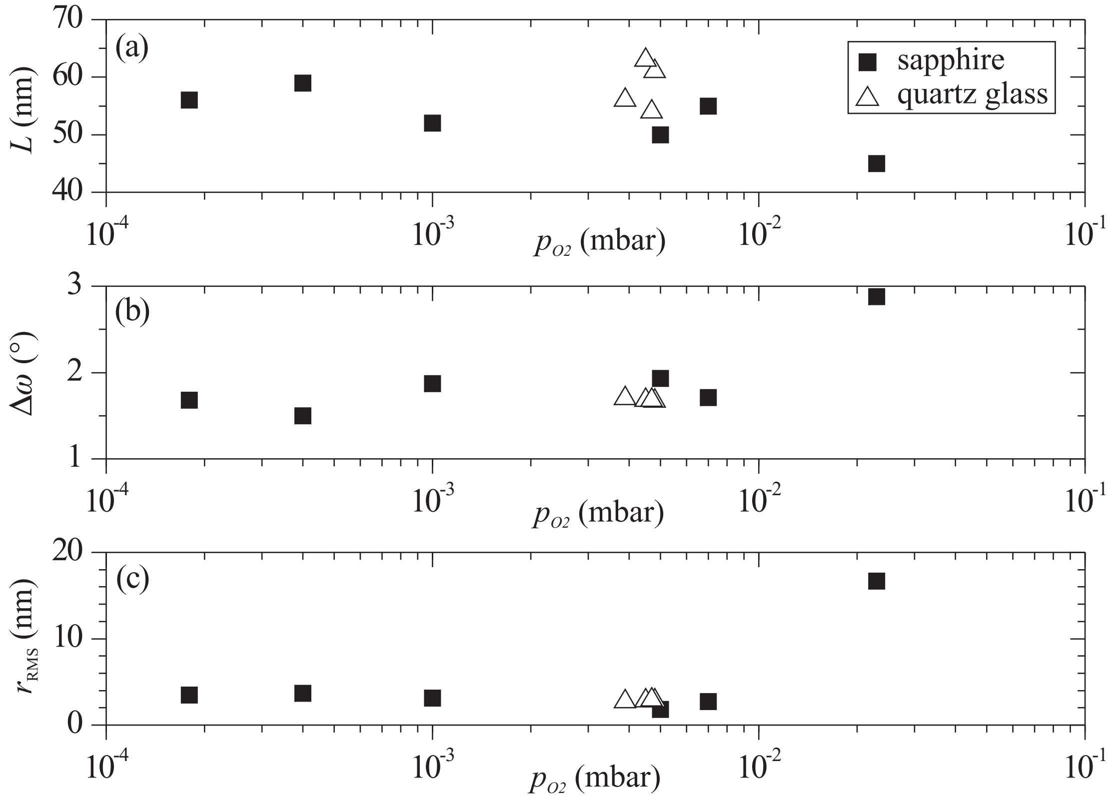

Figure 6.5: Crystallite dimensions L, rocking-curve peak widths $\triangle\omega$ and surface roughnesses r_{RMS} of Er:Y_2O_3 films, deposited at various ambient pressures p_{O_2} on (0001) oriented α-Al_2O_3 (black squares) and amorphous SiO_2 (white triangles) substrates

This change of film properties was also observed in [Kuz06] for Sc_2O_3 and explained by an increasing confinement of the plasma plume with increasing ambient pressure. A shock front, which occurs where plume and background gas pressure are equal, defines the confinement of the plasma plume and separates two different regimes of deposition. Inside the plume the particles have high kinetic energies, which is characteristic for PLD. Outside of the plume, however, the particles are thermalized. At higher ambient pressures, the shock front is formed closer to the target, leaving the substrate in a regime where the deposition has thermal character. Due to the lower particle energy in this thermal deposition regime, the adatoms do not always possess a sufficient surface mobility to reach energetically favored lattice sites, but rather attach to crystallites in their proximity. This results in a lower film density, as observed in [Kuz06], but also in a higher surface roughness.

AFM images of such films, which were deposited in the above mentioned thermal deposition regime, are displayed in Fig. 6.6 (d-f). Crystallites sticking out of the surface as well as indications of a three fold symmetry, which is characteristic for growth in <111> direction, are observable. In addition to the film deposited at 800 °C (Fig. 6.6d) with $L = 45\,\mathrm{nm}$, $\triangle\omega = 2.9^\circ$ and $r_\mathrm{RMS} = 16.7\,\mathrm{nm}$, another film[9] was deposited at 1000 °C (Fig. 6.6e). Due to the increased surface mobility, the crystallinity of this film was higher ($L = 48\,\mathrm{nm}$, $\triangle\omega = 2.0^\circ$) and the surface roughness lower ($r_\mathrm{RMS} = 8.8\,\mathrm{nm}$). A film[10] fabricated with a greatly reduced deposition rate of 1 Hz (Fig. 6.6f) exhibited a significantly higher crystallinity ($L = 96\,\mathrm{nm}$, $\triangle\omega = 1.0^\circ$) and a slightly lower surface roughness ($r_\mathrm{RMS} = 5.8\,\mathrm{nm}$).

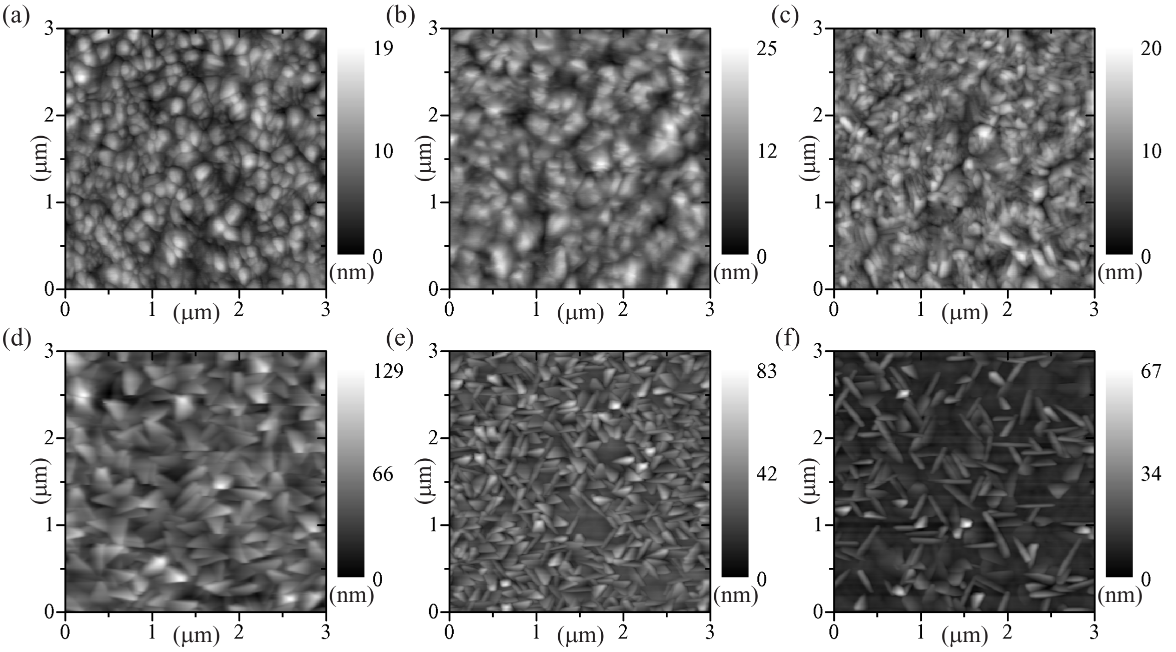

Figure 6.6: AFM images of 1 µm thick Er:Y_2O_3 films: (a) on an amorphous SiO_2 substrate, and (b)-(f) on (0001) oriented α-Al_2O_3 substrates

Since deposition in the non-thermal regime of PLD results in a higher film crystallinity and lower surface roughness (see Fig. 6.5), the influence of the deposition parameters in the thermal deposition regime was not investigated in greater detail. The influence of the substrate temperature and repetition rate on the film crystallinity in the non-thermal regime is examined in [Kue09a]. In this regime, the repetition rate had no significant impact on the film crystallinity. However, higher repetition rates resulted in slightly larger lattice spacings of the deposited films. The expected increase of film crystallinity with the substrate temperature was also shown in [Kue09a].

---

[9] K42: 1 µm Er(0.5 %):Y_2O_3 on α-Al_2O_3, $T = 1000\,^\circ\mathrm{C}$, $p_{O_2} = 2 \times 10^{-2}$ mbar and $\nu_\mathrm{r} = 10\,\mathrm{Hz}$

[10] K43: 1 µm Er(0.5 %):Y_2O_3 on α-Al_2O_3, $T = 1000\,^\circ\mathrm{C}$, $p_{O_2} = 2 \times 10^{-2}$ mbar and $\nu_\mathrm{r} = 1\,\mathrm{Hz}$

In conclusion, growth of the above mentioned sesquioxides on α-Al_2O_3 resulted in highly-textured polycrystalline films. However, the films deposited on amorphous SiO_2 substrates possess similar properties to the ones deposited on α-Al_2O_3 (see Fig. 6.5). The structure of the sapphire substrate therefore has most likely no effect on the crystallinity of the grown films. This is probably due to the amorphous interface, which is created at the beginning of deposition. The formation of the amorphous interface may be prevented by deposition of special buffer layers, possibly allowing for a layer-by-layer growth mode. While such experiments were not carried out within this work, other approaches to obtain a real epitaxial film growth were pursued and are described in the following sections.

6.1.2 Sesquioxide on Sesquioxide Growth

Since deposition on sapphire substrates did not result in monocrystalline films, growth on sesquioxide substrates was investigated as well. In contrast to the ratio of about 3:1 between the lattice spacings for the sesquioxide growth on sapphire, film and substrate possess the same crystal structures and the lattice spacings differ only by the lattice mismatch given in Tab. 6.2. Furthermore, no ordered chemical compounds composed of mixed sesquioxides are expected to occur. Therefore, subplantation should not lead to significant changes of the crystal structure but rather to the formation of a solid solution.

Materials	f	$\triangle n_{1.55\,\mu m}$
Sc_2O_3 on Y_2O_3	-7.57 %	0.074
Lu_2O_3 on Y_2O_3	-2.04 %	0.022
Sc_2O_3 on Lu_2O_3	-5.42 %	0.053

Table 6.2: Lattice mismatch f and refractive index differences $\triangle n_{1.55\,\mu m}$ (at the wavelength $\lambda = 1.55\,\mu m$) for various sesquioxide-on-sesquioxide systems

The highest refractive index difference for heteroepitaxial growth of the above mentioned sesquioxides can be realized with a Sc_2O_3 film on an Y_2O_3 substrate. Hence, this system was investigated in detail. A Nd(0.5 %):Sc_2O_3 film[11] was deposited on an annealed Y_2O_3 substrate and the growth behavior was investigated by RHEED. A {100} oriented substrate was chosen in order to distinguish between film growth in <111> direction, which is usually preferred, and epitaxial film growth in the direction given by the substrate. The resulting diffraction pattern and the intensity behavior of the specular reflected electron beam are displayed in Fig. 6.7. In contrast to the films deposited on sapphire, there are no indications of an amorphous interface. The many parasitic reflexes in the RHEED pattern prior to deposition can be explained by a mosaic structure of the Y_2O_3 substrates, which is probably due to phase transitions of Y_2O_3 occurring during crystal growth.

For the first 1000 pulses, a deposition rate of 1 Hz was chosen and the rate was later increased to fabricate a 3 µm thick film. The first monolayer was growing in a 2D growth

---

[11] K50: $T = 900°C$, $p_{O_2} = 5.1 \times 10^{-3}$ mbar and $\nu_r = 1 - 3$ Hz

mode, as indicated by the intensity oscillation of the (00) reflex. After this, a transition to a 3D growth mode took place, resulting in a spotty diffraction pattern (see also Fig. 6.7). The intensity increase after 50 s of deposition is not related to the intensity of the (00) reflex. It can be explained by the appearance of a 3D diffraction spot at the same position at which the intensity was measured.

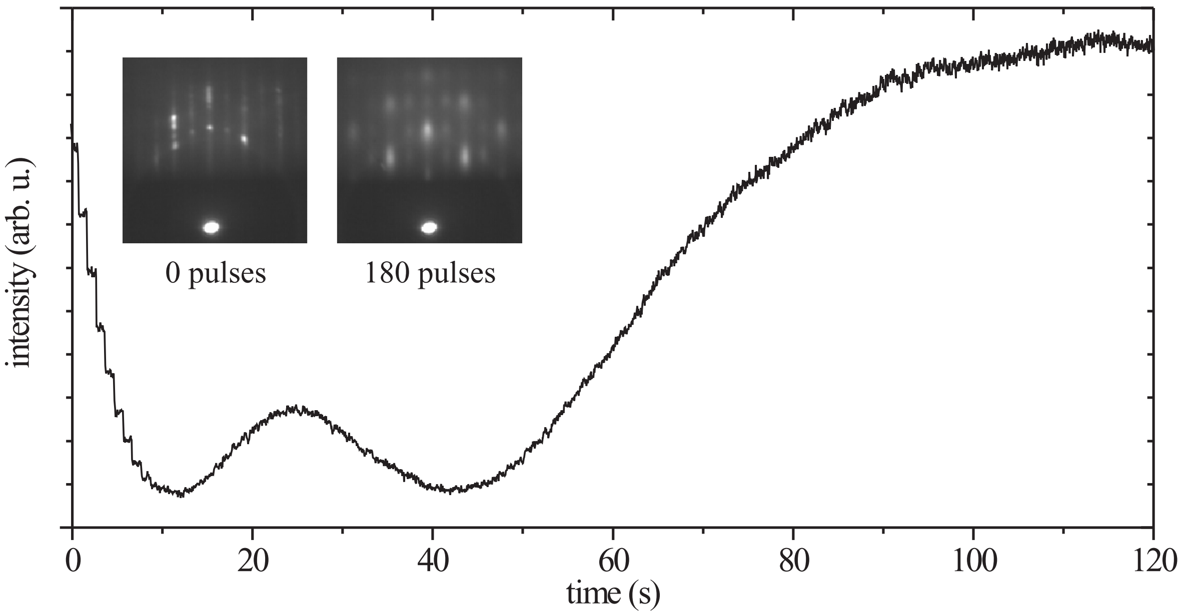

Figure 6.7: RHEED patterns and intensity behavior of the specular reflected electron beam during the growth of Nd(0.5 %):Sc_2O_3 on {100} oriented Y_2O_3 with a repetition rate of 1 Hz

Film growth in <100> direction was verified by XRD measurements. The spectrum of a low-resolution θ-2θ scan is plotted in Fig. 6.8a. Most of the intensity maxima correspond to {100} planes of either the film or substrate material (dashed grey lines). There are no indications of growth in the usually preferred <111> direction. Thus, the growth direction was mainly enforced by the substrate. For comparison, a 3 µm thick Nd(0.5 %):Sc_2O_3 film[12] was deposited on a {111} oriented substrate. Its XRD spectrum is displayed in Fig. 6.8b. The film was mainly grown in <111> direction, as most of the diffraction peaks correspond to {111} planes of either the film or substrate (dashed grey lines). However, some intensity maxima corresponding to other crystallographic orientation were observed. This might be due to the bad quality of some Y_2O_3 substrates, which were not purely {111} oriented, but often consisted to some extend of small regions with other crystallographic orientations. The crystallite dimensions of both films were determined to be at least 300 nm, as the resolution-limit of the XRD setup was reached.

---

[12] K49: $T = 900\,^\circ\mathrm{C}$, $p_{\mathrm{O}_2} = 5.1 \times 10^{-3}$ mbar and $\nu_\mathrm{r} = 1 - 3$ Hz

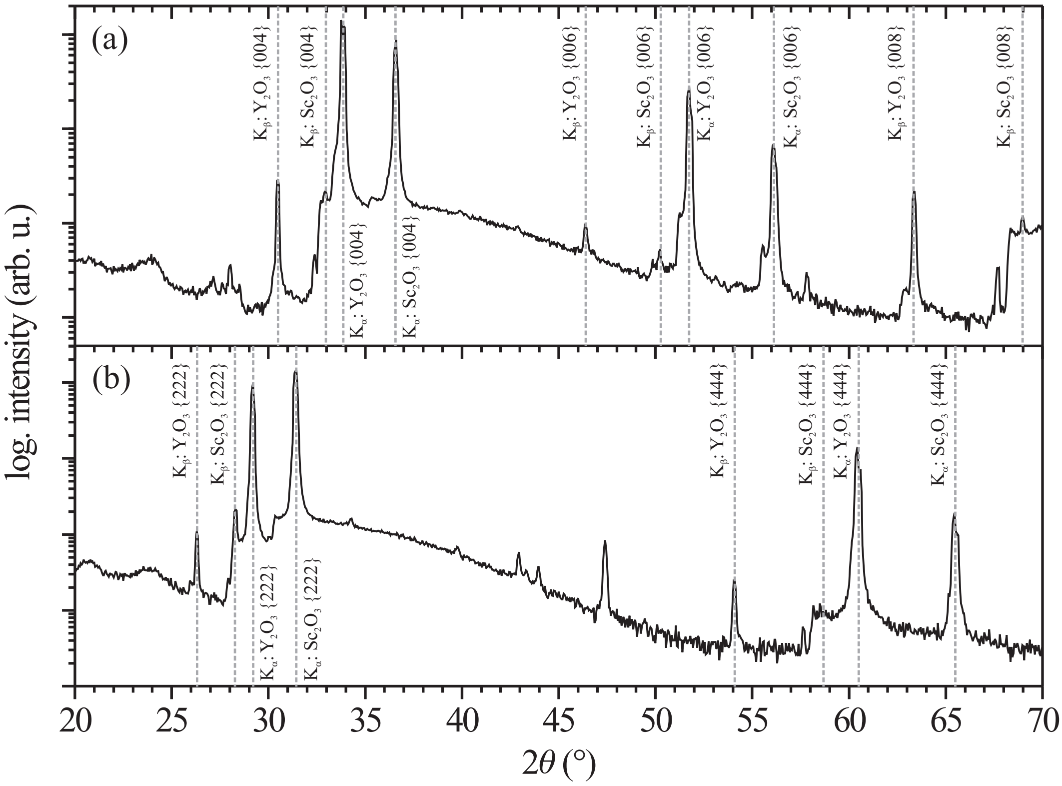

Figure 6.8: Low-resolution XRD spectra of Nd(0.5 %):Sc_2O_3 films, deposited on (a) a {100} oriented and (b) a {111} oriented Y_2O_3 substrate

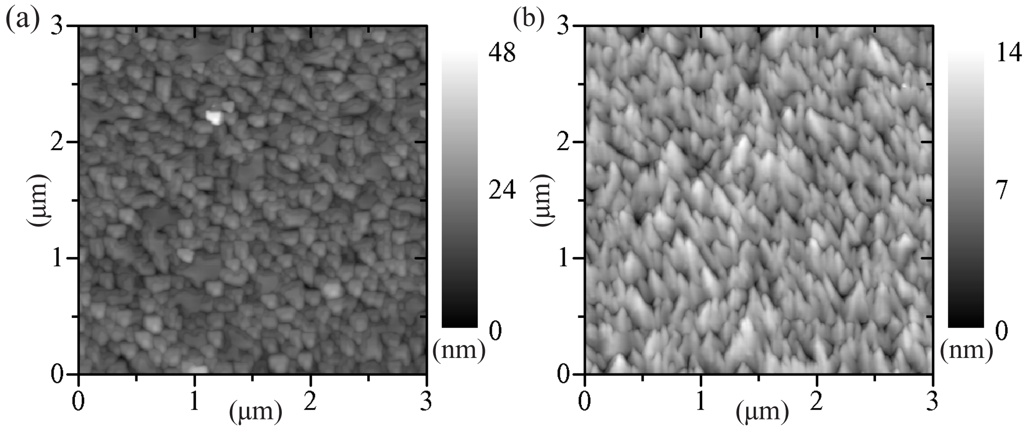

Figure 6.9: AFM images of 3 µm thick Nd(0.5 %):Sc_2O_3 films, deposited on (a) a {100} oriented and (b) a {111} oriented Y_2O_3 substrate

Surface roughnesses of 3.5 nm and 1.7 nm were determined by AFM measurements (see Fig. 6.9) for the {100} and {111} oriented films, respectively.[13] These values are comparable to those of films deposited on α-Al_2O_3 substrates. However, cracks were located all over the {100} oriented film (see Fig. 6.10a). Their formation seems to be reproducible, as such cracks were also observed for a previously fabricated 3 µm thick Nd(0.5 %):Sc_2O_3 film[14], which was deposited on a {100} oriented Y_2O_3 substrate as well (see Fig. 6.10b).

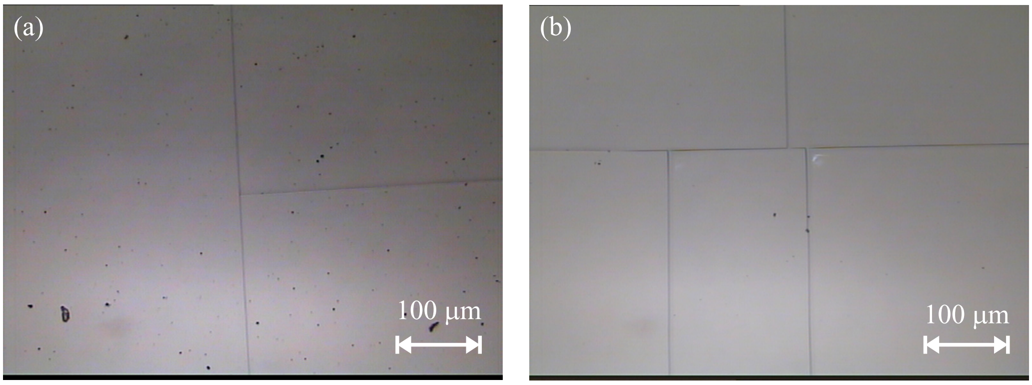

Figure 6.10: Optical microscope images of two 3 µm thick Nd(0.5 %):Sc_2O_3 films, deposited on {100} oriented Y_2O_3 substrates

Since the cracks are perpendicular to each other, they are most likely occurring along a <100> direction. However, no cracks were observed for the {111} oriented film. This is possibly due to a higher mechanical stability of the film, which was grown in the energetically preferred growth direction of the investigated sesquioxides. The cracks are an indication of the tensile stress caused by the high lattice mismatch between Sc_2O_3 and Y_2O_3. Less stress should be induced during growth of Lu_2O_3 on Y_2O_3, as the lattice mismatch is much smaller.

For such films, the initial 2D growth mode might be sustained for a longer time, possibly for the entire growth. This should result in films with a higher mechanical stability. However, Lu_2O_3 growth on Y_2O_3 was not investigated within this thesis, which focusses on the epitaxial grown lattice matched films discussed in the following section.

6.1.3 Lattice Matched Films

While epitaxial layer-by-layer growth was realized in [Gue07b] for homoepitaxial grown Sc_2O_3 films on Sc_2O_3 substrates, the 2D growth mode was not sustained during deposition of Sc_2O_3 on Y_2O_3. While a low lattice mismatch is beneficial for the growth process, a positive refractive index difference and thus heteroepitaxial growth is required for the realization of waveguiding films. Therefore, the growth of lattice matched films, which were realized by mixing sesquioxides with different lattice constants, was investigated.

---

[13] These values were determined for 3 µm × 3 µm large surface areas.

[14] K48: $T = 900\,°C$, $p_{O_2} = 5.1 \times 10^{-3}$ mbar and $\nu_r = 1 - 3$ Hz

It has been shown in [Veg21] that such mixed crystals can be described as solid solutions with a completely disordered substituent distribution among the available lattice sites. For a binary solution, like $(\mathrm{Gd}_x, \mathrm{Lu}_{1-x})_2\mathrm{O}_3$, the lattice constant a' can be calculated from the lattice constants a_1 and a_2 of the respective single crystals by applying Vegard's law [Veg21]:

$$a' = x\, a_1 + (1 - x)\, a_2 \tag{6.1}$$

For the determination of appropriate film compositions, the concentration x_d and lattice constant a_d of the rare-earth oxide used as dopant have to be taken into account as well, which results in concentrations of x and $(1 - x - x_d)$ for the other components:

$$a' = x\, a_1 + (1 - x - x_d)\, a_2 + x_d\, a_d \tag{6.2}$$

Since the lattice constant of $\mathrm{Y_2O_3}$ is between those of $\mathrm{Lu_2O_3}$ and $\mathrm{Gd_2O_3}$, lattice matching of $(\mathrm{Gd, Lu})_2\mathrm{O}_3$ films on $\mathrm{Y_2O_3}$ substrates should be possible. A positive refractive index difference between film and substrate is expected, as the refractive index of both $\mathrm{Lu_2O_3}$ and $\mathrm{Gd_2O_3}$ is higher than the one of $\mathrm{Y_2O_3}$. Hence, this work focusses on RE doped $(\mathrm{Gd, Lu})_2\mathrm{O}_3$ films deposited on $\mathrm{Y_2O_3}$ substrates.

First, a $(\mathrm{Nd}_{0.005}, \mathrm{Gd}_{0.479}, \mathrm{Lu}_{0.516})_2\mathrm{O}_3$ film[15] was deposited on an annealed {100} oriented $\mathrm{Y_2O_3}$ substrate and the growth was monitored by RHEED [Gue08]. In order to compensate for a systematic shift to larger lattice constants, which had been observed in [Ile08], the $\mathrm{Lu}^{3+}/\mathrm{Gd}^{3+}$ ratio was increased by about 3 % with respect to the values calculated for perfect lattice matching.

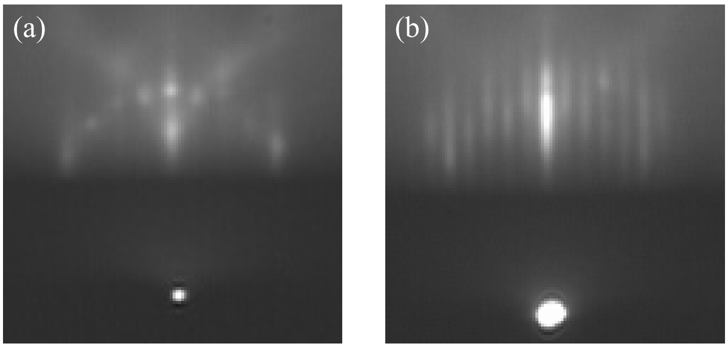

Figure 6.11: RHEED patterns (a) of an annealed {100} oriented $\mathrm{Y_2O_3}$ substrate, and (b) after deposition of a 1 µm thick lattice matched $\mathrm{Nd}(0.5\,\%){:}(\mathrm{Gd, Lu})_2\mathrm{O}_3$ film

---

[15] K47: $T = 900\,°\mathrm{C}$, $p_{\mathrm{O}_2} = 8.8 \times 10^{-3}\,\mathrm{mbar}$ and $\nu_\mathrm{r} = 1\,\mathrm{Hz}$

Figure 6.11a shows the diffraction pattern prior to deposition, which indicates a nearly atomically flat substrate surface.[16]

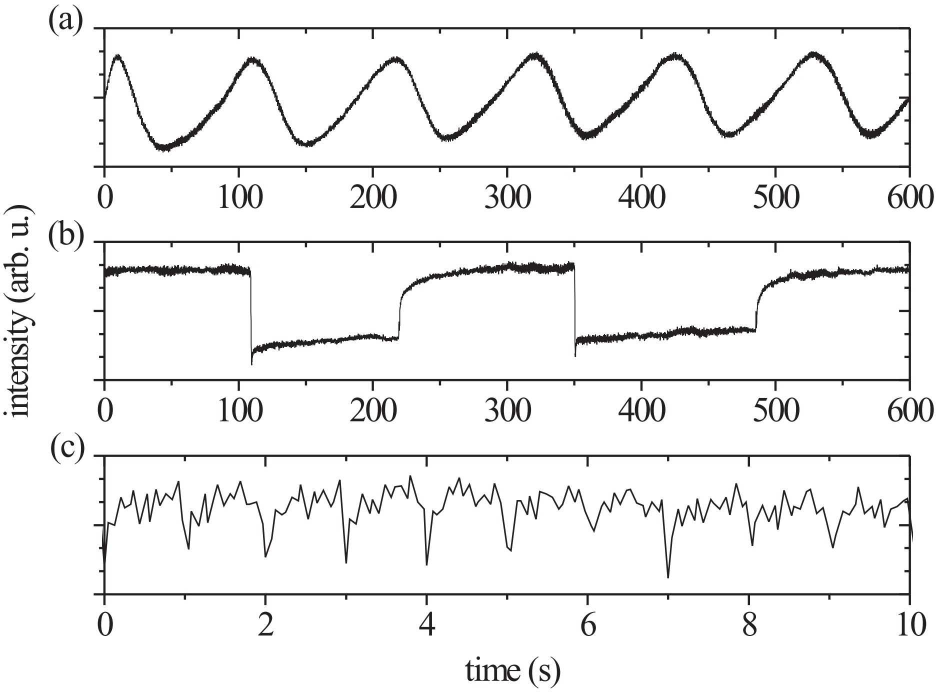

Figure 6.12: Intensity behavior of the specular reflected electron beam during deposition of a lattice matched Nd(0.5 %):$(Gd, Lu)_2O_3$ film on a {100} oriented Y_2O_3 substrate: (a) at the beginning of the growth, (b) during interval growth, and (c) detailed view of the small intensity variations at about 1 µm film thickness

Intensity oscillations of the specular reflected electron beam (see Fig. 6.12a) were observed during the continuous deposition (1 Hz repetition rate) at the beginning of the growth. These oscillations, confirming a 2D layer-by-layer growth, were sustained up to a film thickness of about 100 nm. Afterwards, the RHEED oscillations were damped more and more and finally vanished, indicating a multilevel 2D growth, caused by a premature nucleation of the adatoms. It has been demonstrated in [Kos99], that the probability for premature nucleation can be reduced by using pulsed laser interval deposition; the amount of material needed for the completion of one monolayer is deposited in a short time interval and the deposition is then stopped for a certain recovery time. In order to sustain layer-by-layer growth for a longer time, this technique was also applied several times during the first 100 nm of $(Gd, Lu)_2O_3$ film growth. For the demonstration of the layer-by-layer growth mode (see Fig. 6.12b), only 51 pulses were applied in each deposition interval, the amount needed for deposition of half a monolayer.[17]

---

[16] This was also verified by AFM measurements, showing nearly atomically flat terraces with widths of almost 100 nm and step heights of about 5 Å, which is according to [Gue07b], the height of one Y_2O_3 monolayer.

[17] At the beginning, 102 pulses were needed for the completion of one monolayer (one RHEED oscillation during continuous growth), which corresponds to a deposition rate of about 0.005 nm/pulse. However, the deposition rate changes slowly over time with the target properties.

The material packets were deposited with a repetition rate of 50 Hz, followed by a recovery time of about 100 s. While the deposition of one packet led to a intensity decrease of the (00) reflex, the deposition of two packets resulted in a total intensity recovery, as another monolayer was completed.

No change of symmetry was observed in the RHEED pattern during the entire deposition. This indicates an epitaxial film growth in <100> direction. However, due to the 2D multilevel film growth and thus an increasing surface roughness, the reflections on the first-order Laue circle became more streaky. The RHEED pattern of the 1 µm thick film, confirming a monocrystalline growth, is displayed in Fig. 6.11b and the intensity behavior of the specular reflected beam close to the end of deposition is illustrated in Fig. 6.12c. A relaxation after each pulse was observed, which is possibly due to adatoms diffusing to the step edges (quasi step-flow growth). However, since a similar behavior was observed for the non-diffracted (000) reflex as well, it might also be the result of a measurement artefact.

The multilevel surface structure of the 1 µm thick film, which was indicated by the RHEED measurements, was verified by AFM (see Fig. 6.13), showing nearly atomically flat terraces and step edges with heights of single monolayers (5 Å). A surface roughness r_{RMS} of approximately 0.7 nm was determined,[18] which is remarkably flat for a 1 µm thick heteroepitaxially grown monocrystalline dielectric film.

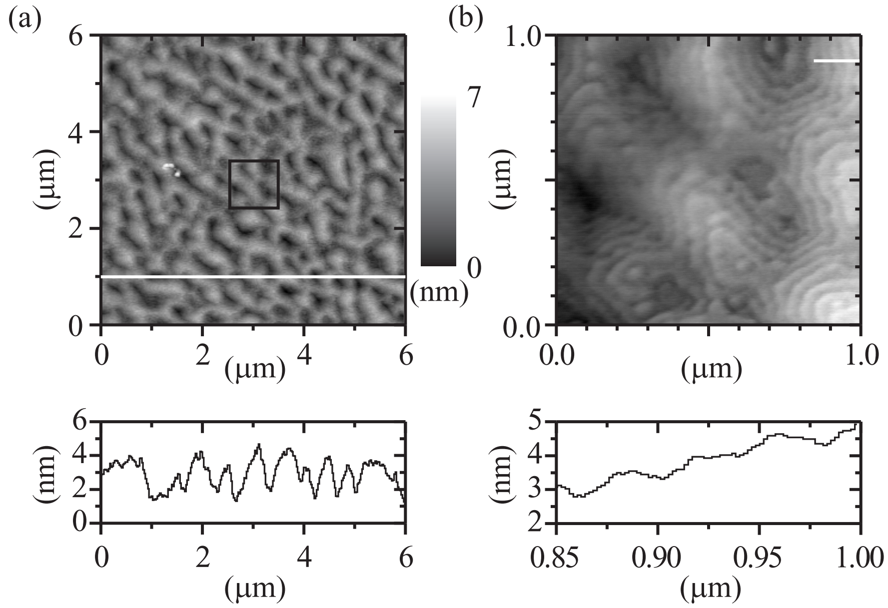

Figure 6.13: AFM images of a monocrystalline 1 µm thick lattice matched Nd(0.5 %):$(\mathrm{Gd,Lu})_2\mathrm{O}_3$ film, deposited on a {100} oriented $\mathrm{Y}_2\mathrm{O}_3$ substrate. The corresponding height profiles are taken along the paths marked with white lines. Image (b) shows the section indicated by the black rectangle in greater detail.

---

[18] The roughness was determined for a 1 µm × 1 µm large surface area.

Growth in <100> direction was also verified by XRD measurements, as indicated by the θ-2θ low-resolution scan plotted in Fig. 6.14a. A high-resolution scan of the K_α {600} peaks is displayed in Fig. 6.14b. The full width at half maximum of corresponding film and substrate peaks is similar, which indicates that the instrumental resolution of the XRD setup was reached and corroborates the monocrystallinity of the film. Although the film composition was adjusted to compensate for a lattice expansion, the K_{α_1} film peak is still shifted by -0.5° in comparison to the corresponding substrate peak. However, the lattice matching of 99.3 % between film and substrate, which was determined with Eq. (5.3) from the peak positions, is identical to the one obtained for a film which was composed without adjusting the Lu^{3+}/Gd^{3+} ratio (see Fig. 6.17). Since monocrystalline films could be reproducibly fabricated and this work focusses on the realization of waveguide devices, the lattice expansion was not further investigated. Hence, the Lu^{3+}/Gd^{3+} ratio of subsequent films was not adjusted and the films were composed as calculated with Eq. (6.2).

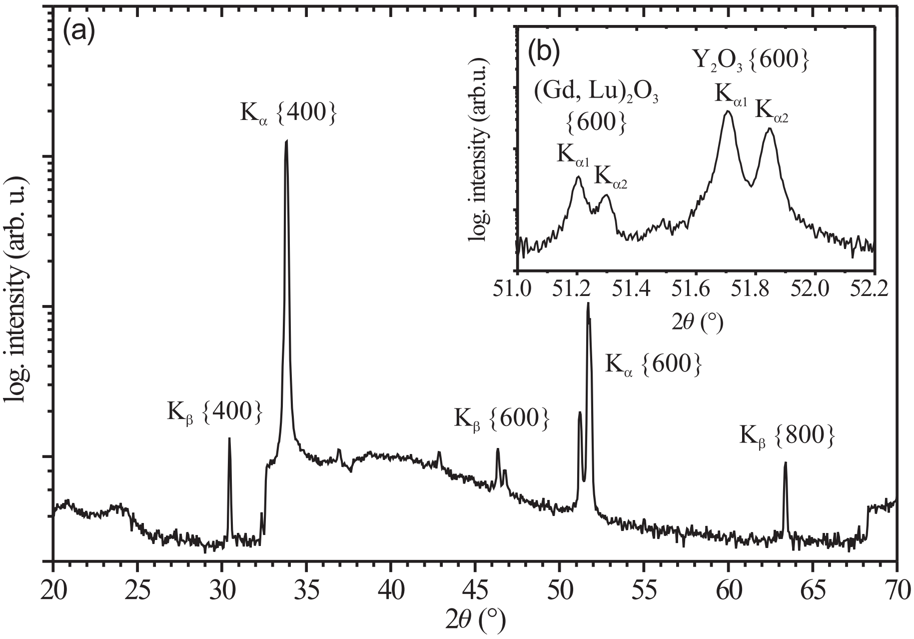

Figure 6.14: XRD spectra of a monocrystalline 1 µm thick lattice matched Nd(0.5 %):$(Gd, Lu)_2O_3$ film, deposited on a {100} oriented Y_2O_3 substrate: (a) low-resolution scan, (b) high-resolution scan

In order to fabricate several micrometer thick films in a reasonable time, a higher pulse repetition rate is required. The influence of the repetition rate was investigated during growth of a $(Nd_{0.005}, Gd_{0.487}, Lu_{0.508})_2O_3$ film[19], deposited on a {100} oriented Y_2O_3 substrate.

RHEED oscillations of the specular reflected electron beam were observed for repetition rates ν_r up to 8 Hz (see Fig. 6.15). The number of completed oscillation periods in each 225 s long time interval shown in Fig. 6.15 is proportional to ν_r, which indicates that

---

[19] K70: $T = 900\,°C$, $p_{O_2} = 8.8 \times 10^{-3}$ mbar and $\nu_r = 1 - 12$ Hz

the growth rate per pulse remains constant. At $\nu_\mathrm{r} = 8\,\mathrm{Hz}$ the RHEED oscillations were strongly damped and vanished at a film thickness of about 20 nm, thus much earlier than for the film described in the preceding paragraphs, which was fabricated with $\nu_\mathrm{r} = 1\,\mathrm{Hz}$. During the following growth at a repetition rate of 12 Hz, the diffraction pattern became more and more streaky. The growth mode at the end of deposition was not clearly distinguishable and no atomic step-structure was observed by AFM. This is not necessarily a result of the high repetition rate, but might also be due to the bad quality of the Y_2O_3 substrate. However, the 1 µm thick film possessed an extremely low surface roughness of $r_\mathrm{RMS} \approx 0.5\,\mathrm{nm}$.[20]

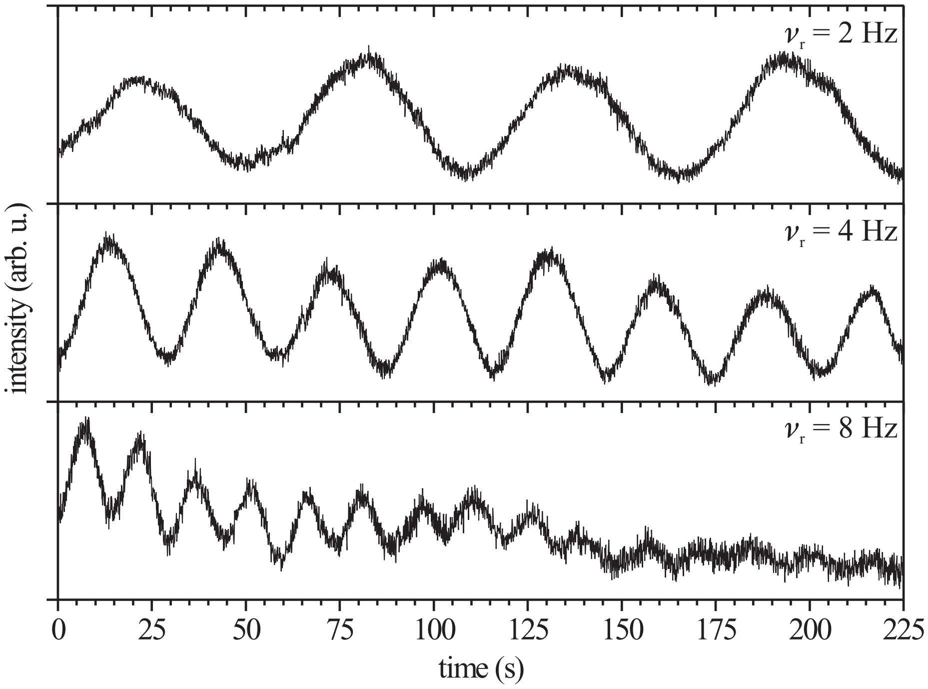

Figure 6.15: Intensity behavior of the specular reflected electron beam during deposition of a Nd(0.5 %):$(\mathrm{Gd,Lu})_2O_3$ film on a {100} oriented Y_2O_3 substrate. At the three displayed time intervals, different pulse repetition rates ν_r were used.

Epitaxial growth of monocrystalline Nd^{3+} and Er^{3+} doped $(\mathrm{Gd,Lu})_2O_3$ films on Y_2O_3 substrates has been reproducibly realized up to a thickness of 3.1 µm. This value is most likely not the upper limit, but no further investigation were made regarding the scalability of the film thickness. The 3.1 µm thick $(\mathrm{Er}_{0.006}, \mathrm{Gd}_{0.494}, \mathrm{Lu}_{0.500})_2O_3$ film[21], however, which was deposited with a repetition rate of 5 Hz on a {100} oriented Y_2O_3 substrate, possesses an excellent surface flatness (see Fig. 6.17a) and film crystallinity (see Figs. 6.17b and 6.16). It is therefore most likely that the thickness of epitaxially grown monocrystalline films can be further increased.

---

[20] This value was determined for a 1 µm × 1 µm large surface area.

[21] K59: $T = 900\,^\circ\mathrm{C}$ and $p_{O_2} = 9 \times 10^{-3}\,\mathrm{mbar}$

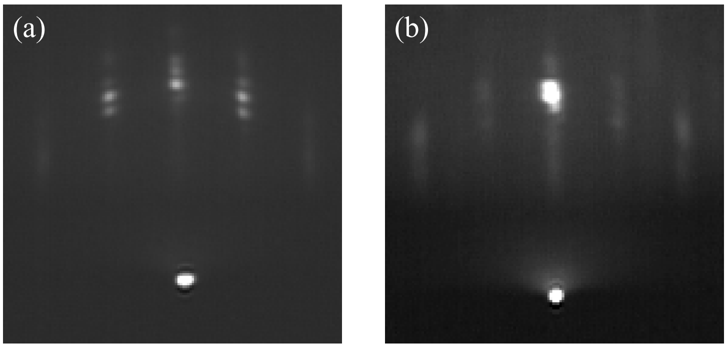

Figure 6.16: RHEED patterns: (a) of an annealed {100} oriented Y_2O_3 substrate, and (b) after deposition of a 3.1 µm thick lattice matched Er(0.6 %):$(Gd, Lu)_2O_3$ film

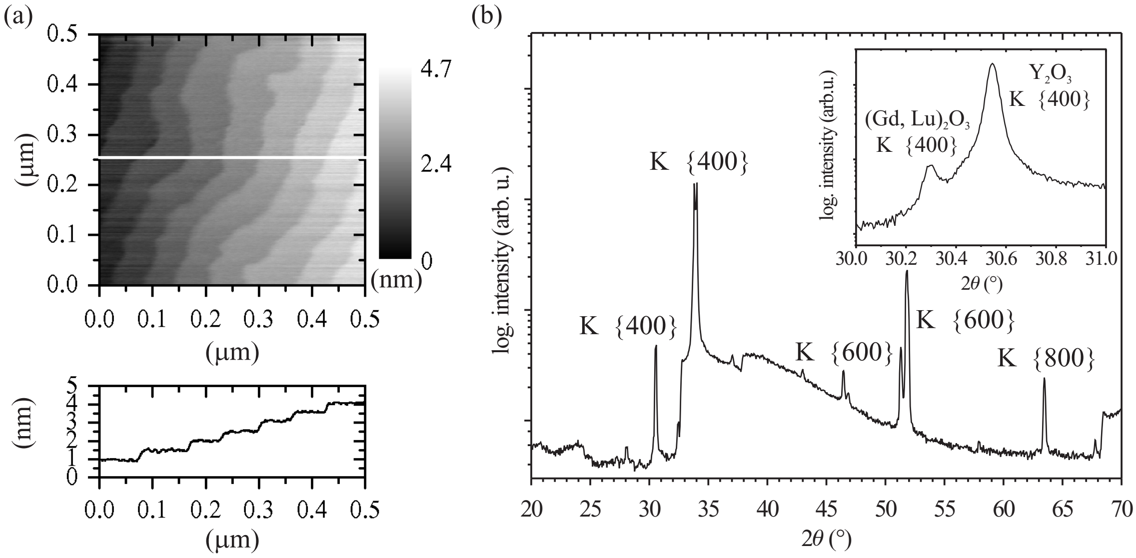

Figure 6.17: Structural measurement results for a monocrystalline 3.1 µm thick lattice matched Er(0.6 %):$(Gd, Lu)_2O_3$ film, deposited on a {100} oriented Y_2O_3 substrate: (a) AFM image with corresponding height profile taken along the path marked with a white line, (b) XRD spectra of the film. A lattice matching of 99.3 % was determined from the high-resolution scan displayed in the inset.

Merging of two components with perfect solubility has thus been proven to be suitable to obtain nearly perfect lattice matching and to fabricate epitaxially grown monocrystalline films with thicknesses of several micrometers. Deposition of $(\mathrm{Gd},\mathrm{Lu})_2\mathrm{O}_3$ films on $\mathrm{Y}_2\mathrm{O}_3$ substrates was investigated, since the lattice constants of the film components do not vary significantly from those of the substrate material. Due to the problems during the growth of $\mathrm{Y}_2\mathrm{O}_3$ crystals (see section 3.1.1), however, the available $\mathrm{Y}_2\mathrm{O}_3$ substrates were of worse crystal quality than the available $\mathrm{Sc}_2\mathrm{O}_3$ and $\mathrm{Lu}_2\mathrm{O}_3$ substrates. Comparing the diffraction patterns of an annealed $\mathrm{Y}_2\mathrm{O}_3$ and $\mathrm{Lu}_2\mathrm{O}_3$ substrate, reveals the different quality. While a clear Laue circle of relatively sharp diffraction peaks can be observed for the $\mathrm{Lu}_2\mathrm{O}_3$ substrate (see left inset of Fig. 6.18), multiple reflexes belonging to different slightly shifted Laue circles are present in the RHEED pattern of the $\mathrm{Y}_2\mathrm{O}_3$ substrate (see Fig. 6.16a). Hence, growth of lattice matched $(\mathrm{Gd},\mathrm{Sc})_2\mathrm{O}_3$ films on $\mathrm{Lu}_2\mathrm{O}_3$ substrates was investigated as well.

For this, a $(\mathrm{Er}_{0.006},\mathrm{Gd}_{0.557},\mathrm{Sc}_{0.437})_2\mathrm{O}_3$ film[22] was deposited on a {100} oriented $\mathrm{Lu}_2\mathrm{O}_3$ substrate and the growth was monitored by RHEED (see Fig. 6.18). RHEED oscillations and thus layer-by-layer growth were observed for a couple of monolayers only. Afterwards, a spotty diffraction pattern (see right inset of Fig. 6.18) indicated a 3D growth mode.

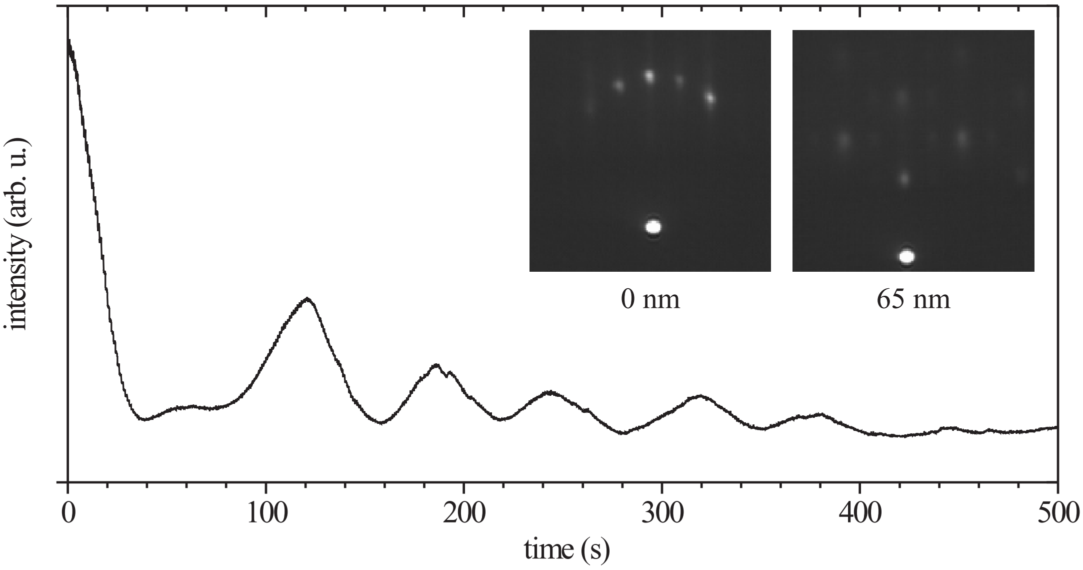

Figure 6.18: Intensity behavior of the $(0\bar{2})$ reflex during growth of an Er(0.6 %):$(\mathrm{Gd},\mathrm{Sc})_2\mathrm{O}_3$ film on a {100} oriented $\mathrm{Lu}_2\mathrm{O}_3$ substrate, as well as the diffraction patterns before deposition and at a film thickness of 65 nm

The different growth behavior of $(\mathrm{Gd},\mathrm{Sc})_2\mathrm{O}_3$ in comparison to $(\mathrm{Gd},\mathrm{Lu})_2\mathrm{O}_3$ may be explained by the lattice constants of its components $\mathrm{Gd}_2\mathrm{O}_3$ and $\mathrm{Sc}_2\mathrm{O}_3$, which differ more than those of $\mathrm{Gd}_2\mathrm{O}_3$ and $\mathrm{Lu}_2\mathrm{O}_3$. Figure 6.19 shows the surface morphology of the 2 µm thick film, confirming the 3D growth mode. Due to a long time breakdown of the XRD setup, the growth direction and texture of the film has not been examined by use of X-Ray diffraction.

---

[22] K66: $T = 900\,^\circ\mathrm{C}$, $p_{\mathrm{O}_2} = 9 \times 10^{-3}\,\mathrm{mbar}$ and $\nu_\mathrm{r} = 1\,\mathrm{Hz}$

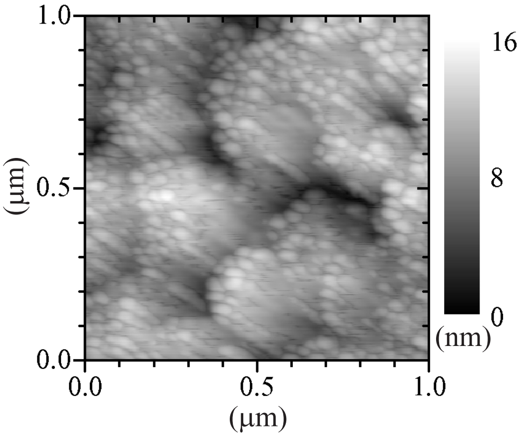

Figure 6.19: AFM image of a 2 µm thick Er(0.6 %):$(Gd, Sc)_2O_3$ film deposited on a {100} oriented Lu_2O_3 substrate

6.1.4 Particulates

A major disadvantage of PLD is the generation of particulates with dimensions ranging from sub-micrometer to several micrometers. Both molten droplets and solid particles can be ejected from the target during pulsed laser ablation. Common mechanisms for particulate generation, as described in [Sae93b], are: splashing due to evaporation of a sub-surface layer, ejection of molten droplets by the recoil pressure of the vaporized material, expulsion by bubbles of trapped expanding gas, and emission from micro-cracks in the target resulting from laser-induced thermal shock. Furthermore, particulates can be created by interaction of the plume species with each other or with the background gas. In the following, all parasitic higher mass species both solid particles and molten droplets are called particulates. Such particulates not only have an adverse effect on the growth of subsequent film layers, but most likely also act as scattering centers increasing the optical waveguide losses. Thus, the fabrication of high quality waveguides with PLD requires an optimization of the process parameters in order to reduce the particulate generation.

It has been reported in [Kor89] that ablation with ultraviolet radiation results in a lower particulate content than ablation at longer laser wavelengths. Thus, in the framework of this thesis, an ultraviolet laser was used for film fabrication. Crater formation in the target was identified by [Bec88] as a possible reason for an increased particulate generation. Therefore, as proposed in [Jac94], the laser focus was continuously scanned to irradiate a different part of the target with each laser pulse. In order to prevent splashing of molten droplets, laser fluences just slightly above the ablation threshold were used.

Figure 6.20 shows a scanning electron microscope (SEM) image of a typical particulate located on a 1 µm thick Er(0.5 %):Y_2O_3 film[23], which was deposited on a (0001) oriented α-Al_2O_3 substrate. The presence of yttrium, oxygen, nitrogen and aluminum was observed by energy dispersive X-ray analysis (EDX), with the electron beam focussed onto the

---

[23] K12: $T = 800\,°C$, $p_{O_2} = 3 \times 10^{-3}$ mbar and $\nu_r = 10\,Hz$

particulate. Beside the nitrogen used for flooding the SEM vacuum chamber and the elements of the film and substrate composition, no other elements were detected.

The films typically exhibited particulate densities between $10^3\,\mathrm{cm}^{-2}$ and $10^5\,\mathrm{cm}^{-2}$. These densities were estimated from optical microscopy images, as described in [Han07]. Since a lower particulate generation was expected for dense targets and for those with smooth surfaces [Chr94], the influence of the target properties was investigated as well. However, both sintered powder targets and targets made of bulk crystals resulted in comparable particulate densities. This indicates that the pressed and sintered powder targets used in this work were of sufficient quality regarding the particulate prevention.

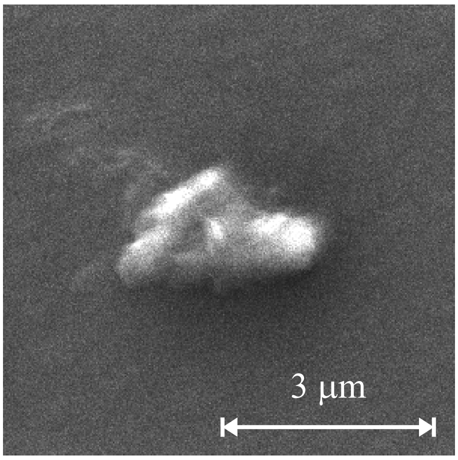

Figure 6.20: SEM image of a typical particulate

Although particulate generation can be reduced by operating at optimal process parameters, it is most likely not entirely preventable. The particulate content can, however, be further reduced by preventing the particulates to reach the film. A number of schemes have been developed for this purpose, such as those described in [Sae93a]: Mechanical chopping to filter out the low velocity particulates, in-flight vaporization of particulates by a secondary laser pulse, and arrangements of intersecting plumes for selective deflection of non-particulates onto the substrate. While the implementation of a velocity filter [Bar69] is in progress, none of these techniques for an active particulate reduction were employed during film fabrication within the framework of this thesis.

Due to the high refractive index difference at the interface between the waveguiding film and the surrounding air, light scattering at particulates is expected to occur mostly at the waveguide surface. An analysis of the reflectometer signal during PLD in [Kuz06] also indicated that most scattering takes place at the film surface. In order to bury particulates which are sticking out of the surface and thus to reduce the scattering losses, some of the films were covered with an amorphous top cladding. The effect of such a cover layer on the waveguide losses is described in section 7.4.

6.2 Spectroscopic Characterization

The spectroscopic properties of Er^{3+} and Nd^{3+} doped films belonging to the different material systems described in section 6.1 were investigated and compared with the ones of correspondingly doped bulk crystals. Both polycrystalline and monocrystalline films were investigated in order to determine the influence of the crystallinity on the fluorescence lifetimes as well as on the absorption and emission cross-sections. The experimental procedures and measurement setups are described in section 5.4.

6.2.1 Er^{3+} Doped Films

Fluorescence Lifetimes

The fluorescence lifetime τ of the ${}^4I_{13/2}$ (Er^{3+}) manifold was determined from the fluorescence decay curves[24] of ${}^4I_{13/2} \rightarrow {}^4I_{15/2}$ transitions upon pulsed excitation at 974 nm. To investigate the influence of the Er^{3+} concentration, several 1 µm thick polycrystalline $Er:Y_2O_3$ films[25] with different Er^{3+} concentrations were deposited on α-Al_2O_3 substrates and examined. The measured lifetimes of 6.9 to 7.8 ms are displayed in Fig. 6.21. The slight increase of the measured values with the erbium concentration is most likely due to an increasing impact of radiation trapping[26] [Auz07]. However, at Er^{3+} concentrations above 0.5 % the measured lifetime remains nearly constant and even decreases slightly for the highest concentration of 2 %. This is most probably due to the ${}^4I_{13/2}$, ${}^4I_{13/2} \rightarrow {}^4I_{9/2}$, ${}^4I_{15/2}$ upconversion process (see Fig. 7.15), which reduces the lifetime and thus compensates the increase of the measured values by radiation trapping. Indeed, an upconversion fluorescence at 980 nm was observed for the films with Er^{3+} concentrations of at least 0.4 % upon pulsed excitation at 1.55 µm. In order to estimate the intrinsic fluorescence lifetime without reabsorption artifacts, the measured values for Er^{3+} concentrations between 0.1 % and 0.4 % were extrapolated[27] to a concentration of 0 % (see inset of Fig. 6.21). This resulted in a lifetime of about 6.6 ms.

The measured lifetimes are in good agreement with the room temperature lifetime of 7.2 ms measured in [Hoe93] for a sputtered Er(0.2 %):Y_2O_3 film and in [Mer07] for an Er(0.5 %):Y_2O_3 ceramic, as well as the radiative $Er:Y_2O_3$ lifetime of (8 ± 2) ms calculated in [Web68] with the Judd–Ofelt method. A good accordance between bulk and film lifetimes was also observed for $Er:Sc_2O_3$. The fluorescence lifetimes of 5.8 ms and 6.3 ms measured in [Fec07b] for a 0.1 % and 0.3 % doped $Er:Sc_2O_3$ film on α-Al_2O_3 are comparable

---

[24] The lifetimes of the Er^{3+} doped films were determined with a double exponential fit function taking both the ${}^4I_{13/2}$ and ${}^4I_{11/2}$ lifetimes into account.

[25] K11 (0.1 %), K14 (0.2 %), K18 (0.3 %), K17 (0.4 %), K16 (0.5 %), K19 (0.6 %), K20 (0.8 %), K21 (1.0 %), and K24 (2.0 %): $T = 800\,°C$, $p_{O_2} = 3 \times 10^{-3}$ mbar and $\nu_r = 10$ Hz

[26] Radiation trapping denotes an effect which is due to reabsorption of spontaneously emitted photons and causes the measured fluorescence lifetime to be longer than the intrinsic fluorescence lifetime of an isolated ion.

[27] In contrast to the linear fit function justified by the pinhole method [Kue07], which is not taking the upconversion process into account, a second order polynomial fit function was applied.

with the 6.2 ms and 6.3 ms determined in [Pet98] for a 0.2 % and 0.41 % doped Er:Sc_2O_3 bulk crystal, respectively. Since these values were not corrected by taking reabsorption into account, the intrinsic Er:Sc_2O_3 lifetime is expected to be slightly smaller than the value of 5.8 ms measured for the lowest concentration sample.

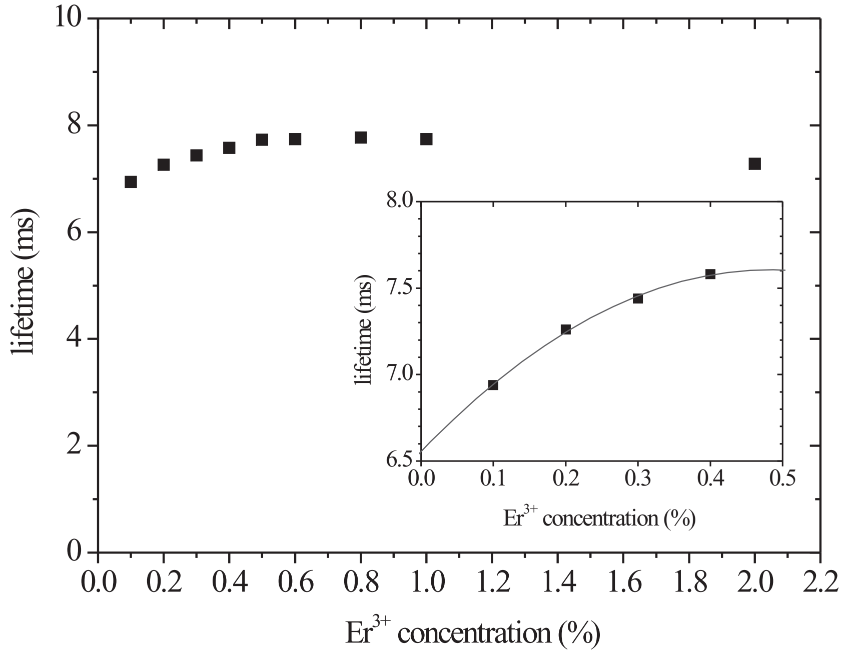

Figure 6.21: Measured $^4I_{13/2}$ (Er^{3+}) fluorescence lifetimes of various polycrystalline Er:Y_2O_3 films with different Er^{3+} concentrations. The inset shows the lower concentrations and a second order polynomial fit for the determination of the intrinsic lifetime.

In order to determine the intrinsic $^4I_{13/2}$ (Er^{3+}) fluorescence lifetime for Er:$(Gd, Lu)_2O_3$, a series of measurements with varying excitation volumes[28] (pinhole method [Kue07]) was performed for the 3.1 µm thick lattice matched Er(0.6 %):$(Gd, Lu)_2O_3$ film[29] which was structurally characterized in section 6.1.3. As the measured values between 6.23 ms and 6.33 ms vary by less than 2 % and are statistically distributed instead of showing a systematic decrease for smaller excitation volumes, radiation trapping seems to have no significant effect on the measured lifetime. The significantly smaller impact of radiation trapping for this material system can be explained by the much smaller refractive index difference $\triangle n_{1.55\,\mu m} = 0.04$ (see section 7.2.1) between film and substrate in comparison to Y_2O_3 on α-Al_2O_3 ($\triangle n_{1.55\,\mu m} = 0.14$), which reduces the probability for a spontaneously emitted photon to be guided within the film and reabsorbed. Since reabsorption can be neglected, the intrinsic fluorescence lifetime was estimated to be 6.3 ms, the average of the measured values. However, the effect of lifetime reducing energy transfer processes, such as upconversion, was not taken into account. It is thus possible that the intrinsic lifetime is slightly higher. A $^4I_{13/2}$ (Er^{3+}) fluorescence lifetime of 5.6 ms was determined for the

---

[28] The different excitation volumes were realized by mounting small pinholes with diameters from 0.9 to 2.5 mm onto the sample surface.

[29] K59: $(Er_{0.006}, Gd_{0.494}, Lu_{0.500})_2O_3$ on Y_2O_3, $T = 900\,°C$, $p_{O_2} = 9 \times 10^{-3}$ mbar and $\nu_r = 5$ Hz

2 µm thick Er(0.6 %):$(Gd,Sc)_2O_3$ film[30] structurally characterized in section 6.1.3. Since the fluorescence signal was extremely weak, the pinhole method was not applied and the effect of radiation trapping was neglected. This is justified by the estimated refractive index difference $\triangle n_{1.55\,\mu m} = 0.05$ (see section 7.2.1) between film and substrate, which is much lower than the one between Y_2O_3 and α-Al_2O_3 ($\triangle n_{1.55\,\mu m} = 0.14$). An overview of the $^4I_{13/2}$ (Er^{3+}) fluorescence lifetimes for the different material systems is given in the following table.

Host Material	Sc_2O_3	Y_2O_3	$(Gd,Lu)_2O_3$	$(Gd,Sc)_2O_3$
$^4I_{13/2}$ (Er^{3+}) lifetime	5.8 ms	6.6 ms	6.3 ms	5.6 ms

Table 6.3: Fluorescence lifetimes of Er^{3+} doped sesquioxide films

It has been shown in [Kue09b] for an Er:Sc_2O_3 bulk crystal that at room temperature the non-radiative decay rate of the $^4I_{13/2}$ (Er^{3+}) manifold is negligible in comparison to the radiative one. Since Y_2O_3, Gd_2O_3 and Lu_2O_3 possess lower phonon energies than Sc_2O_3, this is most probably also true for those host materials. Therefore, the radiative lifetimes are assumed to be only slightly higher than the measured fluorescence lifetimes. In the following, the values given in Tab. 6.3 are thus used as radiative lifetimes for the determination of the emission cross-sections with the Füchtbauer Ladenburg equation.

Emission Cross-Sections

The emission cross-sections for a 1.5 µm thick Er(2 %):Sc_2O_3 film[31] and a 1 µm thick Er(0.5 %):Y_2O_3 film[32], both deposited on α-Al_2O_3 substrates, were determined from their fluorescence spectra using the Füchtbauer Ladenburg equation (5.10). Since the used photodiode was very insensitive at wavelengths above 1.6 µm, the fluorescence measurements did not cover the entire wavelength range of the $^4I_{13/2} \rightarrow {}^4I_{15/2}$ transition. Therefore, only a part of the integral in Eq. (5.10) was determined directly from the fluorescence spectra, and the approximated contribution C of this part in respect to the entire integral was taken into account. C was determined from the emission spectra given in [Pet98] for an Er:Sc_2O_3 and Er:Y_2O_3 bulk crystal and then applied to the corresponding film spectrum. The resulting film spectra in comparison to those of bulk crystals[33] are displayed in Figs. 6.22 and 6.23.

---

[30] K66: $(Er_{0.006},Gd_{0.557},Sc_{0.437})_2O_3$ on Lu_2O_3, $T = 900\,°C$, $p_{O_2} = 9 \times 10^{-3}$ mbar and $\nu_r = 1$ Hz

[31] K03: $T = 820\,°C$, $p_{O_2} = 3.1 \times 10^{-3}$ mbar and $\nu_r = 15$ Hz

[32] K16: $T = 800\,°C$, $p_{O_2} = 3.1 \times 10^{-3}$ mbar and $\nu_r = 10$ Hz

[33] The crystals were grown by the heat exchanger method with 0.3 mol.% Er_2O_3 in the melt. Since, according to [Pet98], the distribution coefficient of Er^{3+} in Y_2O_3 is 1, the Er:Y_2O_3 crystal was expected to be doped with 0.3 at.% Er^{3+}. A dopant concentration of 0.2 at.% Er^{3+} was estimated for the Er:Sc_2O_3 sample. For this, a spatially resolved EDX analysis was performed and the relative position of the prepared sample within the boule was taken into account.

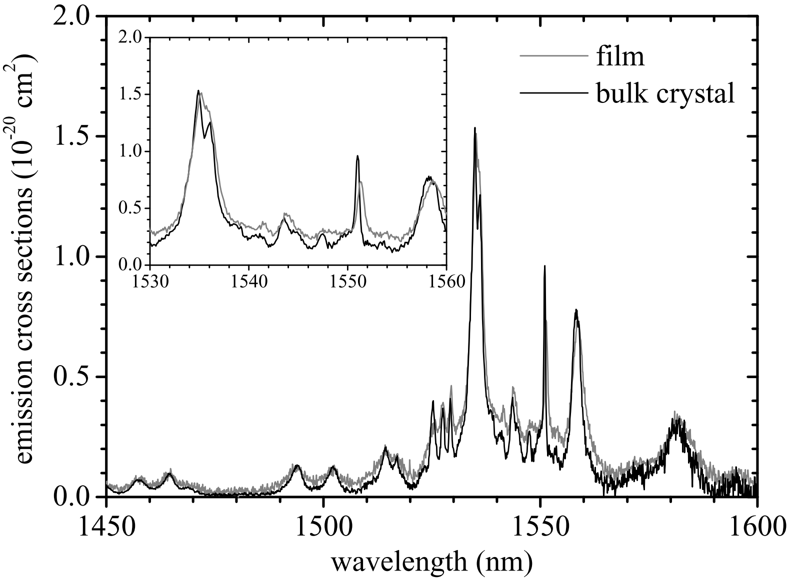

Figure 6.22: Emission spectra (0.32 nm resolution) of a 1.5 µm thick Er(2 %):Sc_2O_3 film deposited on α-Al_2O_3 and an Er(0.2 %):Sc_2O_3 bulk crystal. A detailed view of the wavelength range from 1530 nm to 1560 nm is displayed in the inset.

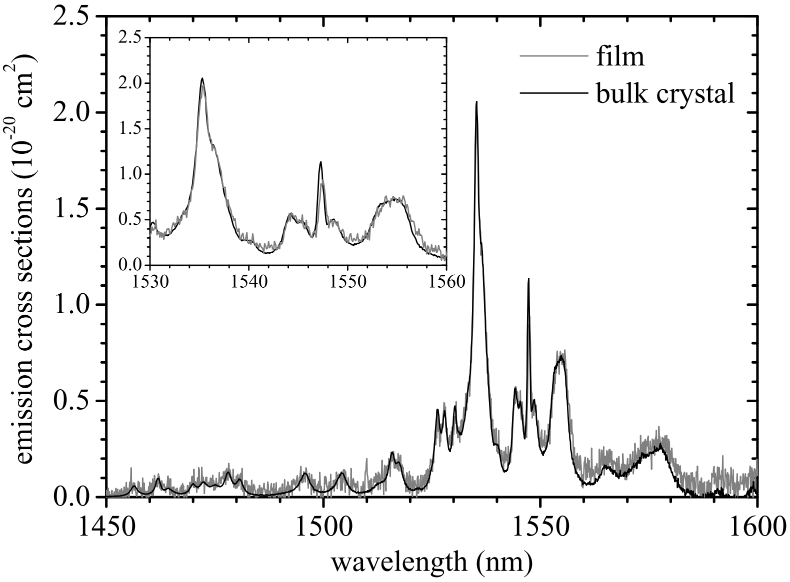

Figure 6.23: Emission spectra (0.48 nm resolution) of a 1 µm thick Er(0.5 %):Y_2O_3 film deposited on α-Al_2O_3 and an Er(0.3 %):Y_2O_3 bulk crystal. The inset shows a detailed view of the wavelength range from 1530 nm to 1560 nm.

Since reabsorption has a significant impact on fluorescence measurements of bulk crystals, the bulk emission cross-sections were determined from absorption spectra by using the McCumber relation (2.45). The required partition functions were determined from the energies given in [Pet98] for the $^4I_{15/2}$ and $^4I_{13/2}$ Stark levels of Er:Sc_2O_3 and Er:Y_2O_3.

For both material systems, peak positions and emission cross sections of the film spectra are in good agreement with those of the corresponding bulk crystal. Only a slight spectral broadening was observed for some film peaks, especially for the narrow ones at 1547 nm and 1551 nm. The broadening is probably due to variances of the local crystal field, which are caused by the existence of different crystalline regions and defects generated during the film growth. However, the results show that these effects are very small and the emission cross-sections of the polycrystalline films and monocrystalline bulk crystals are comparable. Regarding their spectroscopic properties, Er:Sc_2O_3 and Er:Y_2O_3 films deposited on α-Al_2O_3 are thus very promising for the realization of an Er^{3+} waveguide laser.

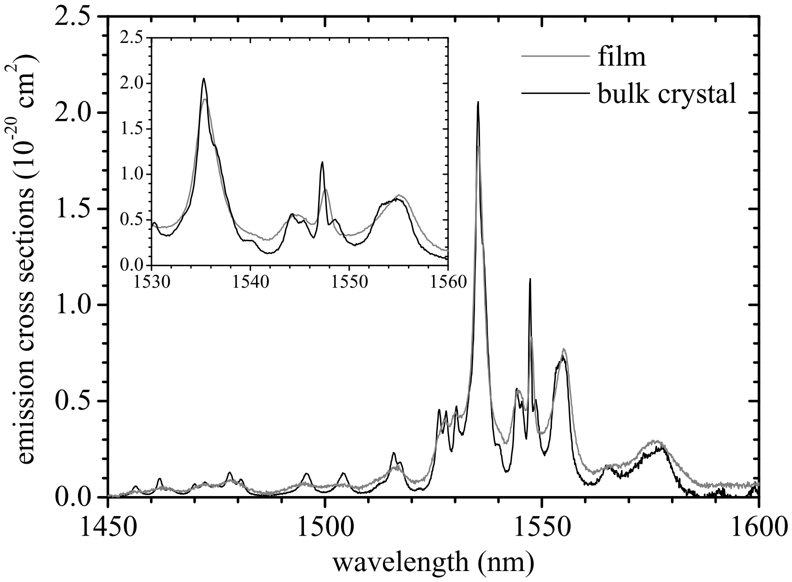

Figure 6.24: Emission spectra of a 3.1 µm thick lattice matched Er(0.6 %):(Gd, Lu)$_2$O$_3$ film (resolution 0.64 nm) and an Er(0.3 %):Y_2O_3 bulk crystal (resolution 0.48 nm). A detailed view of the wavelength range from 1530 nm to 1560 nm is shown in the inset.

The emission cross-sections of the 3.1 µm thick monocrystalline Er(0.6 %):(Gd, Lu)$_2$O$_3$ film, which was deposited on Y_2O_3, were determined in an analogous manner. Two measurements with resolutions of 0.32 nm and 0.64 nm were performed. Since the resulting spectra showed similar linewidths, a spectral bandwidth of 0.64 nm is already sufficient and the corresponding spectrum with much better signal-to-noise ratio was used. A comparison of the resulting emission cross-sections with those determined above for the Er:Y_2O_3 bulk crystal is displayed in Fig. 6.24. For the calculations, the contribution C

of the measured wavelength range to the integral in Eq. (5.10) was assumed to be equal to the one determined for Er:Y_2O_3. This is justified by the shape of the Er:$(Gd, Lu)_2O_3$ fluorescence spectrum, which is in good agreement with that of Er:Y_2O_3.

The peak positions in the Er:$(Gd, Lu)_2O_3$ film spectrum are nearly the same as those measured for the Er:Y_2O_3 bulk crystal. This can be explained by the epitaxial growth and nearly perfect lattice matching. However, a spectral broadening of the emission peaks in the film, resulting in lower peak cross-sections, can be observed. This is probably due to the statistical occupation of the cation sites by Gd^{3+} and Lu^{3+}.

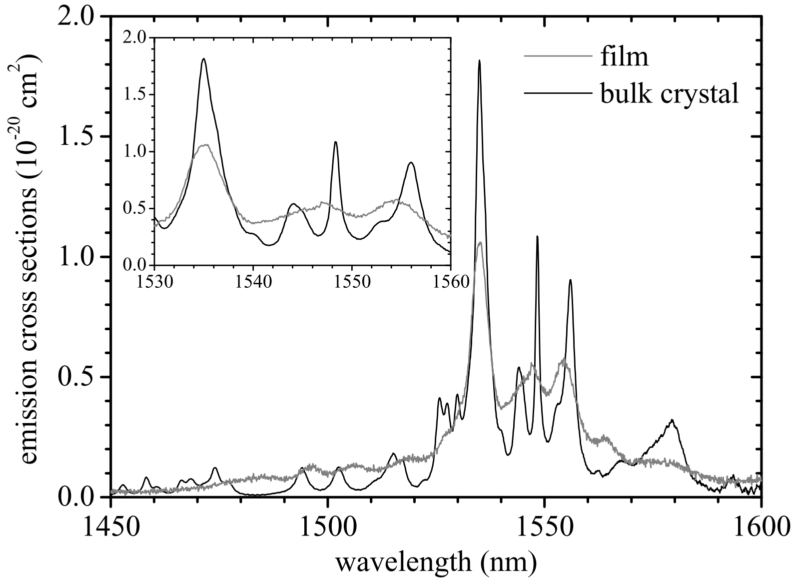

Figure 6.25: Emission spectra (0.64 nm resolution) of a 2 µm thick lattice matched Er(0.6 %):$(Gd, Sc)_2O_3$ film and an Er(0.3 %):Lu_2O_3 bulk crystal. The inset shows a detailed view of the wavelength range from 1530 nm to 1560 nm.

A much stronger line broadening and significantly lower peak cross sections were observed for the 2 µm thick Er(0.6 %):$(Gd, Sc)_2O_3$ film, which was deposited on a Lu_2O_3 substrate. For the determination of the emissions cross-sections with Eq. (5.10), the contribution C of the measured wavelength range to the entire integral was assumed to be comparable to that of Er:Lu_2O_3 and was thus determined from the corresponding bulk spectrum given in [Pet98]. Figure 6.25 compares the spectrum of the Er(0.6 %):$(Gd, Sc)_2O_3$ film with the one of an Er(0.3 %):Lu_2O_3 bulk crystal[34]. The stronger spectral broadening of the Er:$(Gd, Sc)_2O_3$ film in comparison to the Er:$(Gd, Lu)_2O_3$ one can be explained by considering the ionic radii of their components. Since the sizes of Sc^{3+} and Gd^{3+} differ

---

[34] The crystal was grown by the heat exchanger method with 0.3 mol.% Er_2O_3 in the melt. Due to the distribution coefficient of 1 for Er^{3+} in Lu_2O_3 [Pet98], the crystal was expected to be doped with 0.3 at.% Er^{3+}. The emission cross sections were determined from the absorption spectrum using the McCumber relation (2.45) and the Stark-level energies given in [Pet98].

more than the ones of Lu^{3+} and Gd^{3+}, the variations of the local crystal field due to the statistical cation distribution are stronger in $Er{:}(Gd,Sc)_2O_3$. While the resulting broader emission bands of $Er{:}(Gd,Sc)_2O_3$ might be beneficial for optical amplifiers, $Er{:}(Gd,Lu)_2O_3$ was chosen for first Er^{3+} laser experiments, because of the higher peak cross-sections.

Spectroscopy at Cryogenic Temperatures

For the theoretical gain calculations in section 7.5.1 the absorption cross-sections of the films are required. However, due to the small film thicknesses, transmission measurements as described in section 5.4.2 were not successful. The absorption cross-sections of the lattice matched $Er{:}(Gd,Lu)_2O_3$ film were thus determined from its emission cross-sections by use of the McCumber relation (2.45). For the calculations of the required partition functions, the Stark-level energies of the $^4I_{15/2}$ and $^4I_{13/2}$ manifold of Er^{3+} in $(Gd,Lu)_2O_3$ have to be determined, which is possible by emission and absorption spectroscopy at cryogenic temperatures. However, even at low temperatures, film transmission measurements were not successful. Therefore, only fluorescence spectra were obtained. For cooling the film, it was placed inside a cryostat. Apart from that, the experimental procedure was similar to the one performed at room temperature. Figure 6.26 shows the resulting fluorescence spectra measured at two different temperatures[35]. For comparison, the energies for transitions between Stark levels of the $^4I_{13/2}$ and $^4I_{15/2}$ manifold of $Er{:}Y_2O_3$ and $Er{:}Lu_2O_3$, which were determined from the Stark-level energies given in [Pet98], are displayed as well.

Most fluorescence peaks in the spectrum can be related to one of those transitions. In most cases, the $Er{:}(Gd,Lu)_2O_3$ peak positions correspond to energies between the ones determined for $Er{:}Y_2O_3$ and $Er{:}Lu_2O_3$. The Stark-level energies of the $Er{:}(Gd,Lu)_2O_3$ film are thus assumed to be somewhere in between those of $Er{:}Y_2O_3$ and $Er{:}Lu_2O_3$. The McCumber relation (2.45) incorporates these energies only as ratio of partition functions $Z_\mathrm{l}/Z_\mathrm{u}$. Considering the $^4I_{13/2}$ and $^4I_{15/2}$ manifolds, $Z_\mathrm{l}/Z_\mathrm{u}$ varies by less than 2 % when comparing $Er{:}Lu_2O_3$ with $Er{:}Y_2O_3$. The energy levels of $Er{:}Y_2O_3$ given in [Pet98] were thus used for the calculation of the $Er{:}(Gd,Lu)_2O_3$ absorption cross-sections instead of the not completely measured $Er{:}(Gd,Lu)_2O_3$ level structure. Figure 6.27 shows the calculated room temperature absorption spectrum of the $Er{:}(Gd,Lu)_2O_3$ film in comparison to the one determined by transmission measurements of the $Er(0.3\,\%){:}Y_2O_3$ bulk crystal mentioned above.

---

[35] The temperatures T given in Fig. 6.26 are the measured temperatures. Due to the local heating caused by the excitation light, the actual temperatures at the emitting spot are expected to be higher. However, relatively low excitation intensities were used for the measurements in order to reduce the heating effect.

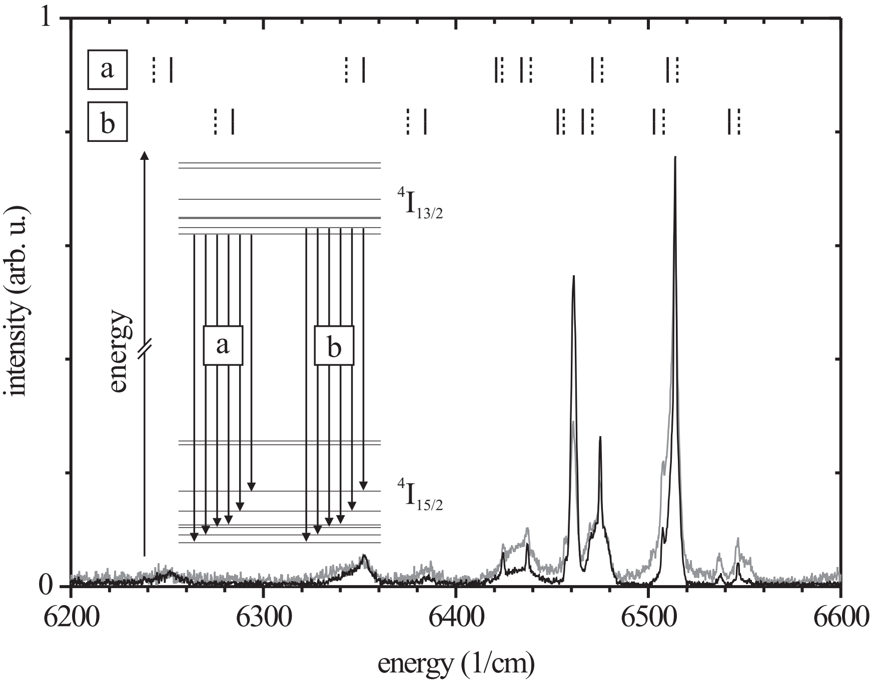

Figure 6.26: Low temperature emission spectra (0.32 nm resolution) of a 3.1 µm thick lattice matched Er(0.6 %):$(Gd, Lu)_2O_3$ film deposited on an Y_2O_3 substrate. The black spectrum was measured at a film temperature $T = 10$ K and the grey one at $T = 70$ K. Two rows of vertical lines indicate energies of transitions [a] and [b] originating from the lowest and second lowest Stark level of the $^4I_{13/2}$ (Er^{3+}) manifold, respectively. These energies were determined from the Stark-level energies given in [Pet98] for Er:Y_2O_3 (solid lines) and Er:Lu_2O_3 (dashed lines).

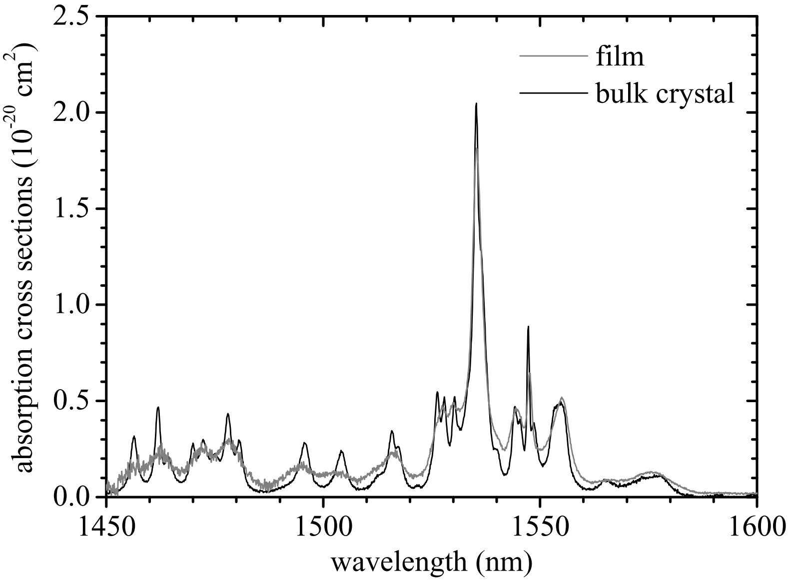

Figure 6.27: Absorption spectra of a 3.1 µm thick lattice matched Er(0.6 %):(Gd, Lu)$_2$O$_3$ film (resolution 0.64 nm) and an Er(0.3 %):Y$_2$O$_3$ bulk crystal (resolution 0.48 nm)

6.2.2 Nd^{3+} Doped Films

The spectroscopic properties of the 1 µm thick lattice matched Nd(0.5 %):(Gd, Lu)$_2$O$_3$ film[36] described in section 6.1.3 were investigated as well. Fluorescence lifetimes of the ^{4}F$_{3/2}$ (Nd^{3+}) manifold ranging from 226 to 236 µs were determined from fluorescence decay curves[37] of ^{4}F$_{3/2}$ → ^{4}I$_{11/2}$ transitions upon pulsed excitation at 820 nm with different excitation volumes[38]. The measured values vary by less than 5 % and no significant decrease for smaller excitation volumes was observed. As for the Er^{3+} doped (Gd, Lu)$_2$O$_3$ film, the effect of radiation trapping on the lifetime measurement is thus negligible. By averaging the measured values, a fluorescence lifetime of 230 µs was determined for the Nd(0.5 %):(Gd, Lu)$_2$O$_3$ film. It is slightly shorter than the corresponding lifetimes of 275 µs and 238 µs measured in [For99] from the fluorescence decay curves of a Nd(0.3 %):Y$_2$O$_3$ and a Nd(1.1 %):Y$_2$O$_3$ bulk crystal, respectively. Considering that these lifetimes are measured for a bulk crystal and thus most likely increased by radiation trapping, they are comparable to those measured for the Nd:(Gd, Lu)$_2$O$_3$ film. Hence, the radiative lifetime of 410 µs, which was derived in [For99] from the spectroscopic data of the above mentioned Nd:Y$_2$O$_3$ bulk crystals, was assumed to be valid for the lattice matched film as well.

---

[36] K47: $(\mathrm{Nd}_{0.005}, \mathrm{Gd}_{0.479}, \mathrm{Lu}_{0.516})_2\mathrm{O}_3$ on Y$_2$O$_3$, $T = 900\,°\mathrm{C}$, $p_{\mathrm{O}_2} = 8.8 \times 10^{-3}$ mbar and $\nu_\mathrm{r} = 1$ Hz

[37] Since the fluorescence decay is almost single exponential, according fit functions were used for the lifetime determination.

[38] For this, pinholes with diameters from 1.5 to 2.5 mm were mounted onto the sample surface.

The emission cross-sections of the $^4F_{3/2} \rightarrow {}^4I_{11/2}$ transitions were determined from the fluorescence spectrum of the Nd:$(Gd, Lu)_2O_3$ film by use of the Füchtbauer Ladenburg equation (5.10). Therein, a branching ratio η of 47 % was assumed, as determined for Nd:Y_2O_3 in [For99]. Figure 6.28 shows the emission cross-section spectrum in comparison to the one measured in [For99] for the Nd(1.1 %):Y_2O_3 bulk crystal mentioned above. A spectral bandwidth of 0.48 nm was sufficient for the film measurement, as both a 0.32 nm and 0.48 nm resolution spectrum exhibited the same linewidths. However, due to the longer integration time, the 0.32 nm resolution spectrum possessed a better signal-to-noise ratio and is thus displayed in the figure.

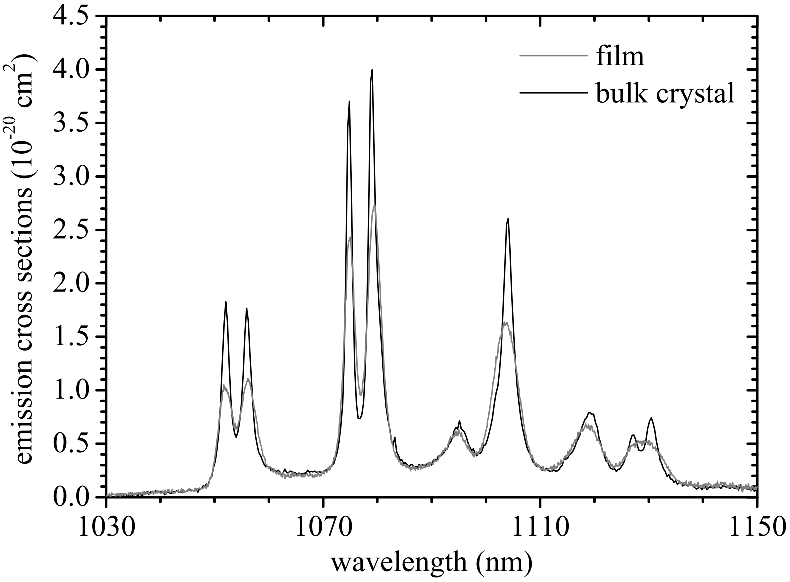

Figure 6.28: Emission spectrum of a 1 µm thick lattice matched Nd(0.5 %):$(Gd, Lu)_2O_3$ film in comparison to the one given in [For99] for a Nd(1.1 %):Y_2O_3 bulk crystal

As for the Er^{3+} doped $(Gd, Lu)_2O_3$ film, the peak positions of the Nd^{3+} doped lattice matched $(Gd, Lu)_2O_3$ film are similar to those of the correspondingly doped Y_2O_3 bulk crystal. A spectral line broadening and reduced peak cross-sections are observed as well. Although the highest emission cross-section of the Nd:$(Gd, Lu)_2O_3$ film is with $2.7 \times 10^{-20}\,cm^2$ significantly smaller than the value of $30 \times 10^{-20}\,cm^2$ [For99] reported for Nd:YAG, it is the highest one measured for all investigated films. Furthermore, Nd^{3+} allows for the realization of four-level lasers. Lattice matched Nd:$(Gd, Lu)_2O_3$ on Y_2O_3 is thus a very promising material system for a first sesquioxide waveguide laser.

7 Waveguide Experiments

This chapter describes the waveguide preparation as well as the experiments performed with planar and channel waveguides. Several waveguide properties such as mode intensity distributions, propagation losses and optical gain were determined. An overview of the investigated waveguides and their properties is given in Tab. 7.6. According to the considerations in section 7.5.2, doping concentrations of 0.5 % and 0.6 % were chosen for the $\mathrm{Nd{:}(Gd,Lu)_2O_3}$ and $\mathrm{Er{:}(Gd,Lu)_2O_3}$ waveguides, respectively. The Er^{3+} concentration of the Y_2O_3 waveguide was higher, since this waveguide was prepared for the spectroscopic investigations in section 6.2.1.

7.1 Waveguide Preparation

In order to fabricate rib-channel waveguides allowing for a two-dimensional light confinement, some planar waveguides were structured at the University of Twente. First, an amorphous Al_2O_3 (a-Al_2O_3) mask was created. For this, a-Al_2O_3 was sputtered onto the film surface, covered with a photoresist mask layer patterned by standard lithography, and then structured by reactive ion etching[1] (RIE) using a BCl_3/HBr process gas. The mask was designed to leave approximately half of the film surface unstructured, so both channel and planar waveguide experiments could be performed with the same sample.[2] After mask fabrication, the sesquioxide film was physically etched by use of an Ar-ion plasma, resulting in waveguide channels such as those displayed in Fig. 7.1. A detailed description of the etch process is given in [Bra07].

Coupling of light into and out of the waveguide took place via the waveguide end-facets, which had thus to be polished. The sample was glued[5] to another substrate of similar hardness or another waveguide, in such a way that the film was sandwiched between two substrates. Due to this procedure, the film edges were protected against damage and the rounding of the end facets during the polishing process was reduced. Some of the films were further protected by an amorphous Al_2O_3 or SiO_2 top cladding, which was sputtered onto them prior to polishing.[6] As pointed out in [Eas07] and shown in

---

[1] An Oxford Plasmalab 100 inductively coupled plasma reactive ion etching system was used.

[2] Approximately 50 channels were structured into each film. However, some of them were damaged, thus resulting in a smaller number of uninterrupted channels.

[3] The pictures were taken at the University of Twente.

[4] K23: $\mathrm{Er(2\%){:}Y_2O_3}$ on α-Al_2O_3 (0001), $T = 800\,^\circ\mathrm{C}$, $p_{O_2} = 3 \times 10^{-3}$ mbar and $\nu_\mathrm{r} = 10\,\mathrm{Hz}$

[5] Struers TriPod Wax (melting point 75 °C) proved to be suitable for this purpose.

[6] Sputtering of the Al_2O_3 and SiO_2 top claddings was performed at the University of Twente and Ecole Polytechnique Fédérale de Lausanne, respectively.

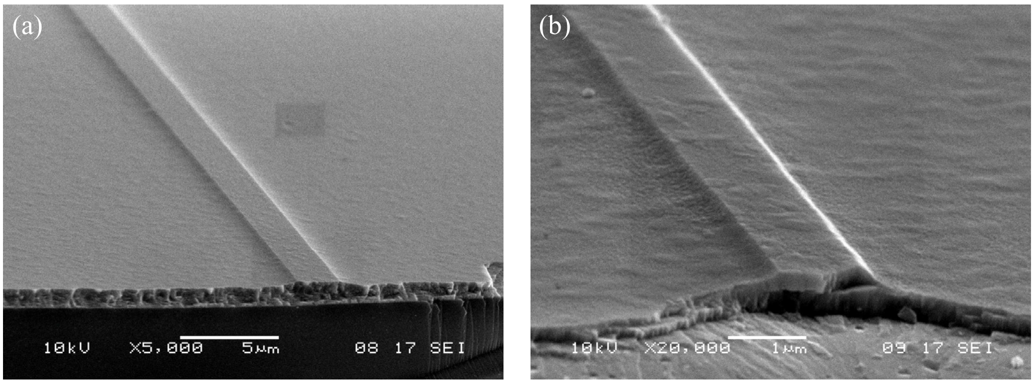

Figure 7.1: SEM images[3] of waveguide channels resulting from 270 nm deep etching of a 1 µm thick Er:Y_2O_3 film[4]. The magnification is (a) 5000× and (b) 20000×, respectively.

section 7.4.1, such a top cladding can also result in a decrease of the scattering losses by burying particulates which are sticking out of the surface. The polishing process for the sesquioxide-on-sesquioxide waveguides was optimized in cooperation with the Ecole Polytechnique Fédérale de Lausanne.[7] Since α-Al_2O_3 possesses a much higher degree of hardness than Sc_2O_3 and Y_2O_3, the polishing process proved to be very difficult for the sesquioxide-on-sapphire waveguides and resulted in an extremely poor surface quality of their end facets. Even various companies which are specialized on polishing did not achieve a sufficiently high end-facet quality. Hence, most of the waveguide experiments were performed with monocrystalline $(Gd, Lu)_2O_3$ films deposited on Y_2O_3, although their peak emission cross-sections were slightly lower than those of the Y_2O_3 films deposited on α-Al_2O_3. However, the polishing process for sesquioxide-on-sapphire waveguides has recently been improved[8], thus allowing to compare their properties with the ones of sesquioxide-on-sesquioxide systems in the near future.

7.2 Basic Waveguide Properties

7.2.1 Refractive Indexes

The refractive indexes of the monocrystalline $(Gd, Lu)_2O_3$ films and amorphous top claddings were calculated using the dispersion relations given in Tab. 7.1. In order to determine the dispersion relation for the lattice matched $(Gd, Lu)_2O_3$ films, a refractive index measurement of a 5 µm thick Er(0.6%):$(Gd, Lu)_2O_3$ film[9] was performed at the University of Twente. The refractive indexes n at the wavelengths $\lambda = 1300\,\mathrm{nm}$ and

---

[7] A Logitech CL40/CL50 polishing machine was used. First, the samples were lapped or grinded with SiC. After that, several polishing steps using α-Al_2O_3 suspensions with grain sizes of 5 µm, 1 µm and 0.3 µm on different woven polishing cloths (polyester, acetat and natural silk) were carried out.

[8] A chemo-mechanical polishing step (Logitech SF1 polishing suspension) proved to be beneficial.

[9] K63: $(Er_{0.006}, Gd_{0.494}, Lu_{0.500})_2O_3$ on Y_2O_3 {100}, $T = 900\,^\circ\mathrm{C}$, $p_{O_2} = 9 \times 10^{-3}\,\mathrm{mbar}$ and $\nu_r = 5\,\mathrm{Hz}$

$\lambda = 1550\,\text{nm}$ were obtained by prism coupling measurements using the attenuated total reflection (ATR) method [Ulr73, Hoe94], and the Cauchy parameters A and B were determined by fitting with the Cauchy formula:

$$n(\lambda) = A + \frac{B}{\lambda^2} \tag{7.1}$$

Since all investigated Er:$(\mathrm{Gd,Lu})_2\mathrm{O}_3$ and Nd:$(\mathrm{Gd,Lu})_2\mathrm{O}_3$ films possessed a very small doping concentration and their $\mathrm{Gd_2O_3}$ and $\mathrm{Lu_2O_3}$ contents were quite similar, the obtained dispersion relation was assumed to be valid for all those films. The refractive index of a sputtered a-$\mathrm{Al_2O_3}$ top claddings was measured for various wavelengths between 600 nm and 1100 nm using spectroscopic ellipsometry[10], and the Cauchy parameters were determined by fitting with Eq. (7.1). However, the refractive index of the $\mathrm{SiO_2}$ cover layer, which had been sputtered onto the investigated $\mathrm{Y_2O_3}$ film, was not measured. Thus, the refractive index of that layer was calculated using the Sellmeier equation given in [Jer05] for $\mathrm{SiO_2}$. For this, a film density $\rho = 2.2\,\mathrm{g/cm^3}$ similar to that of fused quartz was assumed.

Material	$n(\lambda$ in µm$)$	$n(\lambda=0.80)$	$n(\lambda=1.08)$	$n(\lambda=1.55)$
$(\mathrm{Gd,Lu})_2\mathrm{O}_3$ films	$1.912 + 0.0228\,\lambda^{-2}$	1.948	1.932	1.921
a-$\mathrm{Al_2O_3}$ cover layer	$1.642 + 0.0085\,\lambda^{-2}$	1.655	1.649	1.646
$\mathrm{SiO_2}$ $(\rho=2.2\,\mathrm{g/cm^3})$	$\sqrt{1+\frac{1.176}{1-0.015\,\lambda^{-2}}}$	1.485	1.480	1.478

Table 7.1: Dispersion relations for the investigated $(\mathrm{Gd,Lu})_2\mathrm{O}_3$ films and amorphous cover layers, as well as calculated refractive indexes at various wavelengths λ (in µm). The refractive indexes of the a-$\mathrm{Al_2O_3}$ top cladding was determined for TE polarized light.

The refractive indexes given in Tab. 7.1 for the $(\mathrm{Gd,Lu})_2\mathrm{O}_3$ films are in quite good accordance to those obtained by multiplying the indexes of $\mathrm{Gd_2O_3}$ and $\mathrm{Lu_2O_3}$ with their relative contributions to the solid solution (approximately 50 % each) and adding the results. Hence, the refractive index of the $(\mathrm{Gd,Sc})_2\mathrm{O}_3$ film spectroscopically investigated in section 6.2 could be estimated from the refractive indexes of $\mathrm{Gd_2O_3}$ and $\mathrm{Sc_2O_3}$ given in Tab. 3.1. Neglecting the contribution of the dopant ions and thus assuming $\mathrm{Gd_2O_3}$ and $\mathrm{Sc_2O_3}$ contents of 56 % and 44 %, respectively, the refractive index of this film was calculated to be approximately 1.95 at $\lambda = 1.55\,\mu\mathrm{m}$.

7.2.2 NA and Related Properties

By using Eq. (2.3) and the refractive indexes calculated with the dispersion relations given in the tables 3.1 and 7.1, the numerical apertures (NA) and critical coupling angles θ_{crit}

---

[10] The measurement was performed at the University of Twente.

of the investigated waveguiding films were calculated for two promising Nd^{3+} and Er^{3+} pump wavelengths λ_p. The results are shown in Tab. 7.2.

	NA		θ_{crit} (rad)		$2\,\omega_0$ (µm)	
Material System	820 nm	1480 nm	820 nm	1480 nm	820 nm	1480 nm
Y_2O_3 on α-Al_2O_3	0.71	0.70	0.79	0.77	0.66	1.22
$(Gd, Lu)_2O_3$ on Y_2O_3	0.43	0.40	0.45	0.41	1.16	2.31

Table 7.2: Numerical apertures (NA) and critical coupling angles θ_{crit} for the promising pump wavelengths $\lambda_p = 820$ nm and $\lambda_p = 1480$ nm as well as the minimum beam diameters $2\,\omega_0$ of focussed pump beams with maximum far-field divergence angles equal to θ_{crit}

In order to roughly estimate the minimum film thickness for efficient coupling of pump light into the different waveguiding films, a focussed diffraction-limited ($M^2 = 1$) pump beam with a maximum far-field divergence angle θ_{max} equal to θ_{crit} was considered. Its beam width[11] ω_0 at the beam waist was calculated by use of the beam parameter product [Sie86]:

$$\theta_{max} = \frac{M^2 \lambda_p}{\pi \omega_0} \tag{7.2}$$

The minimum thickness of the waveguiding film for efficient coupling of the pump light was estimated to be equal to the minimum beam diameter $2\,\omega_0$. Minimum $(Gd, Lu)_2O_3$ film thicknesses of 1.2 µm and 2.3 µm were calculated for the pump wavelengths of 820 nm (Nd^{3+}) and 1480 nm (Er^{3+}), respectively. While this requirement is fulfilled for the 1.9 µm thick Nd:$(Gd, Lu)_2O_3$ and 3.1 µm thick Er:$(Gd, Lu)_2O_3$ film, coupling of pump light into the 1.0 µm thick Er:$(Gd, Lu)_2O_3$ film is expected to be quite inefficient.

7.3 Waveguide Modes

7.3.1 Planar Waveguide Modes

Both TE and TM modes can be guided in a planar waveguide. According to [Yar76], a TM mode usually possesses a lesser degree of confinement compared to a TE mode of the same order. However, since the general features of TE and TM modes are similar, the following calculations were performed for TE modes only. The maximum number of guided TE modes in the investigated planar waveguides was calculated using Eq. (2.23). For this, the x-components $k_{x,m}$ of the wave vectors in the different layers m were substituted by Eq. (2.21) and the thickness d_3 of the waveguiding film was plotted as a function of the effective refractive index n_{eff}. The four lowest order modes TE_p (with mode numbers $p = 0, 1, 2, 3$) were considered.

---

[11] radius according to the $1/e^2$ definition

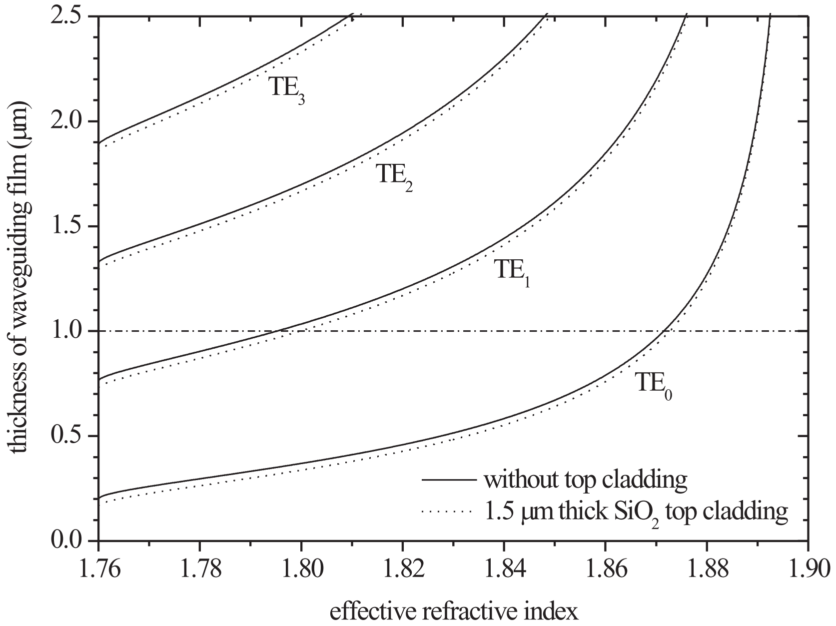

Figure 7.2: Simulation of the TE_p modes with mode numbers $p = 0, 1, 2, 3$ in a planar Y_2O_3-on-sapphire waveguide. The calculations were performed for a wavelength of 800 nm. The horizontal line indicates the thickness of the investigated waveguiding film.

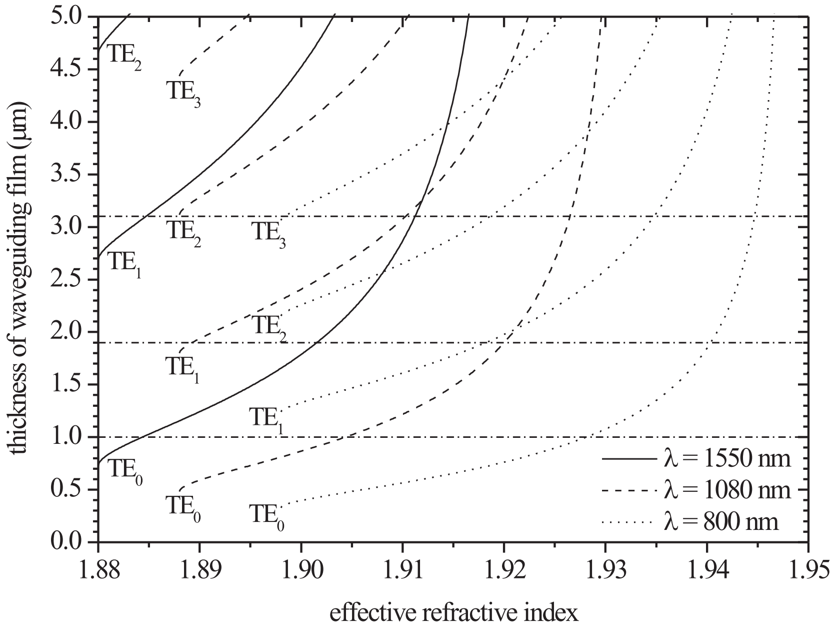

Figure 7.3: Simulation of the TE_p modes with mode numbers $p = 0, 1, 2, 3$ in a planar $(Gd, Lu)_2O_3$-on-Y_2O_3 waveguide covered with a 1.5 µm thick a-Al_2O_3 top cladding. Several wavelengths λ were considered. The horizontal lines indicate the thicknesses of the investigated waveguiding films.

Figure 7.2 shows the resulting functions for the investigated Y_2O_3-on-sapphire waveguide (see Tab. 7.6), both prior and after deposition of the amorphous SiO_2 top cladding. The calculations were performed for a wavelength $\lambda = 800\,\mathrm{nm}$, which was later used for the determination of the planar waveguide losses. The functions displayed in Fig. 7.2 allow to determine the maximum number of guided modes for a given film thickness and the effective refractive indexes of these modes. The thickness $d_3 = 1\,\mu\mathrm{m}$ of the investigated film is represented by a horizontal line. Its intersections with the curves representing the TE_0 and TE_1 mode indicate that these two modes can be guided, in both cases with or without top cladding.

The calculations for the planar parts of the $(Gd, Lu)_2O_3$-on-Y_2O_3 waveguides were performed in a similar way. Since laser emission at about 1080 nm and 1550 nm was expected for Nd:$(Gd, Lu)_2O_3$ and Er:$(Gd, Lu)_2O_3$, respectively, and the loss measurements of the planar waveguides were performed at about 800 nm, these wavelengths were considered. The results are displayed in Fig. 7.3. For the calculations, an a-Al_2O_3 top-cladding thickness $d_2 = 1.5\,\mu\mathrm{m}$ was used. Since small variations of d_2 around this value did not show any significant impact on the effective refractive indexes of the guided modes, the simulations in Fig. 7.3 are valid for all three investigated $(Gd, Lu)_2O_3$-on-Y_2O_3 waveguides. A minimum film thickness of about 0.75 µm is required for waveguiding at $\lambda = 1550\,\mathrm{nm}$. This requirement is fulfilled for all investigated Er:$(Gd, Lu)_2O_3$ waveguides. While solely the fundamental TE mode can be guided in the 1.0 µm thick Er:$(Gd, Lu)_2O_3$ film, the 1.9 µm thick Nd:$(Gd, Lu)_2O_3$ film and the 3.1 µm thick Er:$(Gd, Lu)_2O_3$ film support guiding of both the TE_0 and the TE_1 mode at the expected laser wavelengths.

7.3.2 Rib-Channel Waveguide Modes

In this section, light confinement in the $(Gd, Lu)_2O_3$ rib-channel waveguides is discussed. While the planar parts of the 1.9 µm thick Nd:$(Gd, Lu)_2O_3$ film and the 3.1 µm thick Er:$(Gd, Lu)_2O_3$ film support up to two TE modes at the expected laser wavelengths, the etch depths and channel dimensions were chosen in such a way that solely the fundamental TE and TM modes can be guided in the resulting rib-channel waveguides.

Figure 7.4 shows the simulated transverse intensity profiles of the fundamental TE modes in the 1.0 µm and 3.1 µm thick Er:$(Gd, Lu)_2O_3$ waveguide for an assumed channel width of 5 µm and the potential laser wavelength of 1535 nm. The simulations were performed with the software *FieldDesigner* developed by *PhoeniX BV*. Since the channel widths vary from 2 to 5 µm, different widths were considered and the resulting modes were compared.

For the realization of waveguide amplifiers and lasers it is important that a high percentage of the guided light propagates in the active regions where amplification is possible. Hence, the ratio $\Gamma := P_{\mathrm{doped}}/P_{\mathrm{total}}$ of the light power within the doped $(Gd, Lu)_2O_3$ film and the total power of the propagating light was calculated for the fundamental TE and TM modes, all three structured waveguides and several channel widths.

$$\Gamma = \frac{\int\int_{\mathrm{mode}} D(x,y)\, I(x,y)\, dx\, dy}{\int\int_{\mathrm{mode}} I(x,y)\, dx\, dy} \tag{7.3}$$

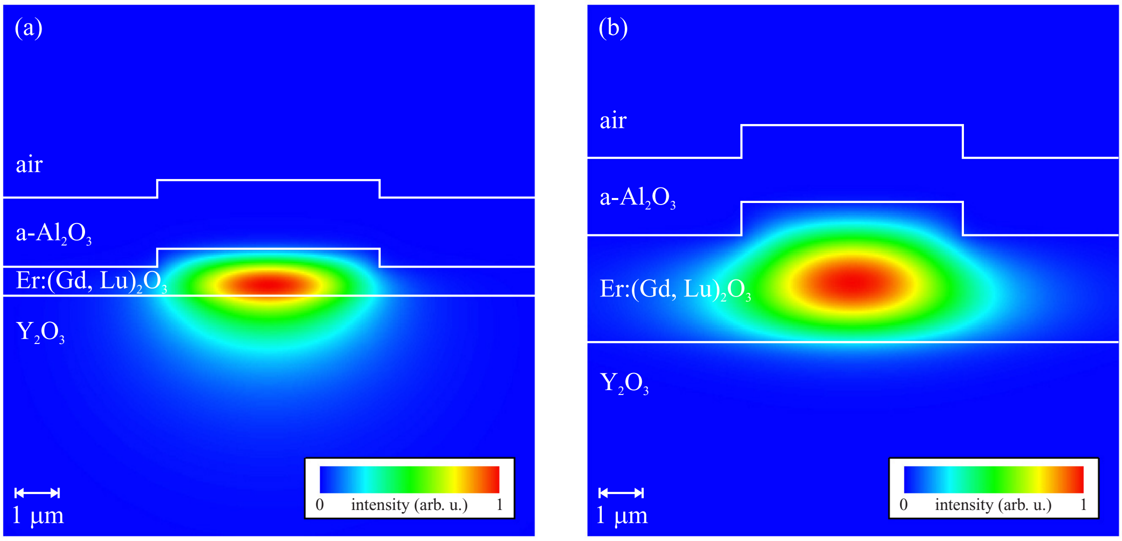

Figure 7.4: Simulated intensity profiles of the fundamental TE modes of 5 µm wide Er:(Gd, Lu)$_2$O$_3$ rib-channel waveguides. The simulations were performed for both the (a) 1.0 µm thick and (b) 3.1 µm thick film using the potential laser wavelength $\lambda = 1535$ nm.

Γ was calculated with Eq. (7.3) by integrating numerically over the simulated transverse intensity profile $I(x, y)$. $D(x, y)$ is a function describing the dopant distribution; it is 1 for all values $\{x, y\}$ within the waveguiding film and 0 otherwise. The resulting confinement factors Γ are summarized in Tab. 7.3.

		Channel width			
Waveguiding film	Mode	2 µm	3 µm	4 µm	5 µm
1.0 µm Er:(Gd, Lu)$_2$O$_3$	TE	-	25.2 %	34.6 %	39.3 %
	TM	-	-	15.8 %	25.9 %
3.1 µm Er:(Gd, Lu)$_2$O$_3$	TE	92.8 %	93.7 %	94.3 %	94.8 %
	TM	-	93.4 %	94.1 %	94.6 %
1.9 µm Nd:(Gd, Lu)$_2$O$_3$	TE	92.6 %	93.2 %	93.6 %	93.9 %
	TM	92.2 %	93.0 %	93.4 %	93.6 %

Table 7.3: Simulated confinement Γ of the fundamental modes guided in the investigated rib-channel waveguides. The simulations were performed at $\lambda = 1535$ nm and $\lambda = 1080$ nm for the Er:(Gd, Lu)$_2$O$_3$ and Nd:(Gd, Lu)$_2$O$_3$ waveguides, respectively. Missing values indicate that the corresponding mode is not guided or the confinement is extremely weak.

For the 3.1 µm and 1.9 µm thick rib-channel waveguides, more than 90 % of the guided light is propagating in the doped regions. The TM modes are slightly less confined to the (Gd, Lu)$_2$O$_3$ film than the corresponding TE modes. While the confinement is decreasing with the channel width, the effect is quite small for these waveguides until the channel width falls below a critical value; a channel width of 2 µm is not sufficient to support guiding of a two-dimensionally confined TM mode in the 3.1 µm thick waveguide. Light confinement in the 1.0 µm thick film is much lower and much more dependent on the channel width. The simulations were also performed using slightly varied parameters with respect to the measured ones. While small deviations of the film thickness and refractive index from the measured values have a marginal influence on the light confinement of the 3.1 µm and 1.9 µm thick rib-channel waveguides, they have a significant impact on the confinement factors of the 1.0 µm thick film. The confinement factors estimated for the 1.0 µm thick $\mathrm{Er{:}(Gd, Lu)_2O_3}$ waveguide are thus expected to be very inaccurate. However, the light confinement in the 1.0 µm thick film is in any case significantly lower than that in the 3.1 µm thick one. Therefore, a lower gain is expected for the former.

As pointed out in section 2.1.2, a good overlap

$$\Omega = \frac{\left|\int\int_{-\infty}^{-\infty} \Psi_\mathrm{p}(x,\, y)\, \Psi_\mathrm{l}^*(x,\, y)\, dx\, dy\right|^2}{\int\int_{-\infty}^{-\infty} |\Psi_\mathrm{p}(x,\, y)|^2\, dx\, dy \cdot \int\int_{-\infty}^{-\infty} |\Psi_\mathrm{l}(x,\, y)|^2\, dx\, dy} \tag{7.4}$$

between the electric fields $\Psi_\mathrm{p}(x, y)$ and $\Psi_\mathrm{l}(x, y)$ of the pump and laser mode can be obtained in channel waveguides. By use of the software *FieldDesigner*, the TE mode profiles at wavelengths of 1480 nm and 1535 nm were simulated for a 5 µm wide channel of the 3.1 µm thick $\mathrm{Er{:}(Gd, Lu)_2O_3}$ waveguide and an overlap of 99.98 % has been calculated.

Rib-channel waveguiding has been demonstrated for all three $\mathrm{(Gd, Lu)_2O_3}$ waveguides. The experimental setup used for the $\mathrm{Er{:}(Gd, Lu)_2O_3}$ waveguides is illustrated in Fig. 7.5. A fiber-coupled laser diode[12] emitting at $\lambda = 1480$ nm served as light source. The light was collimated and then coupled into a waveguide channel using a microscope objective with a NA of 0.35. The outcoupled light was collected with another objective possessing a NA of 0.7 and imaged onto the active area of a camera[13]. After the measurement, the waveguide was removed and a microscope slide with a micrometer scale was placed at the former position of the outcoupling end-facet. By imaging this scale onto the active area of the camera, the mode dimensions were obtained.

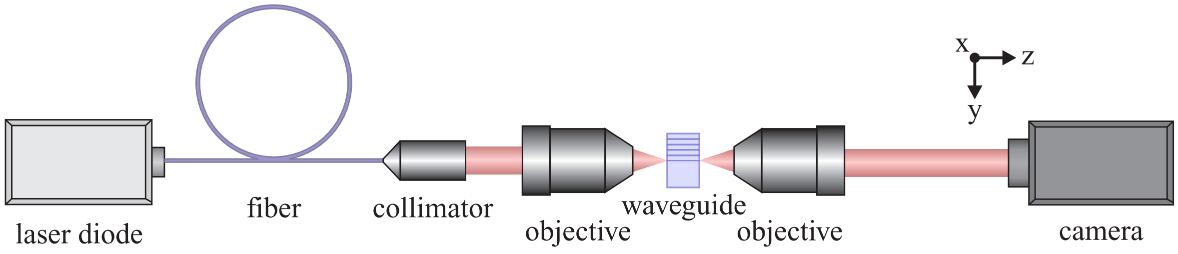

Figure 7.5: Experimental setup for the determination of the transverse intensity profiles of guided modes in the $\mathrm{Er{:}(Gd, Lu)_2O_3}$ rib-channel waveguides

---

[12] A laser diode of the 3400 Series from JDS Uniphase pigtailed to a polarization maintaining single mode Fujikura Panda fiber was used.

[13] Polytec Microviewer 7290

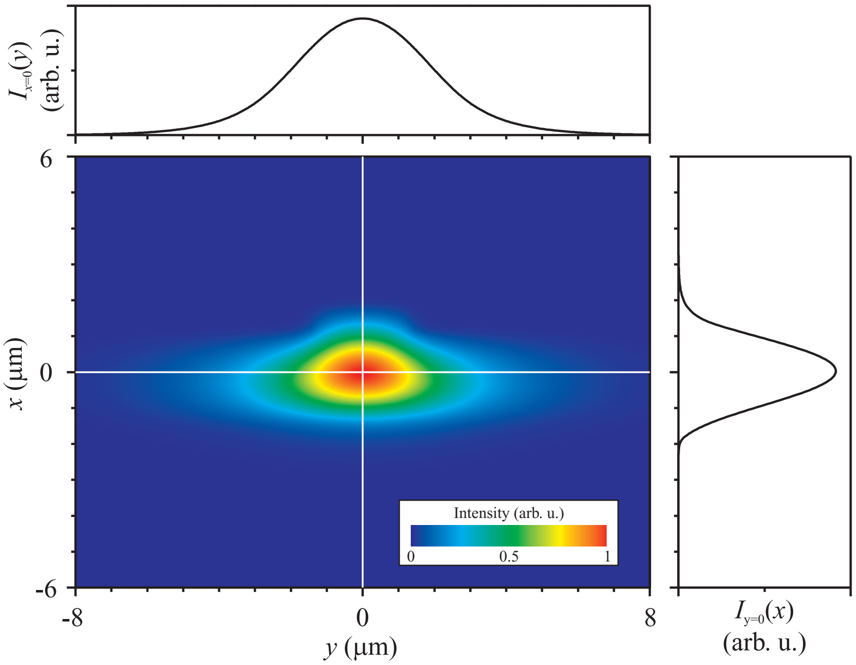

Figure 7.6: Simulated intensity distribution of the fundamental TE mode in a rib-channel waveguide as well as the intensity profiles $I_{\mathrm{x}=0}(y)$ and $I_{\mathrm{y}=0}(x)$ for $x = 0$ and $y = 0$, respectively. The simulation was performed for the investigated 3.1 µm thick Er:(Gd, Lu)$_2$O$_3$ film, a channel width of 3 µm and a wavelength of 1480 nm.

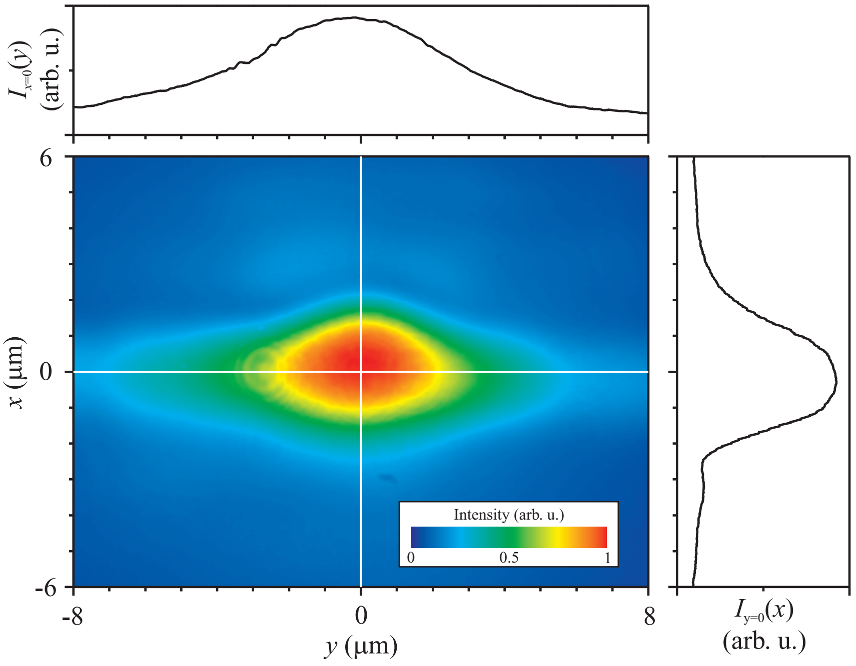

Figure 7.7: Measured transverse intensity profile (near-field image) of 1480 nm light, outcoupled from a rib-channel waveguide of the 3.1 µm thick Er:(Gd, Lu)$_2$O$_3$ film.

Figures 7.6 and 7.7 show the simulated and measured intensity profiles, respectively. The measured profile is broader than the simulated one. This is possibly due to the detection of scattering light and light coupled into the substrate, the top cladding as well as into the planar parts of the waveguiding film. A non-linear behavior of the camera due to saturation, and deviations of the actual channel waveguide geometry from the one used in the simulation are possible reasons as well. A comparison of the two intensity profiles indicates that the actual light confinement in the doped regions may be lower than the simulated confinement given in Tab. 7.3.

7.4 Propagation Loss Measurements

For the realization of amplifying waveguide structures and waveguide lasers, it is essential that the internal losses the propagating light experiences are lower than the gain.[14] Two types of propagation losses are considered in the following, absorption losses and parasitic losses. The former describe the attenuation of light due to resonant absorption by the RE ions, whereas all other loss mechanisms will be referred to as parasitic losses. The determination of these losses is described in the following.

7.4.1 Planar Waveguide Losses

This section describes the measurement of the parasitic losses experienced within the planar parts of the investigated waveguides. Although the laser and gain experiments were performed with channel waveguides, the measurement of the planar waveguide losses is useful, as they are related to both the channel waveguide losses and the film quality.

A straight-forward method for the determination of the propagation losses is the *cut-back technique* [Kec72], in which single-pass transmission measurements are performed on a repeatedly shortened waveguide and the losses are extrapolated to a waveguide length of zero. In contrast to optical fibers, the shortening of rigid short planar waveguides involves the removal of the sample from the optical setup, which makes it complicated to reproduce the input coupling. Therefore, the *cut-back technique* often leads to very inaccurate results for such waveguides. Another disadvantage of the *cut-back technique* is that the waveguide is destroyed in the shortening process. To circumvent both problems, a prism can be used to couple light out of the waveguide at different positions [Zer71, Web73]. Such measurements were performed in cooperation with the University of Twente, but led to very inaccurate results for the relatively short waveguides.

Another approach is to detect the light that is scattered out of the waveguide at different positions [Oka83]. By imaging the waveguide surface onto the chip of a camera, the longitudinal distribution of the scattered light along the direction of propagation (z-direction) can be measured. Assuming that the intensity $I_{\mathrm{sc}}(z)$ of the detected scattering light is proportional to the intensity $I(z)$ of the light propagating in the film

$$I(z) = S \cdot I_{\mathrm{sc}}(z), \tag{7.5}$$

---

[14] During steady-state laser operation, the total losses including the output coupling are equal to the gain.

and that the proportionality factor S is independent of z, the attenuation coefficient α can be determined by fitting with the following equation [Hun02]:

$$I(z) = I(0)\,\exp\left[-\alpha z\right] \tag{7.6}$$

However, the premise that S is independent of z is not always fulfilled. In case of an inhomogeneous distribution of the scattering centers within the waveguide or an unequal angular intensity distribution of the scattered light, the method can be very inaccurate. Another disadvantage is that also light which is not coupled into the waveguiding film might be detected. Hence, an improved technique circumventing both problems has been developed. It is based on the determination of the longitudinal distribution of fluorescence light along the waveguiding direction.

A similar approach has already been proposed by [Oka85, Wei98], but without differentiation between parasitic and absorption losses. Since the measurement relies on the generation of fluorescence light, the absorption losses can usually not be neglected. Hence, a new method using multiple excitation wavelengths has been devised in order to distinguish between these types of losses.

Description of the Loss-Measurement Method

Instead of measuring the intensity of the light which is scattered out of the waveguide, light which is resonant to ground state transitions of the active ions in the doped film is coupled into the waveguide and the generated fluorescence is detected. The method is based on the premise that $I(z)$ can be derived from the fluorescence intensity $I_{\text{flu}}(z)$. In the following, it is assumed that both intensities are proportional to each other:

$$I(z) = E \cdot I_{\text{flu}}(z) \tag{7.7}$$

In contrast to the proportionality factor S in Eq. (7.5), which may depend on z, the factor E is for low intensities often independent of z. This is due to the generally higher distribution homogeneity of the active ions in comparison to that of the scattering centers[15] and the high angular uniformity of the fluorescence radiation. The detection of fluorescence light instead of scattered light thus allows one to obtain $I(z)$ independently of the local scattering. The method is therefore applicable for waveguides that do not possess a perfectly homogeneous scattering center distribution. Another advantage of the fluorescence-based method is that only light which is propagating in the doped layer is absorbed and thus contributes to $I_{\text{flu}}(z)$. Therefore, the measurement is less affected by light which is not coupled into the waveguiding layer. As a trade-off, the method is only applicable to active waveguides.

---

[15] The number of dopant ions is expected to be much larger than the number of scattering centers. Hence, assuming both the dopant ions and the scattering centers to be statistically distributed within the waveguide, a much higher homogeneity is expected for the distribution of the former.

While the determination of the propagation losses by the detection of scattered light is usually performed at a wavelength far away from any resonance and the absorption losses can thus be neglected, this is not the case for the fluorescence-based method. The attenuation coefficient α obtained by fitting with Eq. (7.6) contains both parasitic and absorption losses, which are described by the attenuation coefficients α_L and α_{abs}, respectively. In order to separate both loss coefficients, the measurement is performed at different absorbing wavelengths λ with known relative absorption cross-sections $\sigma_{\text{abs}}(\lambda)/\sigma_{\text{abs, max}}$. Here, $\sigma_{\text{abs, max}}$ is the maximum of $\sigma_{\text{abs}}(\lambda)$ for the investigated wavelengths. Assuming that the variation of α_L with λ is small compared to the corresponding variation of $\alpha_{\text{abs}}(\lambda)$ and that the latter is proportional to $\sigma_{\text{abs}}(\lambda)/\sigma_{\text{abs, max}}$, one has the following relation:

$$\alpha\left(\frac{\sigma_{\text{abs}}(\lambda)}{\sigma_{\text{abs, max}}}\right) = \alpha_L + \alpha_{\text{abs}}(\lambda) = \alpha_L + \alpha_{\text{abs, max}} \cdot \frac{\sigma_{\text{abs}}(\lambda)}{\sigma_{\text{abs, max}}} \tag{7.8}$$

By fitting the measured attenuation coefficients $\alpha(\sigma_{\text{abs}}(\lambda)/\sigma_{\text{abs, max}})$ with Eq. (7.8), the coefficients $\alpha_{\text{abs, max}}$ and α_L, describing the maximum absorption[16] and the parasitic losses, can be obtained.

Experimental Procedure

Using the method described above, the propagation losses of the 1.0 µm thick Er:Y_2O_3 waveguide, prior to deposition of the SiO_2 top cladding, were determined. The loss measurement was possible in spite of the bad polishing quality of the end facets, since the measurement technique is applicable even with low coupling efficiencies. Figure 7.8 shows the experimental setup.

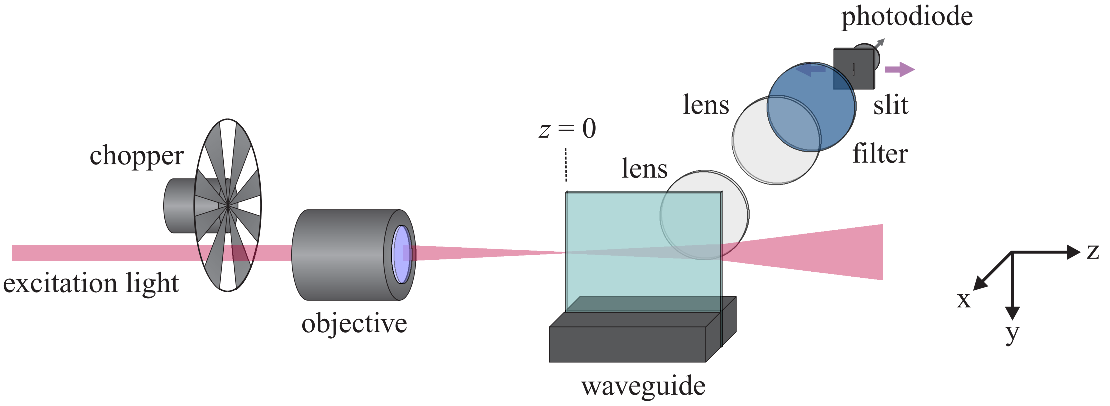

Figure 7.8: Loss-measurement setup using a moveable photodiode behind a slit to determine the intensity of the fluorescence light $I_{\text{flu}}(z)$ as a function of the z-position from where it originated within the waveguide

---

[16] more precisely, the maximum absorption for the investigated wavelengths

A tunable Ti:Al_2O_3 laser[17] served as excitation source. Its beam was coupled into the waveguide by use of a microscope objective with a NA of 0.35. Using two lenses[18], an image of the y-z-surface of the waveguide was created. By placing a moveable germanium photodiode covered by a slit in the plane of the image and scanning the position of both the photodiode and the slit along the z-direction, the spatial intensity distribution $I_{\text{flu}}(z)$ of the generated fluorescence light was obtained. In order to ensure the detection of fluorescence light only, the photodiode was covered by a filter[19] blocking the scattered excitation light. In addition, the laser beam was periodically interrupted by use of a chopper and the lock-in technique was applied.

The measurement was performed at four different excitation wavelengths between 800 nm and 822 nm (see Tab. 7.4), corresponding to absorption peaks of $^4\mathrm{I}_{15/2} \rightarrow {}^4\mathrm{I}_{9/2}$ transitions. Assuming that the measured fluorescence intensity $I_{\text{flu}}(z)$ of the $^4\mathrm{I}_{13/2} \rightarrow {}^4\mathrm{I}_{15/2}$ and $^4\mathrm{I}_{11/2} \rightarrow {}^4\mathrm{I}_{15/2}$ transitions is proportional to the local intensity $I(z)$ of the excitation light and fitting the experimental results for $I(z)$ to match Eq. (7.6), the attenuation coefficient α was obtained for each of the investigated wavelengths (see Tab. 7.4).

The assumption that $I_{\text{flu}}(z)$ is proportional to $I(z)$ is only fulfilled, if saturation effects can be neglected. Hence, the saturation intensities I_{sat} for the relevant $^4\mathrm{I}_{15/2} \rightarrow {}^4\mathrm{I}_{9/2}$ transitions were estimated. Upconversion processes as well as absorption from excited states were neglected and solely the $^4\mathrm{I}_{15/2}$, $^4\mathrm{I}_{13/2}$, $^4\mathrm{I}_{11/2}$ and $^4\mathrm{I}_{9/2}$ manifolds were considered. These manifolds, which consist of thermally coupled Stark levels, were treated as single energy levels $i = 0, 1, 2, 3$ (in the order of increasing energy) with populations N_i and lifetimes τ_i. Since the $^4\mathrm{I}_{9/2}$ manifold possesses an extremely short total lifetime τ_3 of less than 0.5 µs in Er(1%):Y_2O_3 [Pet98] and a significantly longer radiative lifetime $\tau_{\text{rad},3}$ of (4.5 ± 0.8) ms [Web68], it was assumed that any excitation of this level instantly decays non-radiative to the $^4\mathrm{I}_{11/2}$ level. The population N_3 of the $^4\mathrm{I}_{9/2}$ level was thus approximated to be zero. Neglecting reabsorption of spontaneously emitted photons, the following rate equations are obtained:

$$\frac{dN_2}{dt} = -\frac{N_2}{\tau_2} + W_{\text{abs}}\,N_0 \tag{7.9}$$

$$\frac{dN_1}{dt} = -\frac{N_1}{\tau_1} + \eta'\,\frac{N_2}{\tau_2} \tag{7.10}$$

$$N_{\text{t}} = N_0 + N_1 + N_2 \tag{7.11}$$

Here, η' is the branching ratio of the $^4\mathrm{I}_{11/2} \rightarrow {}^4\mathrm{I}_{13/2}$ transitions, which takes both radiative and non-radiative decays into account. At the saturation intensity I_{sat}, the absorption coefficient

$$\alpha_{\text{abs}}(\lambda) = \sigma_{\text{abs}}(\lambda)\,N_0 - \sigma_{\text{em}}(\lambda)\,N_3 = \sigma_{\text{abs}}(\lambda)\,N_0 \tag{7.12}$$

---

[17] Spectra-Physics 3900s, pumped by a Millennia Xs laser

[18] In order to minimize abberations, two achromatic doublets were used.

[19] A dichroic mirror was used for this purpose.

is equal to half the small-signal absorption coefficient introduced in Eq. (2.51). Hence, for $I = I_{\mathrm{sat}}$, one obtains the following relations:

$$\begin{aligned} \sigma_{\mathrm{abs}}\, N_0 &= \tfrac{1}{2}\, \sigma_{\mathrm{abs}}\, N_{\mathrm{t}} && (7.13) \\ N_0 &= \tfrac{1}{2}\, N_{\mathrm{t}} && (7.14) \end{aligned}$$

Solving the system of equations (7.9), (7.10), (7.11) and (7.14) for the steady-state[20], leads to

$$W_{\mathrm{abs}} = \frac{1}{\eta'\, \tau_1 + \tau_2}. \tag{7.15}$$

With the equations (2.43) and (7.15), the saturation intensity can be determined:

$$I_{\mathrm{sat}} = \frac{h\nu}{\sigma_{\mathrm{abs}}\, (\eta'\, \tau_1 + \tau_2)} \tag{7.16}$$

The results are summarized in Tab. 7.4. A lifetime τ_1 of 6.6 ms (see Tab. 6.3) and a branching ratio η' of 0.39, which had been determined in [Kue09a] for the $^4\mathrm{I}_{11/2} \rightarrow {}^4\mathrm{I}_{13/2}$ transitions of an Er:Y_2O_3 bulk crystal, were used for the calculation. The lifetime τ_2 was assumed to be 1.8 ms, the value determined for the Er(1%):Y_2O_3 film investigated in section 6.2.1.[21] Since it had been shown that the Er:Y_2O_3 film spectra are similar to those of bulk crystals, the absorption cross-sections σ_{abs} were determined by transmission measurements[22] of an Er:(0.3%):Y_2O_3 bulk crystal[23]. The resulting absorption spectrum is shown in the inset of Fig. 7.10.

λ (nm)	σ_{abs} $(10^{-21}\,\mathrm{cm}^2)$	I_{sat} $\left(\frac{\mathrm{kW}}{\mathrm{cm}^2}\right)$	$\frac{\sigma_{\mathrm{abs}}}{\sigma_{\mathrm{abs,\,max}}}$	α $\left(\frac{1}{\mathrm{cm}}\right)$
800.1	3.16	18.0	0.808	1.82 ± 0.09
804.2	3.92	14.4	1	2.15 ± 0.19
813.8	1.44	38.8	0.367	1.47 ± 0.09
821.5	0.467	118	0.119	1.05 ± 0.14

Table 7.4: Absolute and relative absorption cross-sections σ_{abs}, saturation intensities I_{sat} as well as the measured attenuation coefficients α (with fitting errors) at the four different wavelengths λ used for the loss measurement of the planar Er(1%):Y_2O_3 waveguide

---

[20] In the steady state, the time derivatives of the rate equations are zero.

[21] Since double-exponential fit functions were used for the determination of the $^4\mathrm{I}_{13/2}$ lifetimes in section 6.2.1, the $^4\mathrm{I}_{11/2}$ lifetimes were obtained as well.

[22] The spectral bandwidth of the measurement was 0.3 nm.

[23] The same Er:(0.3%):Y_2O_3 bulk crystal as in section 6.2.1 was examined.

The experiment was performed with an incident light power P_{in} of 5 mW, which was measured prior to coupling into the waveguide. In order to roughly estimate $I(z)$, the divergence angle ψ of the light propagating in the planar waveguide (see Fig. 7.9) was calculated by use of Eq (7.17), which can be derived from Snell's law [Sal91].

$$\psi = \arcsin\left(\frac{n_0}{n_3}\sin\theta\right) \tag{7.17}$$

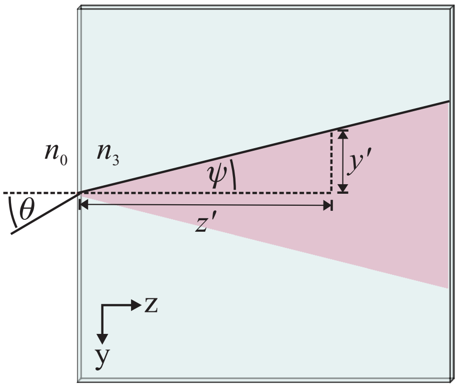

Figure 7.9: Light propagation in a planar waveguide

The NA of the incoupling objective corresponds to a maximum convergence angle θ of 20.5° and thus to a maximum beam divergence ψ of 10.6°. Figure 7.9 illustrates the diverging beam. Fluorescence measurements were performed for z-positions ranging from 3 to 7 mm, thus avoiding regions near the waveguide end-facets.[24] Using a ray-optical calculation, the beam width $2y'$ in y-direction was approximated to be 1.1 mm at the position of the first intensity measurement ($z = 3$ mm). Due to light confinement, the beam width $2x'$ in x-direction can be approximated by the film thickness of 1 µm. Thus, the intensity $I(z = 3\,\mathrm{mm})$ has been estimated to be 0.45 kW/cm^2, which is significantly lower than the calculated saturation intensities. Considering coupling losses due to Fresnel reflections and scattering at the incoupling end-facet as well as the losses experienced in the first 3 mm of propagation, $I(z = 3\,\mathrm{mm})$ is most likely even lower than the estimated value of 0.45 kW/cm^2. Saturation effects are thus neglected and it is assumed for the loss measurement that $I_{\mathrm{flu}}(z)$ is proportional to $I(z)$ and that α_{abs} is proportional to σ_{abs}.

In order to separate absorption and parasitic losses, the determined attenuation coefficients $\alpha(\sigma_{\mathrm{abs}}(\lambda)/\sigma_{\mathrm{abs,\,max}})$ were extrapolated to a regime without absorption ($\sigma_{\mathrm{abs}}(\lambda)/\sigma_{\mathrm{abs,\,max}} = 0$), by fitting with Eq. (7.8). Since the linewidth $\Delta_{\mathrm{FWHM}} = 0.1$ nm of the Ti:Al$_2$O$_3$ laser used as excitation source was lower than the linewidth of the investigated absorption peaks, the line shape of the excitation light was not taken into account. Figure 7.10 shows the individual attenuation coefficients and the resulting fit function. The attenuation α_L due to parasitic losses has been determined to be $(1.02 \pm 0.12)\,\mathrm{cm}^{-1}$, which corresponds to losses L of (4.4 ± 0.5) dB/cm.[25]

---

[24] Reflections and scattering at the end-facets can falsify the result of the loss measurement.

[25] The conversion formula for α_L in cm^{-1} and L in dB/cm is: $L \approx 4.3\,\mathrm{dB} \cdot \alpha_L$

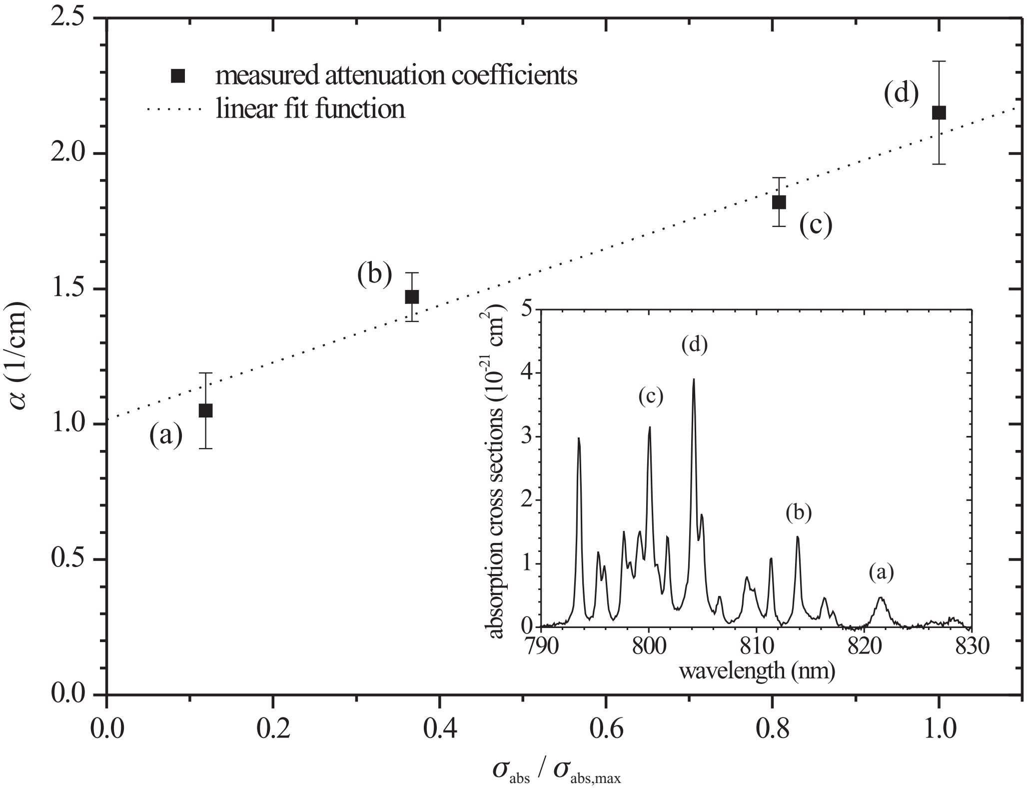

Figure 7.10: Attenuation coefficients α measured at four excitation wavelengths λ with different relative absorption cross-section $\sigma_{\text{abs}}(\lambda)/\sigma_{\text{abs, max}}$. The determined α were linearly fitted with Eq. (7.8) and the attenuation α_L due to parasitic losses was obtained as intersection of the resulting line and the ordinate. In the inset, the corresponding absorption spectrum (0.3 nm resolution) is displayed. The letters (a)-(d) refer to the investigated absorption peaks.

Results and Discussion

The parasitic losses experienced in the planar parts of the other waveguides as well as those of the Er:Y_2O_3 film after deposition of the SiO_2 top cladding were determined in a similar way [Hei09]. All loss measurements were performed at wavelengths between 792 nm and 822 nm. Since the determination of film absorption spectra proved to be complicated and no comparable Nd:$(Gd, Lu)_2O_3$ and Er:$(Gd, Lu)_2O_3$ bulk crytstals were available, the relative absorption cross-sections were estimated from excitation spectra, which were recorded as described in section 5.4.1. The measured parasitic losses are summarized in Tab. 7.6.

Deposition of a cover layer significantly reduced the losses experienced in the 1.0 µm thick Er:Y_2O_3 film. Since the maximum number of guided modes remains unaffected by the top cladding (see Fig. 7.2), the lower losses are most likely due to the reduced difference between the refractive index of the particulates protruding from the waveguiding film and that of the surrounding medium. A reduction of the scattering losses by burying particulates was also pointed out in [Eas07]. Hence, all waveguides prepared for gain and laser experiments were covered with an amorphous top cladding.

The waveguide losses also depend on the number of guided modes. Due to the greater sensitivity of higher-order modes on surface scattering, higher losses are expected for these modes [Hun02]. The correlation between the propagation losses and the number of the excited mode was also investigated in [Lan99] for a pulsed laser deposited Nd:$YAlO_3$ film. While losses below 1 dB/cm were measured for the TE_0 mode, the losses of the TE_9 mode were determined to be 16.1 dB/cm. A similar behavior is hinted by a comparison of the 1.9 µm thick Nd:$(Gd, Lu)_2O_3$ film and the 3.1 µm thick Er:$(Gd, Lu)_2O_3$ film, which possess similar particulate density. While at $\lambda = 800$ nm only two TE modes can be guided in the former, the latter supports up to four guided TE modes at this wavelength (see Fig. 7.3). The significantly higher losses in the thicker waveguide may thus be explained by the higher number of guided modes. However, since a contrary tendency to lower planar waveguide losses was observed in [Bar00] when increasing the film thickness from 2 µm to 8 µm, further investigations are required.

The detrimental effect of the particulates on the waveguide losses is noticeable by comparing the Er:Y_2O_3 and the Nd:$(Gd, Lu)_2O_3$ film. While both films are supporting two TE modes at a wavelength of 800 nm, significantly higher losses were measured for the Nd:$(Gd, Lu)_2O_3$ waveguide, which possesses the higher particulate density. The significant impact of the particulate density on the performance of planar waveguide lasers is examined in [Bar00]. Therein, pulsed laser deposited Nd:$Gd_3Ga_5O_{12}$ films with particulate densities comparable to the ones fabricated in the framework of this thesis were investigated. An increase in particulate density from 3.5×10^4 to $9.7 \times 10^5\,\mathrm{cm}^{-2}$ resulted in an increase of the laser threshold from 2.5 mW to 167 mW of absorbed pump power.

However, this thesis focusses on channel waveguides. The local distribution of scattering centers is expected to have a greater impact on the losses of individual waveguide channels than on the ones experienced in planar waveguides. In the latter, the light propagates in a relatively large area of the waveguiding film and the losses thus depend on the average density of the more or less homogeneously distributed particulates. The losses of a given waveguide channel, however, strongly depend on the presence of individual particulates at the channel region.

7.4.2 Channel Waveguide Losses

While the two-dimensional light confinement in channel waveguides is often beneficial for laser applications, the resulting high intensities are problematic for the loss measurements with the method described in section 7.4.1. Assuming a homogeneous distribution of the incident light power $P_{\text{in}} = 5\,\text{mW}$ in an area of $5\,\mu\text{m} \times 3\,\mu\text{m}$, the intensity within a waveguide channel of the 3.1 µm thick $\text{Er:(Gd, Lu)}_2\text{O}_3$ film can be roughly estimated to be $30\,\text{kW/cm}^2$, which is in the order of magnitude of the saturation intensities given in Tab. 7.4. Since the signal-to-noise ratio was already very low for the measurements performed with $P_{\text{in}} = 5\,\text{mW}$, the power of the incident light could not be significantly reduced any further. Hence, saturation effects could not be neglected and the above mentioned method was not applied to channel waveguides.

A technique based on optical low coherence reflectometry (OLCR) was used instead [Che05].[26] However, the measurement was not successful. Most likely the signal intensity provided by the OLCR setup[27] and the coupling efficiency were not sufficiently high for the loss measurement of high-loss waveguides with a low end-facet reflectivity. Other interference based methods, such as the Fabry-Perot resonance technique [Reg85], were not employed, since inaccuracies due to inclinations of the end-facets as well as their relatively low reflectivity were expected [Tit93].

So far, only the combined coupling and propagation losses of several waveguide channels were determined by single-pass transmission measurements. For this, laser light was coupled into the waveguide channel with a microscope objective and the outcoupled light was collected with another objective. The outcoupled laser power P_{out} was compared to the power P_{in} measured before coupling into the waveguide. Taking the reflectance of both end facets and the transmittance of the outcoupling objective into account, the total waveguide losses L_{total} were determined as follows:

$$L_{\text{total}} = -10 \cdot \log \frac{P_{\text{out}}}{P_{\text{in}}}\,\text{dB} \tag{7.18}$$

The loss measurements of the Nd^{3+} and Er^{3+} doped waveguides were performed with a $\text{Ti:Al}_2\text{O}_3$ laser at $\lambda = 780\,\text{nm}$ and a He-Ne laser at $\lambda = 633\,\text{nm}$, respectively. At these wavelengths, the absorption cross-sections are very low and absorption losses could thus be neglected. However, additional coupling losses, such as those resulting from an imperfect overlap between the intensity profiles of the incident light and the waveguide mode, are still included in L_{total}.

---

[26] The measurements were performed in cooperation with the Ecole Polytechnique Fédérale de Lausanne.

[27] Hewlett Packard 8504B

Since the waveguide channels are unequally affected by particulates, the measured losses depend strongly on the individual channel for which the measurement is performed. Hence, it is possible that the losses of certain channels are lower than the losses experienced in the planar part of the waveguiding film. The total losses of the specific channel for which Nd^{3+} laser action was demonstrated (see section 8.1) have been determined to be 6.4 dB. Since light propagation in all channels of the 3.1 µm thick $\mathrm{Er{:}(Gd,Lu)_2O_3}$ film was severely affected by particulates, the total losses for this waveguide were not calculated. In the 1.0 µm thick $\mathrm{Er{:}(Gd,Lu)_2O_3}$ film, however, a promising channel with total losses of 4.4 dB was identified.

In order to derive the propagation losses from the total losses, the coupling efficiency ξ has to be determined. For coupling from a single-mode source into a single-mode waveguide, this can be done by calculating the overlap integral between the electric field distributions of the incident light and the waveguide mode [McC83].

The loss measurements of the $\mathrm{Nd{:}(Gd,Lu)_2O_3}$ waveguide were performed subsequent to the laser experiments (see section 8.1) with similar coupling and shape of the pump beam. While the coupling was optimized for laser performance, this does not necessarily imply that the pump beam is single mode. Nevertheless, a rough estimation of the coupling efficiency is made for this waveguide; coupling of a single-mode pump beam with Gaussian profile and beam width ω_0 into the fundamental TE mode of the waveguide is assumed. By use of Eq. (7.2), the minimum beam width, which can be obtained at $\lambda = 820\,\mathrm{nm}$ by focussing with the incoupling objective ($\mathrm{NA} = 0.35$, $\theta_{\mathrm{max}} = 0.36$), has been calculated to be 0.7 µm. Hence, the overlap of the Gaussian beam profile and the simulated waveguide mode was calculated for various $\omega_0 \geq 0.7\,\mu\mathrm{m}$.[28] The results are displayed in Fig. 7.11.

For ω_0 between 0.7 µm and 3.5 µm, the simulated ξ has a value between 40 % and 70 %. Since larger pump-beam widths are not expected, the coupling efficiency is most likely in the range mentioned above. While the actual beam shape and thus coupling efficiency is yet to be measured, the upper limit of the propagation losses has been determined by assuming a coupling efficiency $\xi = 1$. This results in propagation losses $L < 6.1\,\mathrm{dB/cm}$ and $L < 10.7\,\mathrm{dB/cm}$ for the 7.2 mm long $\mathrm{Er{:}(Gd,Lu)_2O_3}$ waveguide and the 6 mm long $\mathrm{Nd{:}(Gd,Lu)_2O_3}$ waveguide, respectively.

It has been shown in [Bra07] that only small additional losses in the order of 0.1 dB/cm (at $\lambda = 1523\,\mathrm{nm}$), such as scattering losses caused by the sidewall roughness of the straight channels, are introduced by the structuring process described in section 7.1. The relatively high measured losses are thus most probably due to a poor film quality.

The losses were measured at wavelengths below the promising laser wavelengths of 1079 nm and 1535 nm. Their wavelength dependence has thus to be considered. While scattering at imperfections smaller than the wavelength λ can be described by a λ^{-4} dependence[29] [Pin73], other models such as the Mie theory [Mie08] have to be considered to describe scattering at particulates in the micrometer range.

---

[28] Both the mode simulation and the overlap calculation were performed with the software *FieldDesigner*.

[29] This is in agreement with the Rayleigh law of scattering.

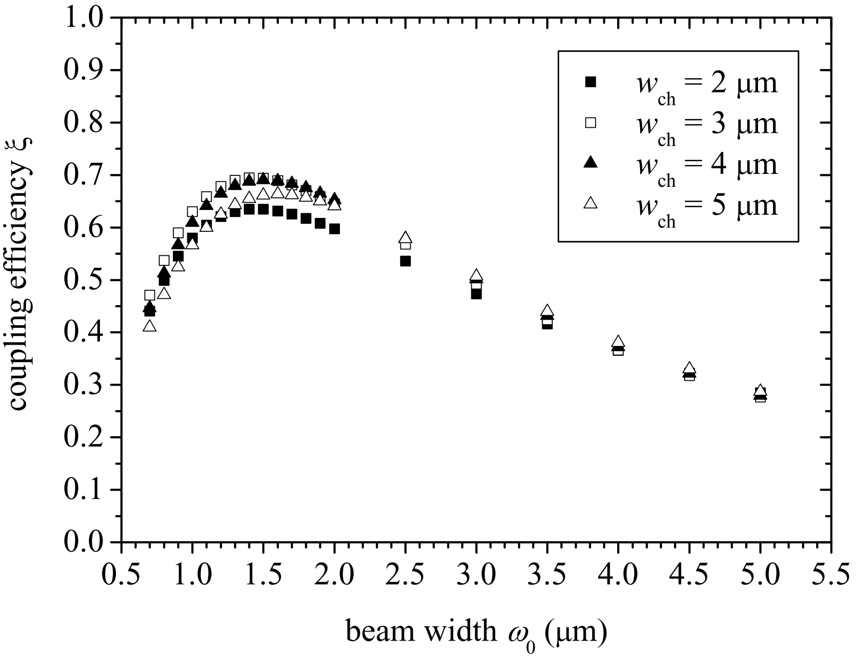

Figure 7.11: Overlap between simulated rib-channel waveguide modes of the Nd:$(\mathrm{Gd},\mathrm{Lu})_2\mathrm{O}_3$ sample and Gaussian beam profiles with beam widths ω_0. Several channel widths w_{ch} were considered. According to [McC83], the overlap corresponds to the coupling efficiency ξ.

Generally, the Mie-scattering cross-section σ_{Mie} depends on the ratio λ/r_{sc} of the wavelength of the scattered light and the radius r_{sc} of the scattering center. For $\lambda/r_{\mathrm{sc}} \ll 1$, the wavelength dependence of σ_{Mie} can be neglected and for $\lambda/r_{\mathrm{sc}} \gg 1$ one has the λ^{-4}-Rayleigh law of scattering. However, for scattering centers with radii in the same order of magnitude than the wavelength, $\sigma_{\mathrm{Mie}}(\lambda)$ shows an oscillating behavior. Nevertheless, the wavelength dependence in this regime can, in certain circumstances, be neglected. Here, scattering at a large number of particulates is considered and the radii of these scattering centers are assumed to be randomly distributed between values smaller than the shortest considered wavelength and larger than the longest one. As in [Ina76], the losses due to Mie scattering at scattering centers comparable to or larger than λ are thus assumed to be wavelength independent. In that case, the attenuation α_{sc} due to scattering can be approximately described with the following equation [Ina76]:

$$\alpha_{\mathrm{sc}} = A' \cdot \lambda^{-4} + B' \tag{7.19}$$

Since the positive coefficients A' and B' are independent of λ, the scattering losses are decreasing with longer wavelengths. Thus, the losses at the potential laser wavelengths mentioned above are expected to be lower than the measured ones.

7.5 Gain in Channel Waveguides

On the one hand, the promising spectroscopic properties of the fabricated films should lead to a high optical gain. The measured propagation losses, on the other hand, are quite high as well. Waveguide amplifiers and lasers can only be realized if the gain is higher than the propagation losses. Hence, the maximum small-signal gain obtainable for the Er:$(\mathrm{Gd},\mathrm{Lu})_2\mathrm{O}_3$ and Nd:$(\mathrm{Gd},\mathrm{Lu})_2\mathrm{O}_3$ waveguides was calculated and pump-probe experiments were performed in order to measure the actual gain in the Er^{3+} doped ones.

7.5.1 Theoretical Gain

In this section, a simplified model for the gain calculations in channel waveguides is described. Interionic processes, excited state absorption (ESA) and amplified spontaneous emission[30] are neglected and the pump intensity is assumed to be high enough to completely bleach the waveguide channel on the pump transition. More complex treatments can be found in [Hoe94, Din94]. In order to describe the gain experienced in the investigated channel waveguides, the gain coefficient $g(\lambda)$ defined in Eq. (2.49) is modified by taking the confinement Γ (see Tab. 7.3) of the guided light to the doped layer into account:

$$g'(\lambda) = \Gamma \cdot (\sigma_{\mathrm{em}}(\lambda)\, N_{\mathrm{u}} - \sigma_{\mathrm{abs}}(\lambda)\, N_{\mathrm{l}}) \tag{7.20}$$

Apart from that, it is assumed that the gain coefficient $g'(\lambda)$ is constant for the entire transverse mode profile. The confinement factor Γ is approximated to be independent of λ in the investigated wavelength interval. Introducing the gain cross-section $\sigma_{\mathrm{gain}}(\lambda)$ as follows

$$\sigma_{\mathrm{gain}}(\lambda) := \frac{N_{\mathrm{u}}}{N_{\mathrm{t}}}\,\sigma_{\mathrm{em}}(\lambda) - \frac{N_{\mathrm{l}}}{N_{\mathrm{t}}}\,\sigma_{\mathrm{abs}}(\lambda), \tag{7.21}$$

Eq. (7.20) can be simplified to

$$g'(\lambda) = \Gamma \cdot \sigma_{\mathrm{gain}}(\lambda) \cdot N_{\mathrm{t}}. \tag{7.22}$$

Assuming that $g'(\lambda)$ is constant along the entire waveguide length l, the evolution of the signal intensity $I_{\mathrm{s}}(\lambda,\, z)$ for light propagation in z-direction within the waveguide can be derived from Eq. (2.50):

$$I_{\mathrm{s}}(\lambda,\, z) = I_{\mathrm{s}}(\lambda, 0)\, \exp\left[g'(\lambda)\, z\right] \tag{7.23}$$

Here, the intensity change due to stimulated emission and absorption is considered only.

---

[30] The influence of amplified spontaneous emission (ASE) on the gain characteristics of an Er^{3+} doped Ti:LiNbO_3 channel waveguide was investigated in [Din94] and was negligible for pump powers in the order of 100 mW and below.

Er^{3+} Doped Waveguides

As shown in section 3.2.2, in-band pumping of Er^{3+} doped sesquioxides is beneficial. In waveguide geometries, in-band pumping offers additional advantages over pumping at 975 nm, which are due to the smaller wavelength difference with respect to the signal or laser light; a higher modal overlap can be realized and for amplifiers the coupling is facilitated, because of similar optimal conditions for the pump and signal light. Hence, this pumping scheme was used for the gain and laser experiments. Neglecting all interionic processes as well as ESA[31], the only manifolds of interest are the $^4I_{15/2}$ and $^4I_{13/2}$ ones. Since these manifolds consist of thermally coupled Stark levels, they are treated as single energy levels with populations N_l and N_u, respectively. By considering $N_t = N_l + N_u$ and introducing the inversion

$$\beta := \frac{N_u}{N_t}, \tag{7.24}$$

Eq. (7.21) can be simplified to

$$\sigma_{gain}(\lambda) = \beta\, \sigma_{em}(\lambda) - (1-\beta)\, \sigma_{abs}(\lambda). \tag{7.25}$$

In order to obtain a high optical gain, a high inversion β is required. Hence, the maximum inversion β_{max} attainable at the pump wavelength λ_p is calculated. In case of complete bleaching at that wavelength, the following relation can be applied

$$\sigma_{abs}(\lambda_p)\, N_l = \sigma_{em}(\lambda_p)\, N_u, \tag{7.26}$$

and the resulting maximum inversion β_{max} can be derived from the equations (7.24) and (7.26) as follows:

$$\beta_{max} = \frac{\sigma_{abs}(\lambda_p)}{\sigma_{abs}(\lambda_p) + \sigma_{em}(\lambda_p)} \tag{7.27}$$

In order to obtain a high inversion at room temperature, it is beneficial to pump at relatively short wavelengths. Hence, a pump wavelength λ_p of 1480 nm was chosen. At that wavelength, the effective absorption and emission cross-sections of the Er:$(Gd, Lu)_2O_3$ films are $\sigma_{abs} = 2.39 \times 10^{-21}\,cm^2$ and $\sigma_{em} = 7.48 \times 10^{-22}\,cm^2$ (see section 6.2.1). The maximum inversion obtainable by bleaching at 1480 nm is thus $\beta_{max} = 0.76$.

For the determination of the small-signal gain, it is assumed that the signal intensity I_s is significantly lower than the pump intensity I_p. Hence, the influence of the signal light on the inversion is neglected and β depends on the pump intensity only. If the pump intensity is high enough to bleach the entire waveguide, the inversion $\beta = \beta_{max}$ and thus also $g'(\lambda)$ are constant along the waveguide length l. Therefore, Eq. (7.23) can be used to describe the intensity evolution $I_s(z)$ of the signal light due to stimulated emission and absorption in the waveguide.

---

[31] As pointed out in section 3.2.2, excited state absorption is not expected for the investigated pump and signal wavelengths.

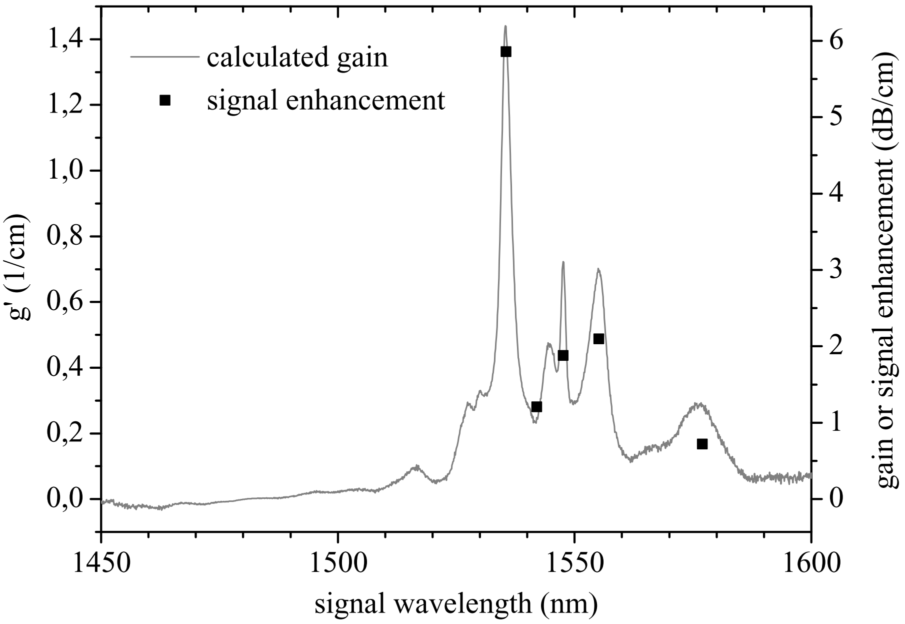

Figure 7.12: Calculated small-signal gain of the 3.1 µm thick Er(0.6 %):$(Gd, Lu)_2O_3$ waveguide for complete bleaching of the waveguide channel at $\lambda_p = 1480\,\text{nm}$, as well as the measured signal enhancement (see section 7.5.3)

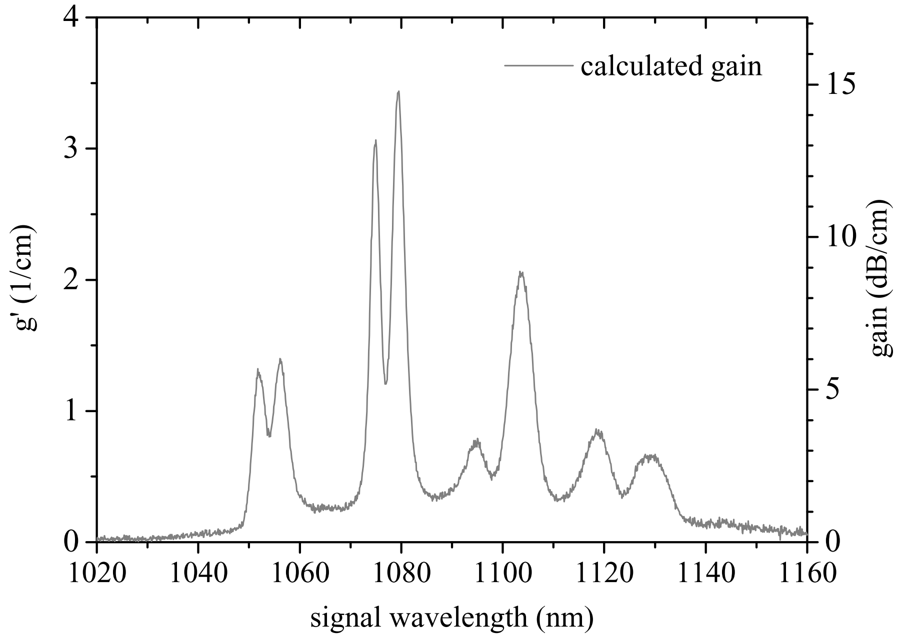

Figure 7.13: Calculated small-signal gain of the Nd(0.5 %):$(Gd, Lu)_2O_3$ waveguide. All active ions are assumed to be excited to the $^4F_{3/2}$ manifold (i.e. $\beta = 1$).

In the following, the gain $g'(\lambda)$ obtainable by total bleaching at $\lambda_p = 1480$ nm is calculated for the waveguide channels of the 3.1 µm thick Er(0.6 %):(Gd, Lu)$_2$O$_3$ film. Considering the simulated values given in Tab. 7.3, the confinement factor Γ is approximated to be 94 %. Since solely the $^4I_{15/2}$ and $^4I_{13/2}$ manifolds are considered, $N_l + N_u$ is equal to the total density of active ions $N_t = 1.61 \times 10^{20}$ cm^{-3}. This value has been calculated for 0.6 % doped Y$_2$O$_3$, which possesses a nearly identical crystal structure and lattice constant as the lattice matched (Gd, Lu)$_2$O$_3$. Similarly as for the losses, the gain G in dB/cm is introduced.[32] The resulting gain spectrum is displayed in Fig. 7.12.

In the channel waveguides of the 3.1 µm thick Er:(Gd, Lu)$_2$O$_3$ film, a maximum gain G_{max} of 6.2 dB/cm can be obtained when pumping at $\lambda_p = 1480$ nm. The theoretical gain in the 1.0 µm thick Er:(Gd, Lu)$_2$O$_3$ waveguide has not been calculated, since the confinement factor could not be reliably estimated (see section 7.3.2).

Nd^{3+} Doped Waveguides

For the calculation of the gain obtainable in the waveguide channels of the Nd:(Gd, Lu)$_2$O$_3$ film, a four-level system consisting of the $^4I_{9/2}$, $^4I_{11/2}$, $^4F_{3/2}$ and $^4F_{5/2}$ manifolds is considered (see Fig. 7.14). These manifolds consisting of thermally coupled Stark levels are treated as single energy levels $i = 0, 1, 2, 3$ (in the order of increasing energy) with populations N_i. Excited state absorption as well as upconversion and cross-relaxation processes are neglected.

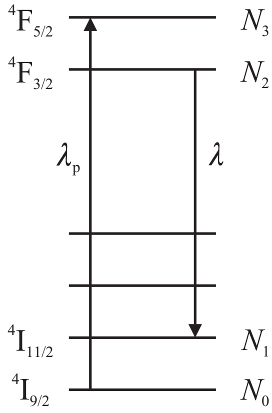

Figure 7.14: Nd^{3+} four-level system

It is assumed in the following that any excitation of the $^4F_{5/2}$ and $^4I_{11/2}$ levels decays completely and almost instantly to the $^4F_{3/2}$ and $^4I_{9/2}$ levels, respectively. According to [For99], this is the case for Nd:Y$_2$O$_3$ bulk crystals. It is expected that the Stark-level energies of the Nd:(Gd, Lu)$_2$O$_3$ film are similar to those of Nd:Y$_2$O$_3$ bulk crystals, since the peak position of their emission spectra are approximately the same (see section 6.2.2) and the similarity of the Stark-level energies has been shown for the Er^{3+} doped films (see section 6.2.1). The maximum phonon energy of the mixed system (Gd, Lu)$_2$O$_3$ is approximated to be 577 cm^{-1} by averaging the phonon energies of its components Gd$_2$O$_3$ and Lu$_2$O$_3$ (see Tab. 3.2), which are contributing almost equally to the solid solution. This approach is justified by [Cha71], stating that the phonon energies of most tertiary ionic mix-crystals shift linearly with the constituent concentration from the phonon energies of one component to those of the other one. Since the phonon energies and the Stark-level energies of Nd:(Gd, Lu)$_2$O$_3$ films and Nd:Y$_2$O$_3$ bulk crystals are comparable, the almost instantaneous decay of the $^4F_{5/2}$ and $^4I_{11/2}$ levels is also expected for the lattice matched Nd:(Gd, Lu)$_2$O$_3$ films.[33]

---

[32] The conversion formula for g' in 1/cm and G in dB/cm is: $G \approx 4.3\,\text{dB} \cdot g'$

[33] The single exponential decay of the $^4F_{3/2} \rightarrow {}^4I_{11/2}$ fluorescence obtained upon excitation of the $^4F_{5/2}$ manifold during the lifetime measurements of the Nd:(Gd, Lu)$_2$O$_3$ film also indicates a fast decay of the $^4F_{5/2}$ manifold.

Hence, the populations N_1 and N_3 are approximated to be zero.[34] Introducing the inversion $\beta := N_2/N_\mathrm{t}$ thus leads to:

$$\sigma_\mathrm{gain}(\lambda) = \beta\, \sigma_\mathrm{em}(\lambda) \tag{7.28}$$

The small-signal gain $g'(\lambda)$ obtainable on ${}^4\mathrm{F}_{3/2} \rightarrow {}^4\mathrm{I}_{11/2}$ transitions is calculated for the waveguide channels of the 1.9 µm thick Nd(0.5 %):(Gd, Lu)$_2$O$_3$ film. It is assumed that due to high pump intensities almost all active ions ($N_\mathrm{t} = 1.61 \times 10^{20}\,\mathrm{cm}^{-3}$) are excited to the ${}^4\mathrm{F}_{3/2}$ level and that the signal intensity is small enough not to affect the resulting inversion of $\beta \approx 1$ significantly. According to the values given in Tab. 7.3, the confinement factor Γ is approximated to be 94 %. The resulting gain spectrum is displayed in Fig. 7.13.

The maximum gain G_max of 14.8 dB/cm (at $\lambda = 1079.5\,\mathrm{nm}$) obtainable in the waveguide channels of the Nd:(Gd, Lu)$_2$O$_3$ film is significantly higher than the maximum gain of 6.2 dB/cm calculated for the Er^{3+} doped sample.

7.5.2 Deteriorative Phenomena

According to the simplified models described above, in which interionic processes are neglected and high pump intensities are assumed, the small-signal gain $g'(\lambda)$ is proportional to the number of active ions. High doping concentrations thus seem beneficial. However, the detrimental effects of high doping concentrations have to be considered, as they affect the performance of lasers and amplifiers.

Er^{3+} Doping

A detailed description of the population mechanisms in erbium-doped solid-state lasers is given in [Pol96]. Here, mainly the ${}^4\mathrm{I}_{13/2}$, ${}^4\mathrm{I}_{13/2} \rightarrow {}^4\mathrm{I}_{9/2}$, ${}^4\mathrm{I}_{15/2}$ upconversion process (see Fig. 7.15) is considered, which depopulates the metastable ${}^4\mathrm{I}_{13/2}$ manifold of Er^{3+}.

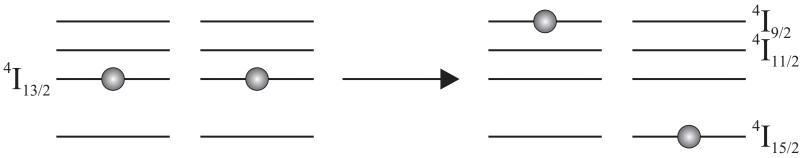

Figure 7.15: Schematic representation of the ${}^4\mathrm{I}_{13/2}$, ${}^4\mathrm{I}_{13/2} \rightarrow {}^4\mathrm{I}_{9/2}$, ${}^4\mathrm{I}_{15/2}$ upconversion process of Er^{3+}

The resulting population of the ${}^4\mathrm{I}_{9/2}$ level decays mostly non-radiative to the ${}^4\mathrm{I}_{11/2}$ one. From that level, a radiative decay into the ground state or another upconversion process, which is illustrated in Fig. 7.16, may occur.

---

[34] Considering the Stark-level energies of Nd:Y$_2$O$_3$ given in [For99], the energy difference between the lowest Stark-levels of the ${}^4\mathrm{F}_{3/2}$ and ${}^4\mathrm{F}_{5/2}$ manifolds is significantly larger than $k_\mathrm{B}\,T$ at room temperature. This also applies to the energy difference between the ${}^4\mathrm{I}_{9/2}$ and ${}^4\mathrm{I}_{11/2}$ manifold. Thus, the thermal occupations of the ${}^4\mathrm{F}_{11/2}$ and ${}^4\mathrm{F}_{5/2}$ manifolds according to Maxwell-Boltzmann statistics are negligible.

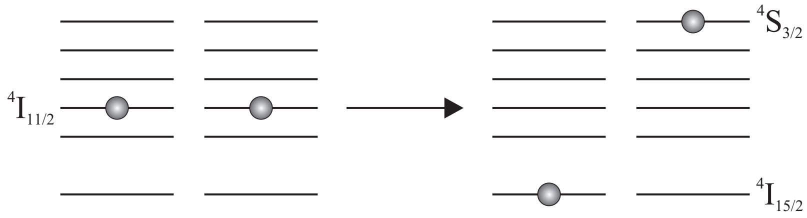

Figure 7.16: Schematic representation of the $^4I_{11/2}$, $^4I_{11/2}$ → $^4I_{15/2}$, $^4S_{3/2}$ upconversion process of Er^{3+}

Due to these upconversion processes, the inversion and thus the gain is reduced. Furthermore, the thermal load of the sample is increased. The resulting change in the relative Stark-level populations and thus the effective cross-sections as well as the resulting spectral broadening are usually detrimental to the gain.

The rate of the initial $^4I_{13/2}$, $^4I_{13/2}$ → $^4I_{9/2}$, $^4I_{15/2}$ upconversion process is $k_{uc} \cdot N_u^2$, with an upconversion coefficient k_{uc} of approximately $0.25 \times 10^{-25}\,m^3/s$ in $Er:Y_2O_3$ [Hoe94]. This upconversion coefficient is smaller than the values of at least $1.5 \times 10^{-25}\,m^3/s$ reported in [Shi90] for Er:YAG. Since most spectroscopic properties of the lattice matched $Er:(Gd, Lu)_2O_3$ films and $Er:Y_2O_3$ bulk crystals have been shown to be comparable, this is also expected for the upconversion coefficient k_{uc}. Hence, k_{uc} is assumed to be lower for the lattice matched films than for Er:YAG. In order to obtain the same upconversion rate as in YAG, the Er^{3+} density N_t in the $(Gd, Lu)_2O_3$ films may thus be slightly higher.

A highly efficient in-band pumped Er:YAG laser was realized with an Er^{3+} concentration of approximately 0.5 % [She06], which corresponds to a doping concentration of approximately 0.25 % in the lattice matched $(Gd, Lu)_2O_3$ films.[35] However, with such low doping concentrations, a maximum gain of merely 2.6 dB/cm is obtainable in the $Er:(Gd, Lu)_2O_3$ waveguides.[36] In order to compensate the high waveguide losses of several dB/cm, a higher doping concentration is most likely required. Therefore, an Er^{3+} concentration of 0.6 % was chosen for first gain and laser experiments in the framework of this thesis. Considering that the upconversion coefficient k_{uc} is about six times smaller in $Er:Y_2O_3$ than in Er:YAG, the $\sqrt{6}$ times larger density of active ions in the $Er:(Gd, Lu)_2O_3$ waveguide is justified.

Nd^{3+} Doping

For typical four-level Nd^{3+} lasers with low losses, the population density of the upper laser level is usually clamped at a relatively low value. However, in order to obtain the high gain necessary to compensate the high losses of the PLD films, much higher populations of the metastable $^4F_{3/2}$ level are required. Due to the waveguide geometry, high pump intensities and thus high inversions can be achieved. The effects of high inversions in planar Nd:YAG waveguides are investigated in [Guy98]. Two energy-transfer processes

---

[35] The density of RE ions is approximately 50 % smaller in YAG ($1.38 \times 10^{22}\,cm^{-3}$ [For99]) than in Y_2O_3.

[36] This value was calculated as in section 7.5.1, for an Er^{3+} concentration of 0.25 % but otherwise identical waveguide parameters.

are considered, self-quenching of Nd^{3+} by cross-relaxation (see Fig. 7.17), and energy-transfer upconversion (see Fig. 7.18).

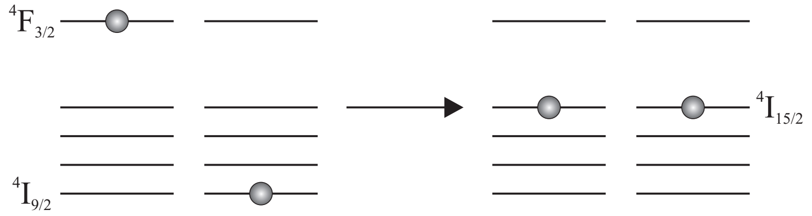

Figure 7.17: Schematic representation of the $^4F_{3/2}$, $^4I_{9/2} \rightarrow {}^4I_{15/2}$, $^4I_{15/2}$ cross-relaxation process of Nd^{3+}. This process is usually followed by a decay of both ions to the ground state.

Due to fluorescence quenching of the $^4F_{3/2}$ lifetime, the threshold of Nd:YAG lasers usually increases with high doping concentrations. Therefore, the optimum Nd^{3+} concentration for Nd:YAG lasers is usually in the vicinity of 1 % [Dan73]. Since the $^4F_{3/2}$, $^4I_{9/2} \rightarrow {}^4I_{15/2}$, $^4I_{15/2}$ cross-relaxation process is depending on the ground-state population, it is expected to have a lower impact at high pump intensities emptying the $^4I_{9/2}$ manifold. Thus, higher doping concentrations might be beneficial in a waveguide geometry. Furthermore, the threshold power of channel waveguide lasers is usually very low, as high pump intensities can be obtained with relatively low pump powers. Hence, an increase of the laser threshold due to self-quenching is often not as relevant as in bulk lasers. At high population densities of the metastable $^4F_{3/2}$ level, however, $^4F_{3/2}$, $^4F_{3/2} \rightarrow {}^4I_{11/2}$, $^2G_{9/2}$ upconversion can become a significant gain-reducing process and limits the Nd^{3+} concentration for optimum laser performance.

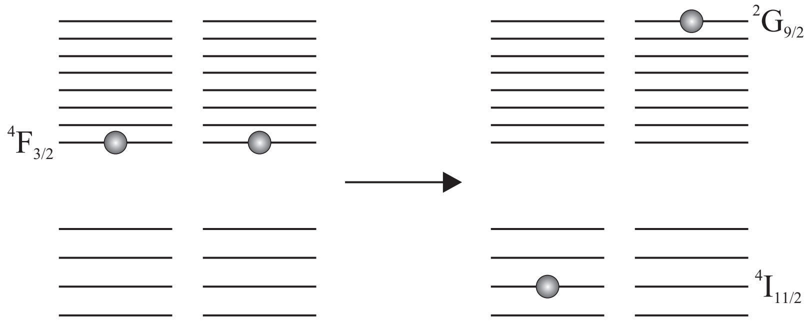

Figure 7.18: Schematic representation of the $^4F_{3/2}$, $^4F_{3/2} \rightarrow {}^4I_{11/2}$, $^2G_{9/2}$ upconversion process of Nd^{3+}

The effect of upconversion on the small-signal gain of a Nd(1 %):YAG amplifier is investigated in [Guy98]. In that publication, an inversion β of approximately 0.7 has been calculated for an incident pump intensity five times higher than the saturation intensity

$$I_{\text{sat}} = \frac{h\,c_0}{\lambda_{\text{p}}\,\tau_{\text{u}}\,\sigma_{\text{abs}}(\lambda_{\text{p}})}. \tag{7.29}$$

Without considering upconversion, an inversion of 0.83 would be obtained for the above mentioned amplifier.

In order to estimate if such large inversions can be obtained in the waveguide channels of the Nd:(Gd, Lu)$_2$O$_3$ film, the saturation intensity at $\lambda_\mathrm{p} = 820\,\mathrm{nm}$ and the attainable pump intensity were compared. For the calculation of I_sat, the lifetime $\tau_\mathrm{u} = 230\,\mu\mathrm{s}$ measured in section 6.2.2 for the $^4\mathrm{F}_{3/2}$ level was used and the absorption-cross section of the film was roughly estimated to be $2 \times 10^{-20}\,\mathrm{cm}^2$, which is approximately half the value given in [For99] for a Nd:Y$_2$O$_3$ bulk crystal.[37] The calculation results in a saturation intensity of $50\,\mathrm{kW/cm}^2$. Considering the maximum incident pump power P_max of approximately 400 mW attainable with the Ti:Al$_2$O$_3$ laser used for the Nd^{3+} laser experiments and assuming a homogeneous distribution of the pump power in the approximated channel area of $5\,\mu\mathrm{m} \times 2\,\mu\mathrm{m}$, intensities of up to $4 \times 10^3\,\mathrm{kW/cm}^2$ can be obtained. Since this intensity is significantly higher than the saturation intensity, a high inversion is possible in the waveguide, even if the pump intensity is considerably reduced due to high coupling and propagation losses.

The attainable small-signal gain is thus most likely comparable to the one determined in section 7.5.1. Therefore, a doping concentration of 0.5 % is expected to be sufficiently high to compensate the waveguide losses. This concentration corresponds to a Nd^{3+} density similar to that of the Nd(1 %):YAG amplifier investigated in [Guy98] and is comparable to the optimum doping concentration given in [Dan73] for Nd:YAG. Hence, a Nd^{3+} concentration of 0.5 % was chosen for first waveguide laser experiments. However, due to the reduced impact of fluorescence quenching, which is expected for the small waveguide dimensions, higher doping concentrations may be beneficial and should be investigated in future experiments.

7.5.3 Gain Measurements

The gain experienced in a rib-channel waveguide of the 3.1 µm thick Er:(Gd, Lu)$_2$O$_3$ film was measured with a pump-probe experiment illustrated in Fig. 7.19.

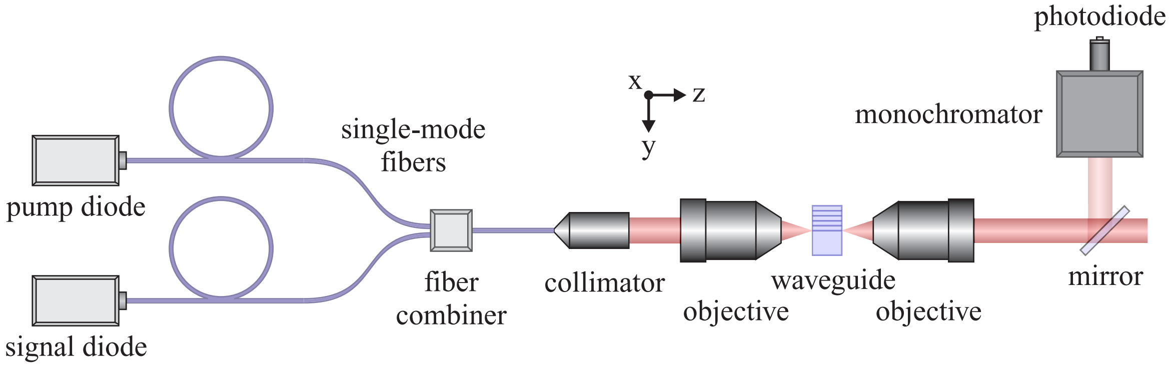

Figure 7.19: Schematic of the setup used for the gain measurments of the Er:(Gd, Lu)$_2$O$_3$ channel waveguides

---

[37] The Nd:(Gd, Lu)$_2$O$_3$ film absorption spectrum is expected to be broader than that of the Nd:Y$_2$O$_3$ bulk crystal, as observed for the fluorescence spectra (see Fig. 6.28). Therefore, the peak absorption cross-sections of the film are expected to be lower than those of the bulk crystal.

A tunable diode laser[38] ($\lambda = 1501 - 1583\,\text{nm}$) was used as signal source and a laser diode[39] at $\lambda_\text{p} = 1480\,\text{nm}$ as pump. The light from both fiber-coupled sources was combined[40] in one single-mode fiber,[41] collimated and then coupled into the waveguide channel by use of a microscope objective with a NA of 0.35. Using another objective with a NA of 0.7, the outcoupled light was collected. Signal and pump light were separated with a dichroic mirror and a monochromator. The outcoupled signal light was detected with a germanium photodiode and its intensity $I_\text{s,out}(P_\text{p})$ (in arbitrary units) was measured in dependance of the incident pump power[42] P_p for values up to $P_\text{max} \approx 200\,\text{mW}$. In order to distinguish between the signal and spontaneous fluorescence light, the former was modulated and the lock-in technique was applied.

λ (nm)	I_sat $\left(\frac{\text{kW}}{\text{cm}^2}\right)$	G'_sp (%)	G' (dB/cm)
1535.5	0.54	257	5.9
1542.0	3.51	122	1.2
1547.6	1.31	135	1.9
1555.1	1.51	140	2.1
1577.0	4.67	112	0.72

Table 7.5: Single-pass signal enhancement G'_sp measured for the 3.1 µm thick Er:$(\text{Gd,Lu})_2\text{O}_3$ waveguide as well as the signal enhancement G' in dB/cm. I_sat is the calculated saturation intensity at the corresponding signal wavelength λ.

By use of Eq. (7.30), the single-pass signal enhancement G'_sp was determined (see Tab. 7.5).

$$G'_\text{sp} = \frac{I_\text{s,out}\left(P_\text{max}\right)}{I_\text{s,out}\left(P_\text{p} = 0\right)} \tag{7.30}$$

Considering the waveguide length l of 0.7 cm, the signal enhancement G' in dB/cm is obtained as follows:

$$G' = 10 \cdot \frac{\log G'_\text{sp}}{l}\,\text{dB} \tag{7.31}$$

The signal enhancement corresponds to the gain if the absorption of the signal in the unpumped case can be neglected. Otherwise a G' higher than the gain would be measured, as pumping reduces the signal absorption.

---

[38] Lion Series of the SACHER LASERTECHNIK GROUP, Littman design

[39] 3400 Series from JDS UNIPHASE

[40] A wavelength division multiplexer (WDM) was used for that purpose.

[41] SM15 polarization maintaining FUJIKURA PANDA fibers with NA of 0.11 were used.

[42] P_p was measured between the waveguide and the coupling optics.

In order to estimate the effect of signal absorption in the unpumped case, the intensity dependent absorption coefficient $\alpha_{\mathrm{abs}}(I_{\mathrm{s}})$ at the signal wavelength $\lambda = c_0/\nu$ is determined. As in section 7.5.1, solely the $^4\mathrm{I}_{15/2}$ and $^4\mathrm{I}_{13/2}$ manifolds with populations N_{l} and N_{u} are considered. Neglecting reabsorption of spontaneously emitted photons leads to the following rate equations:

$$\frac{dN_{\mathrm{u}}}{dt} = -\frac{N_{\mathrm{u}}}{\tau_{\mathrm{u}}} + \frac{I_{\mathrm{s}}}{h\nu}\,\sigma_{\mathrm{abs}}\,N_{\mathrm{l}} - \frac{I_{\mathrm{s}}}{h\nu}\,\sigma_{\mathrm{em}}\,N_{\mathrm{u}} \tag{7.32}$$

$$N_{\mathrm{t}} = N_{\mathrm{l}} + N_{\mathrm{u}} \tag{7.33}$$

Here, τ_{u} is the lifetime of the metastable $^4\mathrm{I}_{13/2}$ level. By solving the rate equations for the steady-state, $\alpha_{\mathrm{abs}}(I_{\mathrm{s}})$ can be derived from Eq. (2.48):

$$\alpha_{\mathrm{abs}}(I_{\mathrm{s}}) = \frac{\alpha_{\mathrm{abs}}(0)}{1 + \frac{I_{\mathrm{s}}}{I_{\mathrm{sat}}}} \tag{7.34}$$

$$I_{\mathrm{sat}} = \frac{h\,\nu}{\tau_{\mathrm{u}}\,(\sigma_{\mathrm{abs}} + \sigma_{\mathrm{em}})} \tag{7.35}$$

At the saturation intensity I_{sat}, the absorption coefficient $\alpha_{\mathrm{abs}}(I_{\mathrm{s}})$ equals half the value of the small-signal absorption coefficient $\alpha_{\mathrm{abs}}(0)$. The saturation intensities for the investigated signal wavelengths were calculated with the spectroscopic parameters determined in section 6.2.1. The results are summarized in Tab. 7.5.

Incident signal powers P_{s} of at least 1.2 mW were used for the gain measurements of the 3.1 µm thick waveguide.[43] The signal intensities which would be obtained if all this power was coupled into a 5 µm wide channel of the investigated waveguide and no propagation losses occurred,[44] were simulated for the wavelengths with the highest and lowest saturation intensity.

Figure 7.20a shows the resulting intensity distribution for $\lambda = 1535.5$ nm. At this wavelength, most of the waveguide channel is significantly saturated. Less than 1.3 % of the signal power is propagating in regions where the saturation intensity is not reached, and 91.2 % is confined to areas with an intensity more than eight times higher than I_{sat}. However, the small-signal absorption coefficient at this wavelength is 2.91 cm^{-1} (12.5 dB/cm) and thus very high. Therefore, even at high intensities, absorption is not entirely negligible.

In order to estimate the signal absorption in the unpumped case, the average absorption coefficient $\bar{\alpha}_{\mathrm{abs}}$ is calculated as follows:

$$\bar{\alpha}_{\mathrm{abs}} = \frac{\int\int_{\mathrm{mode}} D(x,y)\,\alpha_{\mathrm{abs}}\left(I_{\mathrm{s}}(x,y)\right)\,I_{\mathrm{s}}(x,y)\,dx\,dy}{\int\int_{\mathrm{mode}} I_{\mathrm{s}}(x,y)\,dx\,dy} \tag{7.36}$$

$D(x,y)$ is the function introduced in section 7.3.2 in order to describes the dopant distribution. By substituting Eq. (7.34) and integrating numerically over the entire mode

---

[43] P_{s} was measured between the waveguide and the coupling optics.

[44] Coupling, absorption and parasitic losses were neglected.

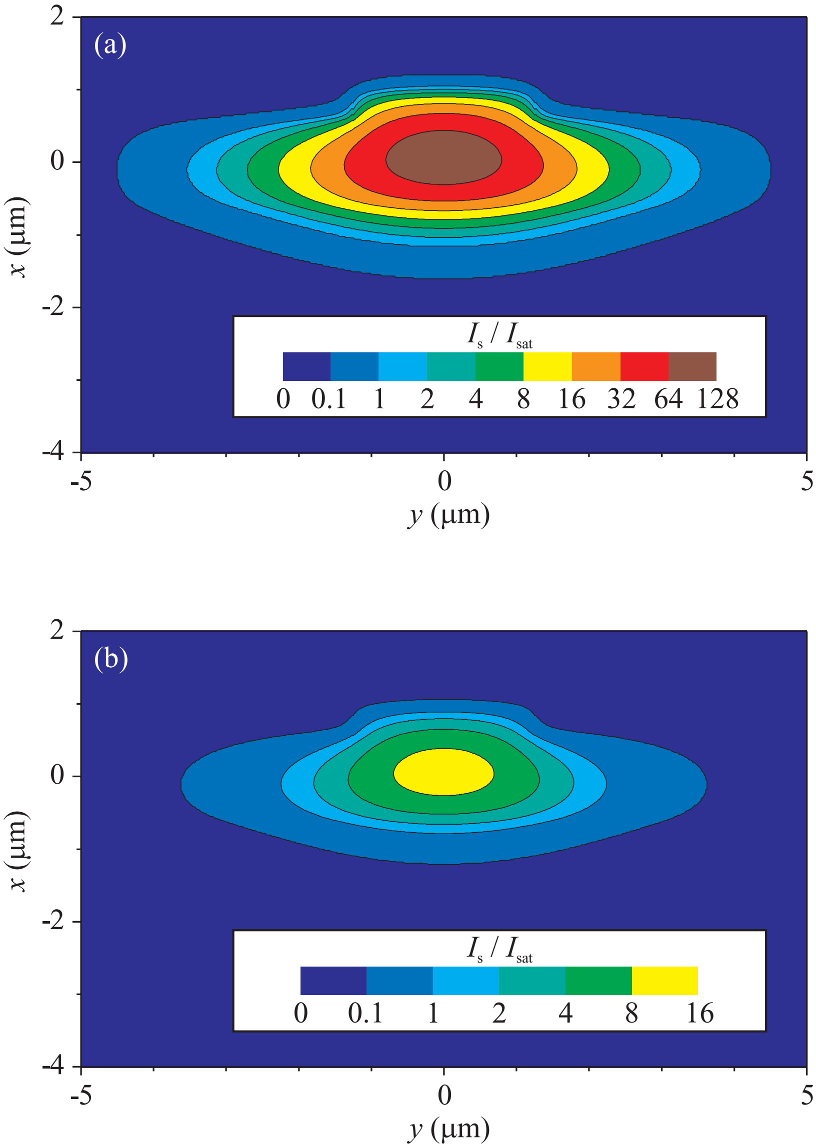

Figure 7.20: Simulated distribution of the signal intensity I_s in a 5 µm wide channel of the 3.1 µm thick Er:(Gd, Lu)$_2$O$_3$ waveguide. The simulation was performed for a signal power of 1.2 mW, TE polarization, and two wavelengths with different saturation intensities: (a) $\lambda = 1535.5$ nm, $I_\mathrm{sat} = 0.54$ kW/cm^2 and (b) $\lambda = 1577$ nm, $I_\mathrm{sat} = 4.67$ kW/cm^2

profile, an $\bar{\alpha}_{\mathrm{abs}}$ of $0.11\,\mathrm{cm}^{-1}$ (0.47 dB/cm) is obtained. This value corresponds to approximately 8 % of the measured signal enhancement G'. The actual gain G is therefore expected to be at least 8 % smaller than G'. Considering the high waveguide losses and thus reduced signal intensities, a lesser degree of saturation is obtained in most waveguide regions and G' deviates more than 8 % from the actual gain.

At $\lambda = 1577\,\mathrm{nm}$, the saturation intensity is significantly higher. Therefore, the waveguide channel is much less saturated at this wavelength (see Fig 7.20b). Nevertheless, 90.2 % of the signal propagates in regions where the saturation intensity is reached. While the channel is less saturated at $\lambda = 1577\,\mathrm{nm}$, the small-signal absorption coefficient of $0.202\,\mathrm{cm}^{-1}$ (0.87 dB/cm) is significantly smaller at this wavelength. By use of Eq. (7.36), an average absorption of $0.040\,\mathrm{cm}^{-1}$ (0.17 dB/cm) is obtained, which is 24 % of the measured signal enhancement. The actual gain at this wavelength is thus expected to be at least 24 % smaller than G'.

In the previous paragraphs, a rough estimation of the measurement error associated with signal absorption in the unpumped case was made. A more precise treatment requires the simulation of the signal-intensity evolution during propagation. However, several required parameters, such as the coupling and propagation losses, could not be determined precisely. Hence, such a simulation has not been performed.

For a qualitative comparison of the measured signal enhancement and the theoretically calculated gain, the measured values are plotted in the theoretical gain spectrum illustrated in Fig. 7.12. Since the pump power is two orders of magnitude higher than the signal power, an almost complete bleaching of the waveguide channel on the pump transition is expected. As detailed above, the signal enhancement is merely an upper limit for the actual gain. However, the measured values are still lower than the calculated ones. This is most probably due to a lesser confinement of the propagating light to the doped regions; as indicated by the comparison of the measured and simulated mode profiles in section 7.3.2, the actual confinement is most likely lower than the simulated one. Since the signal linewidth of 0.3 nm (FWHM) is smaller than the smallest linewidth in the film spectra, effects caused by the signal line shape and its overlap with the absorption and emission peaks are negligible. However, the deteriorative processes mentioned in section 7.5.2 may be responsible for the deviations from the simplified theoretical model. Nevertheless, the measurement results reproduce qualitatively the curve calculated from the spectroscopic data.

A signal enhancement of 4.8 dB/cm at $\lambda = 1535\,\mathrm{nm}$ has been determined in a similar way for a rib channel of the 1.0 µm thick Er(0.6 %):$(\mathrm{Gd},\mathrm{Lu})_2\mathrm{O}_3$ film. The smaller signal enhancement measured for this waveguide is mostly due to a lower confinement of the signal light to the doped regions. However, the measured signal enhancement for both samples is significantly higher than the value of 2.6 dB/cm measured at the same pump and signal wavelengths in a sputtered Er(0.34 %):$\mathrm{Y}_2\mathrm{O}_3$ channel waveguide [Hoe93].

The extreme losses in the channels of the 3.1 µm thick Er:$(\mathrm{Gd},\mathrm{Lu})_2\mathrm{O}_3$ sample are most probably higher than the achievable gain. In the 1.0 µm thick Er:$(\mathrm{Gd},\mathrm{Lu})_2\mathrm{O}_3$ waveguide, however, the losses are significantly lower. Hence, the 1.0 µm thick waveguide is more promising for first Er^{3+} waveguide laser experiments, although a lower gain is expected to be obtainable in this waveguide.

7.6 Summary of Waveguide Properties

The most important parameters and properties of the waveguides investigated in this chapter are summarized in Tab. 7.6.

	I[45]	II[46]	III[47]	IV[48]
Film material	$Er:Y_2O_3$	$Er:(Gd, Lu)_2O_3$	$Er:(Gd, Lu)_2O_3$	$Nd:(Gd, Lu)_2O_3$
Substrate material	α-Al_2O_3	Y_2O_3	Y_2O_3	Y_2O_3
Doping concentration (at. %)	1	0.6	0.6	0.5
Dopant density ($10^{20}\,cm^{-3}$)	2.69	1.61	1.61	1.34
Film thickness (µm)	1.0	1.0	3.1	1.9
Etch depth (nm)	-	380	710	300
Channel widths (µm)	-	2-5	2-5	2-5
Waveguide length (mm)	9.3 / 7.0	7.2	7.0	6.0
Top cladding	- / SiO_2	a-Al_2O_3	a-Al_2O_3	a-Al_2O_3
Cladding thickness (µm)	- / 1-2	1.5	1.7	1.8
Particulate density (cm^{-2})	6×10^3	8×10^4	2×10^5	2×10^5
Planar losses (dB/cm) (at $\lambda \approx 800\,nm$)	4.4 ± 0.5 1.4 ± 0.2	2.8 ± 1.3	14.8 ± 0.1	10.7 ± 0.3
Total channel losses (dB) (incl. coupling losses)	-	4.4 dB (at $\lambda = 633\,nm$)	*	6.4 dB (at $\lambda = 780\,nm$)
Signal enhancement (dB/cm) (at $\lambda = 1535\,nm$)	-	4.8	5.9	-

Table 7.6: Properties of the investigated waveguides. Since the losses of the first waveguide were measured prior and after deposition of the SiO_2 top cladding (and second end-facet polishing), two values are given for certain properties. *Light propagation in all channels of the 3.1 µm thick $Er:(Gd, Lu)_2O_3$ waveguide was severely affected by particulates.

---

[45] K41: $Er(1\%):Y_2O_3$ on α-Al_2O_3 (0001), $T = 800\,°C$, $p_{O_2} = 1.8 \times 10^{-4}$ mbar and $\nu_r = 10\,Hz$

[46] K52: $(Er_{0.006}, Gd_{0.494}, Lu_{0.500})_2O_3$ on Y_2O_3 {111}, $T = 900\,°C$, $p_{O_2} = 9 \times 10^{-3}$ mbar and $\nu_r = 1\,Hz$

[47] K59: $(Er_{0.006}, Gd_{0.494}, Lu_{0.500})_2O_3$ on Y_2O_3 {100}, $T = 900\,°C$, $p_{O_2} = 9 \times 10^{-3}$ mbar and $\nu_r = 5\,Hz$

[48] K62: $(Nd_{0.005}, Gd_{0.487}, Lu_{0.508})_2O_3$ on Y_2O_3 {100}, $T = 900\,°C$, $p_{O_2} = 9 \times 10^{-3}$ mbar and $\nu_r = 3\,Hz$

8 Waveguide Laser Experiments

The main objective of this work has been the realization of waveguide lasers[1] based on rare-earth doped sesquioxides. Due to the excellent light confinement in the investigated channel waveguides as well as spectroscopic film properties comparable to those of bulk crystals, a high optical gain is expected. As shown in section 7.5.3, measurements of the signal enhancement also indicate that a high gain can be obtained. However, the waveguides exhibit extremely high parasitic losses of several dB/cm. Nevertheless, the first waveguide laser based on rare-earth doped sesquioxides has been realized in the framework of this thesis.[2] Laser action in a monocrystalline Nd:$(\mathrm{Gd,Lu})_2\mathrm{O}_3$ rib-channel waveguide has been demonstrated. This laser as well as the laser experiments performed with Er^{3+} doped channel waveguides are described in the following sections.

8.1 Nd^{3+} Doped Waveguides

For optimum coupling and a compact waveguide design, the polished end facets of the Nd:$(\mathrm{Gd,Lu})_2\mathrm{O}_3$ waveguide were directly coated with reflective mirrors. The coatings were based on TiO_2 and SiO_2 films deposited by electron beam evaporation (EBV).[3] While a highly reflective (HR) coating for $\lambda = 1000 - 1100$ nm was applied on the incoupling facet, the transmittance T_{oc} at the outcoupling side was approximately $1-2\,\%$ for this wavelength range. Figure 8.1 shows a schematic of the waveguide laser setup.

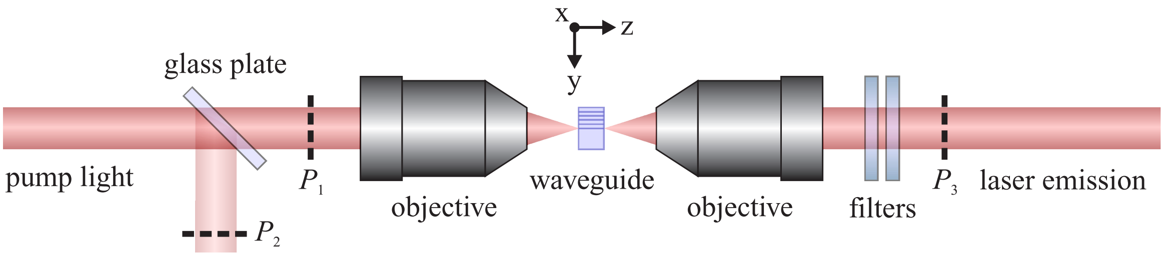

Figure 8.1: Schematic of the Nd:$(\mathrm{Gd,Lu})_2\mathrm{O}_3$ waveguide laser setup

---

[1] For a detailed description of the laser principle, see [Sve98] or another textbook of laser physics.

[2] The laser modes of the Nd:$\mathrm{Y}_2\mathrm{O}_3$ single-crystal fiber laser reported in [Sto78] are not considered to be guided modes, since merely two transverse modes were observed and more than 100 guided modes would be expected for the 2.5 mm long cylinder with a diameter of 100 µm.

[3] The EBV technique and the specific EBV setup are described in [Rab04].

A Ti:Al_2O_3 laser at $\lambda_p = 820\,\text{nm}$ was used as excitation source.[4] Using a microscope objective with a NA of 0.35, the pump light was coupled into a waveguide channel of the 1.9 µm thick and 6 mm long Nd(0.5 %):$(Gd, Lu)_2O_3$ film. The transmittance of the coated waveguide end-facets for the pump wavelength was 94 % and 84 % at the incoupling and outcoupling side, respectively. The outcoupled light was collected by use of a microscope objective with a NA of 0.7. Two dichroic mirrors, which were HR for the pump light, served as filters. Since these filters weren't aligned to couple light back into the waveguide, the pumping scheme is single pass.

Laser action with a heavily damped relaxation oscillation[5] (see Fig. 8.2) has been demonstrated. The relaxation oscillation was visualized on an oscilloscope by periodically interrupting the pump beam with a chopper and measuring the intensity variations of the outcoupled light at $\lambda = 1079\,\text{nm}$ with a silicon photodiode behind a monochromator.

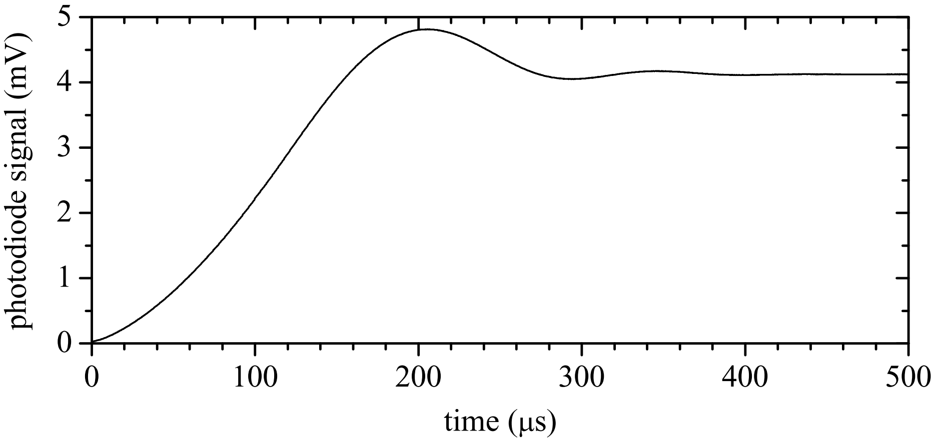

Figure 8.2: Relaxation oscillation of the Nd:$(Gd, Lu)_2O_3$ channel waveguide laser for an incident pump power of 120 mW

Figure 8.3 shows the transverse intensity profile of the outcoupled laser light, which was recorded with a CCD (charge-coupled device) camera[6]. In contrast to the intensity profiles investigated in section 7.3.2, the measured intensity profile of the laser beam is in good agreement with the simulated mode profile (see Fig. 8.4).

---

[4] According to [For99], Nd:Y_2O_3 possesses the highest $^4I_{9/2} \rightarrow {}^4F_{5/2}$ absorption cross-section at $\lambda = 820.8\,\text{nm}$. A similar optimum pump wavelength was expected for the Nd:$(Gd, Lu)_2O_3$ waveguide. Indeed, the best laser performance has been obtained for a pump wavelength λ_p of about 820 nm.

[5] For four-level lasers, the measurement of the relaxation oscillation frequency is a convenient way to determine the round trip losses [Cla89]. However, it is assumed in [Cla89] that the pump causes a negligible depletion of the ground-state population. Due to the high gain required to compensate the losses, this requirement is not fulfilled for the investigated waveguide. Hence, the above mentioned technique was not applied.

[6] PIEPER FK-7512-IQ

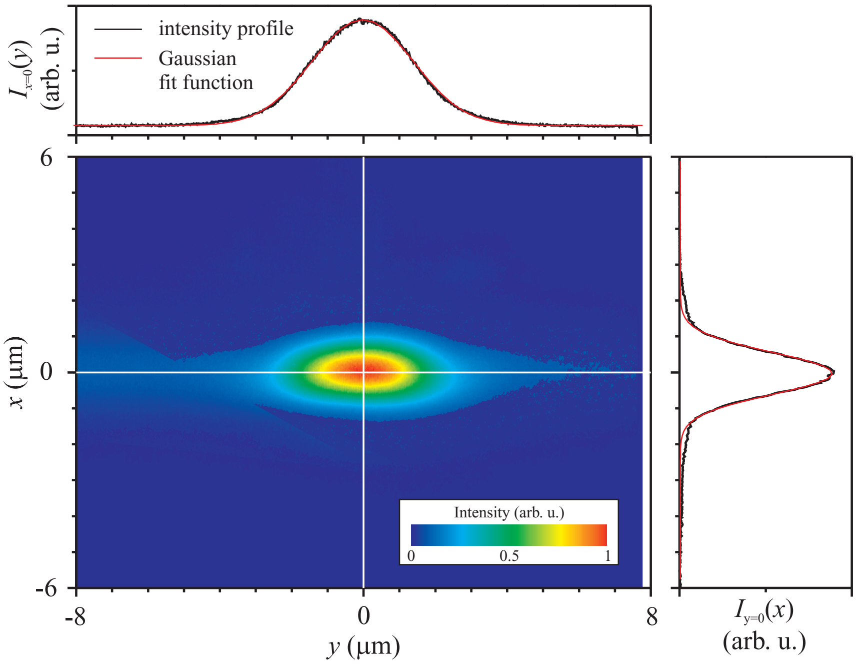

Figure 8.3: Measured transverse intensity profile (near-field image) of the laser emission outcoupled from a rib-channel of the Nd:(Gd, Lu)$_2$O$_3$ waveguide. Fitting the intensity profiles $I_{y=0}(x)$ and $I_{x=0}(y)$ with Gaussian functions, results in beam widths[7] of $\omega_x = 1.2\,\mu\text{m}$ and $\omega_y = 2.8\,\mu\text{m}$, respectively.

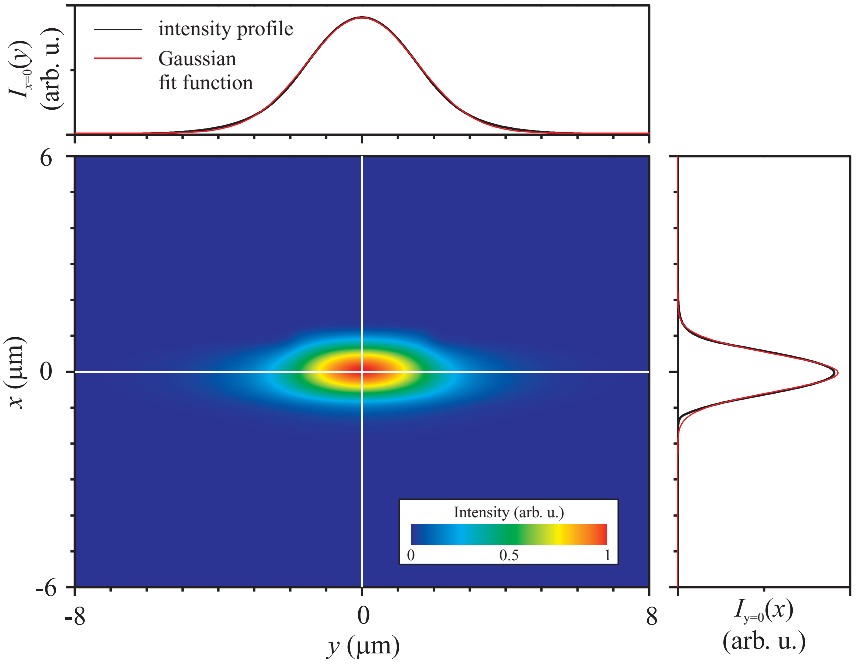

Figure 8.4: Simulated intensity distribution of the fundamental TE mode at $\lambda = 1080\,\text{nm}$ in a 4 µm wide rib-channel of the Nd:(Gd, Lu)$_2$O$_3$ waveguide. Beam widths[7] of $\omega_x = 1.0\,\mu\text{m}$ and $\omega_y = 3.1\,\mu\text{m}$ were obtained by fitting the intensity profiles $I_{y=0}(x)$ and $I_{x=0}(y)$ with Gaussian functions.

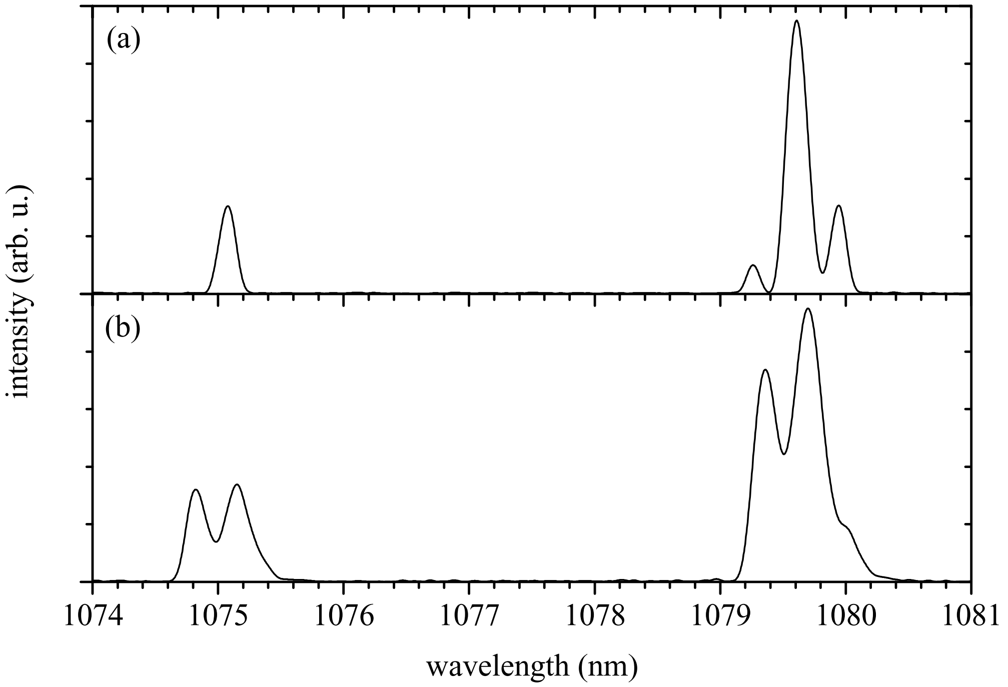

Figure 8.5: Laser spectra of the Nd:$(Gd, Lu)_2O_3$ waveguide, which have been measured using a Fourier transform spectrometer[8] with 0.1 nm resolution in the displayed spectral range. The spectra (a) and (b) have been measured for different coupling conditions.

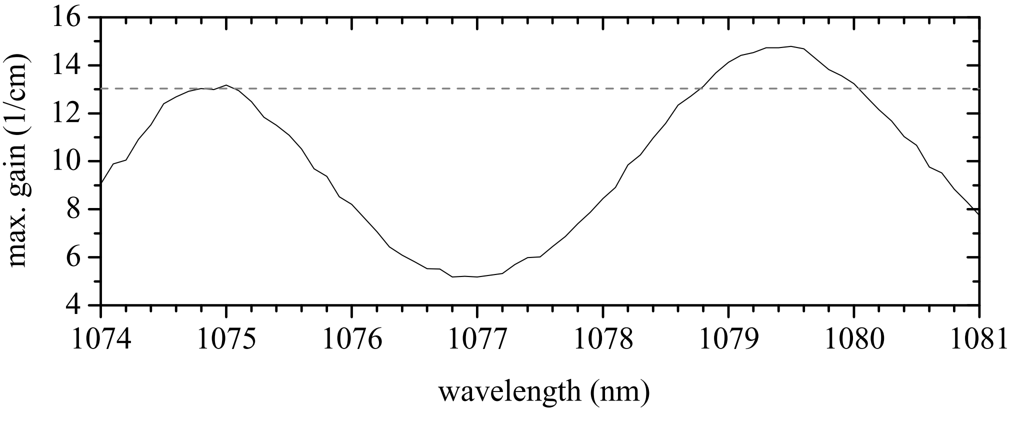

Figure 8.6: Detailed view of the Nd:$(Gd, Lu)_2O_3$ gain spectrum calculated in section 7.5.1 for an inversion $\beta = 1$. The dashed grey line indicates an upper bound for the waveguide losses.

This corroborates the theory that light coupled into the substrate, the top cladding or into the planar parts of the waveguiding film is responsible for the broad intensity profile measured in section 7.3.2. In contrast to the pump light, the laser light is generated within the waveguide and merely the rib-channel modes are supported by the cavity. Hence, the above mentioned effects, which may be responsible for the discrepancy between the simulated and measured intensity profile in section 7.3.2, are not influencing the shape of the laser mode.

The good agreement of the simulated and measured intensity profile indicates that the laser is oscillating in the fundamental transverse modes only.[9] However, the laser emitted at several wavelengths of about 1075 nm and 1080 nm simultaneously, as shown in Fig. 8.5. These wavelengths correspond to the two highest peaks in the gain spectrum calculated in section 7.5.1. A detailed view of this spectrum is given in Fig. 8.6. Since laser emission at $\lambda = 1074.8$ nm was observed, the maximum gain of 13 dB/cm obtainable at this wavelength is an upper bound for the waveguide losses. Considering the outcoupling losses and that the gain spectrum was calculated for maximum inversion (i.e. $\beta = 1$), the actual propagation losses are necessarily lower. Indeed, the measurement of the channel waveguide losses in section 7.4.2 resulted in $L < 10.7$ dB/cm (at $\lambda = 780$ nm).

The different observed laser wavelengths correspond most likely to longitudinal laser modes. For a given peak in the gain spectrum, the observed laser wavelengths are equally spaced with a distance of $0.33 - 0.35$ nm between them. This distance corresponds to a spectroscopic wavenumber of approximately 3 cm^{-1} or a frequency $\Delta\nu$ of 90 GHz. Considering the cavity to be a Fabry-Perot resonator with a length l of 6 mm, the free spectral range (FSR) $\Delta\nu_{\mathrm{fsr}} = c_0/2l'$ [Sve98] would be 13 GHz. The optical path length $l' = n_{\mathrm{eff}} \cdot l$ was calculated with the effective refractive index n_{eff} of the simulated waveguide modes, which is approximately 1.92 for all channel widths between 2 µm and 5 µm as well as both polarizations.

Since $\Delta\nu$ is approximately seven times larger than the calculated FSR, it is expected that several longitudinal modes are suppressed. This may be explained by inhomogeneities in the waveguide channel causing the individual longitudinal modes to experience different losses. It has been shown in [Pet91] that strain, growth imperfections and scattering centers resulting in the formation of weak Fabry-Perot cavities can reduce the number of longitudinal modes in a waveguide laser spectrum.

The output power $P_{\mathrm{laser,\,out}}$ of the waveguide laser in dependance of the incident pump power $P_{\mathrm{pump,\,in}}$ is plotted in Fig. 8.7. A thin glass plate served as beam splitter and the pump power was varied[10] slowly while $P_{\mathrm{pump,\,in}}$ and $P_{\mathrm{laser,\,out}}$ were recorded simultaneously. In order to derive the power P_1 of the pump light transmitted through the glass plate from the power P_2 of the reflected light, a calibration measurement was performed. $P_{\mathrm{pump,in}}$ was determined from P_1 by taking the transmittance of the incoupling objective as well as the reflectance of the coated waveguide end-facet into account. Additional coupling

---

[7] radius according to the $1/e^2$ definition

[8] BRUKER Equinox 55

[9] Both TE and TM polarization is considered.

[10] A combination of a half-wave plate and a polarizer was used for this purpose.

losses, such as those resulting from an imperfect overlap between the electric fields of the incident light and the waveguide modes, were not considered. Similarly, $P_{\mathrm{laser,out}}$ was obtained from the measured output power P_3 by considering the transmittance of the outcoupling objective and the dichroic mirrors used as filters.

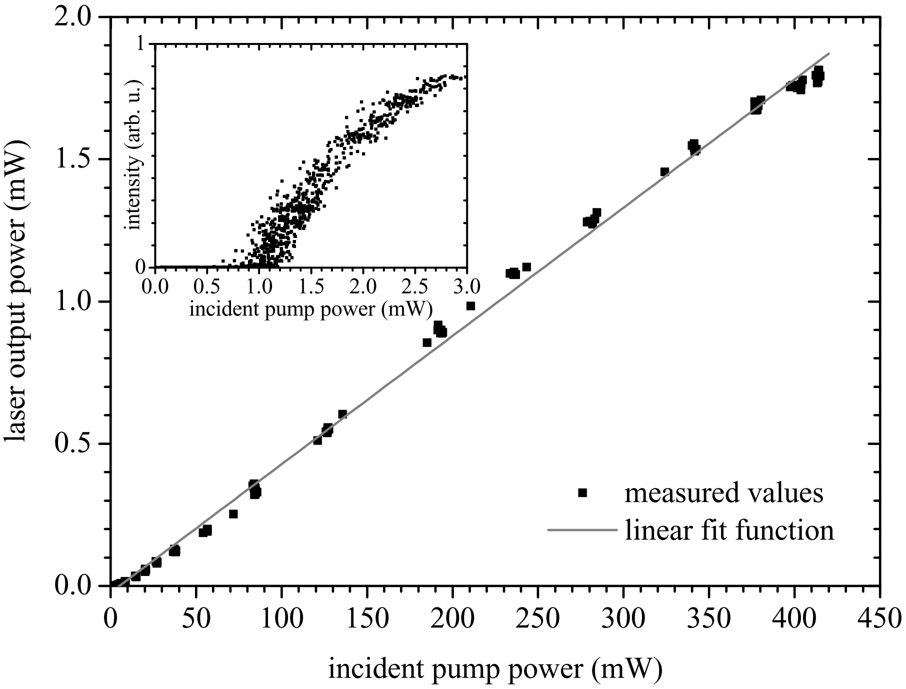

Figure 8.7: Laser output power $P_{\mathrm{laser,out}}$ plotted against the incident pump power $P_{\mathrm{pump,in}}$. A slope efficiency η_s of 0.5 % with respect to the incident pump power has been determined by fitting the measured data points with a linear function. The inset shows the measurement results for the determination of the laser threshold P_{th}, which is approximately 1 mW of incident pump power.

A maximum output power of 1.8 mW has been obtained for an incident pump power of 410 mW. The absorbed pump power could not be determined precisely, due to the unknown coupling efficiency ξ. However, an estimation of the absorbed pump power is given at the end of this section. The laser possesses a slope efficiency η_s of 0.5 %, also with respect to the incident pump power.

Due to light confinement in the extremely small waveguide dimensions and the low output coupling T_{oc}, the laser threshold is very low and could not be determined reliably from the input-output curve shown in Fig. 8.7. Therefore, instead of measuring $P_{\mathrm{laser,out}}$, the signal of a silicon photodiode behind a monochromator was measured in dependance of $P_{\mathrm{pump,in}}$ (see inset of Fig. 8.7).[11] For increased accuracy, the pump beam was periodically

---

[11] The bend of the measured data points may be explained by a saturation of the photodiode.

interrupted with a chopper and the lock-in technique was applied. The laser threshold P_{th} has been determined to be approximately 1 mW of incident pump power, which is extremely low considering the high losses. For comparison, the threshold power of the planar Nd:$Gd_3Ga_5O_{12}$ waveguide laser reported in [Gil96], which possessed an output coupling of less than 1 % and comparably high losses of 6 dB/cm, was 91 mW with respect to the pump light coupled into the waveguide. However, slope efficiencies and laser thresholds are usually given with respect to the absorbed pump power. Hence, in order to compare the properties of the demonstrated Nd:$(\mathrm{Gd},\mathrm{Lu})_2\mathrm{O}_3$ waveguide laser to those of other neodymium doped lasers, the absorbed pump power is estimated.

For this, two transmission measurements were performed subsequently to the laser experiments. The total waveguide losses at a wavelength with negligible absorption (see section 7.4.2) and those at the pump wavelength were determined. Figure 8.8 shows the results of the transmission measurement performed at $\lambda_{\mathrm{p}} = 820\,\mathrm{nm}$.

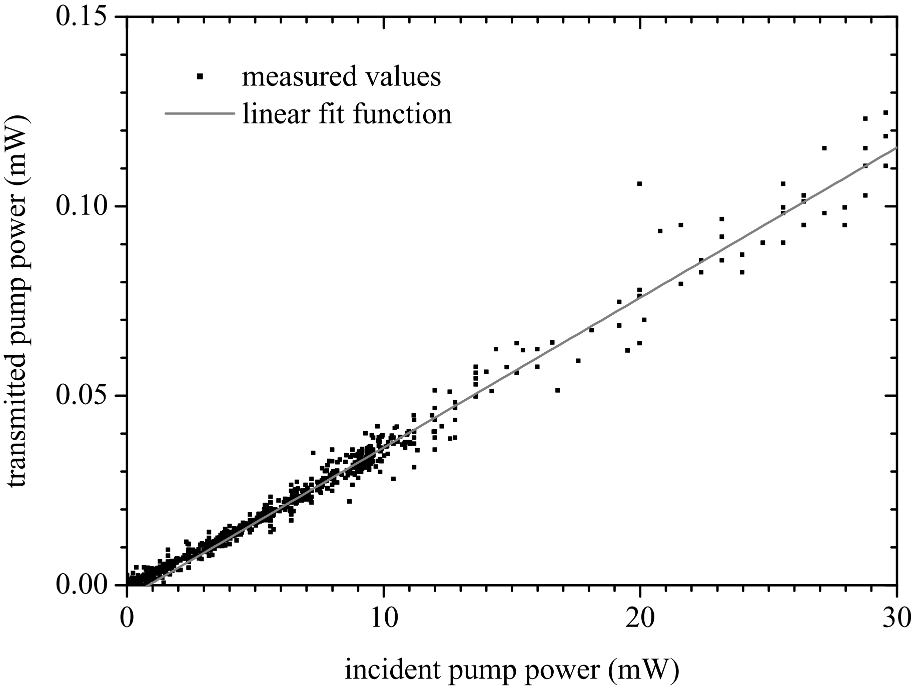

Figure 8.8: Transmission measurement for the determination of the pump absorption. The power of the transmitted pump light at $\lambda_{\mathrm{p}} = 820\,\mathrm{nm}$ is plotted against the incident power.

The incident pump power $P_{\mathrm{pump,\,in}}$ was determined in a similar way as described above. However, the dichroic mirrors were replaced by a filter, which was HR for the waveguide laser emission and possessed a high transmittance at the pump wavelength. For the determination of the transmitted pump power, the measured power P_3 was corrected by considering the transmittances of the waveguide end-facet, the outcoupling objective and the dichroic filter.

Due to fixed populations[12] at pump powers equal to or higher than the laser threshold, the relative pump transmission in Fig. 8.8 shows a linear behavior. Fitting the measured values with a linear function for incident pump powers of at least 5 mW, which is significantly above the laser threshold, a pump transmission of 0.4 % is obtained from the slope of the resulting line. According to Eq. (7.18), this value corresponds to total losses L_{total} of 24 dB. Since the reflection losses at the end-facets have already been deducted, L_{total} includes only the absorption losses L_{abs}, the parasitic losses L_{p} and the losses L_{ξ} due to an imperfect overlap ξ between the electric fields of the incident light and the waveguide modes:

$$L_{\mathrm{total}} = L_{\mathrm{abs}} + L_{\mathrm{p}} + L_{\xi} \tag{8.1}$$

The measurement at $\lambda = 780\,\mathrm{nm}$ resulted in total losses of 10.7 dB. Considering the small wavelength difference between 780 nm and 820 nm, it is assumed that L_{p} as well as L_{ξ} are similar in both measurements. Thus, by subtracting the total losses measured for the two wavelengths and neglecting the marginal absorption at $\lambda = 780\,\mathrm{nm}$, the absorption losses L_{abs} at the pump wavelength are determined to be 13.3 dB. This value corresponds to a transmission T_{abs} of 4.7 %. Thus, 95.3 % of the pump light which is not lost due to coupling or parasitic losses is absorbed. However, due to the high remaining losses of 10.7 dB, the percentage of absorbed power with respect to the incident light is expected to be much smaller.[13] Since the parasitic losses L_{p} are often negligible, the absorbed pump powers given in most publications do not take these losses into account. Hence, in order to compare the performance of the demonstrated Nd:$(\mathrm{Gd,Lu})_2\mathrm{O}_3$ waveguide laser with those of other reported Nd^{3+} lasers, the absorbed pump power $P_{\mathrm{pump,\,abs}}$ is also calculated without taking the parasitic losses into account:

$$P_{\mathrm{pump,\,abs}} = \xi \cdot (1 - T_{\mathrm{abs}}) \cdot P_{\mathrm{pump,\,in}} \tag{8.2}$$

Thus, merely an upper limit for the absorbed pump power is determined. In section 7.4.2, the coupling efficiency ξ was roughly estimated to be in between 40 % and 70 %. Considering the pump transmission T_{abs} of 4.7 %, slope efficiencies between 0.7 % and 1.3 % as well as laser thresholds between 0.4 mW and 0.7 mW are obtained, all values with respect to the absorbed pump power as defined in Eq. (8.2).

Due to the low output coupling T_{oc} of approximately 1 − 2 % and the high waveguide losses of several dB/cm, the slope efficiency is extremely low. The threshold pump power is, however, significantly lower than that obtained in [For99] for various Nd^{3+} doped sesquioxide bulk-lasers emitting at comparable wavelengths λ_{l} (see Tab. 8.1). However,

---

[12] During cw laser-operation, the inversion is usually time-invariant. However, thermal effects changing the spectroscopic properties, the beam shape and the waveguide losses, can introduce intensity dependent population variations.

[13] In order to determine the actually absorbed pump power, a simulation of the pump-intensity evolution during propagation within the waveguide would be required. However, several important parameters, such as the coupling and propagation losses, could not be determined precisely. Hence, such a simulation has not been performed.

the $Nd:Y_2O_3$ single-crystal fiber laser reported in [Sto78] featured a comparably low laser threshold of 0.57 mW of absorbed pump power.

Material	λ_p (nm)	λ_l (nm)	T_{oc} (%)	η_s (%)	$P_{th,abs}$ (mW)
$Nd(1.4\,\%):Y_2O_3$	819.5	1075	3	5	65
$Nd(0.8\,\%):Lu_2O_3$	821.5	1076	1	39	50
$Nd(0.13\,\%):Sc_2O_3$	825.5	1082, 1087	3	58	5

Table 8.1: Properties of several Nd^{3+} doped sesquioxide bulk-lasers demonstrated in [For99]. All lasers were operated at room temperature upon cw-excitation with a $Ti:Al_2O_3$ laser. The slope efficiencies η_s and laser thresholds $P_{th,abs}$ are with respect to the absorbed pump power.

In spite of the extremely high parasitic losses, the threshold pump power of the demonstrated device is among the lowest ones reported for Nd^{3+} doped channel waveguide lasers, such as the 0.54 mW of absorbed pump power achieved for an ion-implanted Nd:YAG waveguide channel [Fie91].

While the slope efficiency is very low, higher values are expected when increasing the output coupling above 2 %. The optimum output coupling and doping concentration for maximum output power is yet to be determined. However, in order to significantly increase the overall laser performance, a reduction of the extremely high waveguide losses is essential.

8.2 Er^{3+} Doped Waveguides

Channel waveguide laser experiments were also performed with the 1.0 µm thick $Er(0.6\,\%):(Gd,Lu)_2O_3$ waveguide. This waveguide was chosen due to its significantly lower losses in comparison to the 3.1 µm thick one (see Tab. 7.6). By use of EBV, reflective mirrors were deposited on both end-facets of the waveguide. In order to obtain a high reflectance at the potential laser wavelength of 1535 nm and a reasonable transmittance at the pump wavelength of 1480 nm, a steep edge filter was required at the incoupling side.

While the realization of sufficiently steep edge filters is possible by use of ion beam sputtering (IBS), some problems are encountered using EBV as deposition technique. The coatings possess a high porosity and are thus sensitive to moisture [Rab04].[14] Hence, the refractive index and the thickness of the dielectric layers change after deposition, and the resulting shift of the transmission spectrum has to be pre-estimated. Since the extent of the spectral shift could not be exactly predicted, a reflectance of merely 90 % at $\lambda = 1535$ nm was obtained for the incoupling end-facet of the 1.0 µm thick waveguide.

---

[14] By use of ion assisted deposition (IAD) layers with higher density can be obtained [Mar83].

Furthermore, due to the large number of required layers, the coatings were spalling shortly after deposition.

Due to the damaged and insufficiently reflective coatings, the laser experiments with the otherwise promising 1.0 µm thick Er:$(Gd, Lu)_2O_3$ waveguide were not successful. The coatings were not removed for another deposition attempt, since the required polishing process would have resulted in an extremely short waveguide.

However, another Er(0.6 %):$(Gd, Lu)_2O_3$ waveguide[15] was fabricated for subsequent laser experiments. This waveguide possessed a film thickness of 2.0 µm, channel widths of 2 – 5 µm, an etch depth of 690 nm and a 1.7 µm thick a-Al_2O_3 top cladding. The waveguide length after polishing was 6.9 mm. For this waveguide, the deposition of stable reflective coatings by EBV was successful; introducing a $\lambda/2$ layer, a band-pass filter with a relatively sharp transmission peak at the pump wavelength was realized with a reduced number of layers. While a transmittance of approximately 70 % at $\lambda_\mathrm{p} = 1480$ nm and a reflectance of about 98 – 99 % at $\lambda = 1535$ nm were obtained for the incoupling end-facet, the reflectance at the outcoupling side was approximately 98 – 99 % for both wavelengths.

The laser setup was comparable to the one used for the gain measurements (see Fig. 7.19). However, neither a signal diode nor a fiber combiner were employed. Instead, the pump diode[16] was connected to the collimator by use of its pigtailed single-mode fiber. Although several waveguide channels were investigated and incident pump powers up to 170 mW were used,[17] laser action has not been observed.

While the waveguide losses have yet to be measured, a particulate density of approximately $1 \times 10^5 - 2 \times 10^5\,\mathrm{cm}^{-2}$ has been determined for the above mentioned waveguide. Since the particulate density is comparable to those of the other investigated $(Gd, Lu)_2O_3$ waveguides (see Tab. 7.6), parasitic losses in the order of several dB/cm are expected for this waveguide as well.

Lower losses or a higher gain are required for the realization of an Er^{3+} doped channel waveguide laser. In order to increase the gain, higher doping concentrations should be considered, although the detrimental effects (see section 7.5.2) have to be taken into account. However, even with higher doping concentrations, a reduction of the parasitic losses is crucial for the realization of efficient waveguide lasers. Potential solutions are thus proposed in the outlook of this thesis.

---

[15] K64: $(Er_{0.006}, Gd_{0.494}, Lu_{0.500})_2O_3$ on Y_2O_3 {100}, $T = 900\,°C$, $p_{O_2} = 9 \times 10^{-3}$ mbar and $\nu_\mathrm{r} = 3$ Hz

[16] 3400 Series from JDS Uniphase

[17] While the transmittance of the incoupling objective and the waveguide end-facet are taken into account, the coupling efficiency ξ is not considered.

9 Conclusion

9.1 Summary of Results

The realization of integrated optical devices based on rare-earth (RE) doped sesquioxides is very promising. Since integrated optical elements can be fabricated by structuring thin waveguiding films, the preparation of such films using pulsed laser deposition (PLD) and the optimization of the deposition process have been the first objectives of this work. A summary of the progress in film deposition is given in the first part of this section.

The main objective of this work has been the realization of rib-channel waveguide lasers based on the fabricated sesquioxide films. Hence, the films were structured and waveguide experiments were performed. These experiments, resulting in the demonstration of the first RE doped sesquioxide waveguide laser, are described in the second part of this section.

Fabrication and Characterization of RE Doped Sesquioxide Films

Several different types of film-substrate combinations were investigated regarding their suitability for the fabrication of waveguiding films. The main focus was on the realization of epitaxial growth and the preparation of films with a high crystallinity featuring sharp emission peaks and high peak cross sections. Film growth was monitored by use of reflection high-energy electron diffraction (RHEED) and the structure of the films was characterized using X-Ray diffraction (XRD) and atomic force microscopy (AFM). The fluorescence lifetimes of the Nd^{3+} and Er^{3+} doped films were measured and their absorption and emission cross-sections were determined.

Epitaxial growth could not be realized for the deposition of RE doped Y_2O_3 on (0001) oriented α-Al_2O_3 substrates. This is due to the formation of an amorphous interface, which has been identified at the beginning of film deposition. Nevertheless, a preferred growth in <111> direction was observed, resulting in highly-textured polycrystalline films with spectroscopic properties similar to those of correspondingly doped bulk crystals. Thus, this material system is promising for the fabrication of integrated optical devices, although epitaxial film growth has not been obtained. Therefore, the influence of several deposition parameters on the crystallinity and optical quality of the films was investigated. For a substrate temperature of 800 °C and oxygen pressures between 1.8×10^{-4} mbar and 7×10^{-3} mbar, the 1 µm thick films consisted of slightly tilted monocrystalline regions with dimensions of 50 to 60 nm perpendicular to the sample surface. Nevertheless, the films possessed relatively flat surfaces with root-mean-square (RMS) roughnesses between 2 nm and 4 nm.

While the spectroscopic properties of the polycrystalline Y_2O_3 films deposited on sapphire substrates are promising, a layer-by-layer growth mode and monocrystalline films may be advantageous regarding optical quality and thermal conductivity. In order to obtain such a growth mode with the above mentioned materials, the formation of the amorphous interface at the beginning of film growth should be prevented. This may be achieved by deposition of special buffer layers. However, the lattice mismatch may still be too high for layer-by-layer growth. Hence, in the framework of this thesis, other film-substrate combinations were investigated in order to realize such a growth mode.

For this, the growth of RE doped Sc_2O_3 on {100} oriented Y_2O_3 substrates was investigated. In contrast to the films deposited on sapphire, no indications of an amorphous interface have been observed. Indeed, growth in <100> direction, which was supported by the crystal structure of the substrate, has been realized. However, due to the extremely high lattice mismatch of -7.57 %, the growth mode was mostly three-dimensional (3D) and cracks were located all over the film. A lower lattice mismatch is thus required. Therefore, the growth of lattice matched films was investigated. These films were fabricated by mixing sesquioxides with different lattice constants.

Epitaxial growth of RE doped $(\mathrm{Gd, Lu})_2O_3$ on {100} oriented Y_2O_3 substrates has been realized and monocrystalline films with thicknesses up to 3 µm have been fabricated. Up to a film thickness of approximately 100 nm, two-dimensional (2D) layer-by-layer growth was observed. Afterwards, the growth mode changed to multilevel 2D growth. The surface structure of the $1-3$ µm thick films consisted of nearly atomically flat terraces and step edges with typical heights of a single monolayer. Therefore, remarkably low surface roughnesses as low as 0.7 nm (RMS) have been achieved. While epitaxial 2D growth by lattice matching is well established for the deposition of semiconductor materials, it is a remarkable achievement for dielectric oxides.

As a result of the lattice matching, the peak positions in the emission spectra of the Nd^{3+} and Er^{3+} doped $(\mathrm{Gd, Lu})_2O_3$ films are nearly identical to those measured for correspondingly doped Y_2O_3 bulk crystals. However, a spectral broadening of the emission peaks, resulting in lower peak emission cross-sections, has been observed. Nevertheless, emission cross-section of $2.7 \times 10^{-20}\,\mathrm{cm}^2$ and $1.8 \times 10^{-20}\,\mathrm{cm}^2$ have been measured for the $\mathrm{Nd{:}(Gd, Lu)_2O_3}$ and $\mathrm{Er{:}(Gd, Lu)_2O_3}$ films at the potential laser wavelengths of 1079 nm and 1535 nm, respectively. These cross sections are only 32 % and 11 % lower than the respective cross sections determined for $\mathrm{Nd{:}Y_2O_3}$ and $\mathrm{Er{:}Y_2O_3}$ bulk crystals. Since the fluorescence lifetimes of the lattice matched films are also comparable to those of correspondingly doped Y_2O_3 bulk crystals, monocrystalline RE doped $(\mathrm{Gd, Lu})_2O_3$ films are very promising for the realization of integrated optical devices.

Waveguide and Laser Experiments

For the fabrication of practical integrated optical devices and efficient waveguide lasers, a high optical quality of the employed materials is required. However, the investigated films were severely affected by parasitic particulates, which are usually generated during PLD. Typical particulate densities between $10^3\,\mathrm{cm}^{-2}$ and $10^5\,\mathrm{cm}^{-2}$ were measured for the deposited films. Scattering at these particulates increases the losses light experiences during propagation within a waveguide. In order to determine these parasitic waveguide losses, an improved loss-measurement method has been devised. Using this technique, the effect of several film properties on the waveguide losses was examined. For instance, the expected reduction of the propagation losses by deposition of a top cladding could be confirmed. Most of the planar waveguides though exhibited extremely high parasitic losses up to 14.8 dB/cm at wavelengths of approximately 800 nm.

In order to realize rib-channel waveguide lasers, several films were structured by Ar-ion etching and their end-facets were polished. For laser experiments, reflective coatings were applied to the end-facets of the waveguides. Since an extremely poor surface quality of the end-facets was obtained by polishing the waveguides deposited on α-$\mathrm{Al_2O_3}$ substrates, monocrystalline $(\mathrm{Gd,Lu})_2\mathrm{O}_3$ waveguides deposited on $\mathrm{Y_2O_3}$ were chosen for first laser experiments. However, the polishing process for sesquioxide-on-sapphire waveguides has been improved, and the employment of such waveguides for future experiments should be possible.

Due to the high pump intensities obtainable in a waveguide channel, a high optical gain was expected. Indeed, a signal enhancement of 5.9 dB/cm at a wavelength of 1536 nm has been measured for an Er(0.6 %):$(\mathrm{Gd,Lu})_2\mathrm{O}_3$ waveguide upon in-band pumping at 1480 nm. However, the gain in the Er:$(\mathrm{Gd,Lu})_2\mathrm{O}_3$ waveguides was not sufficient to compensate the high losses and laser action has not been realized in the Er^{3+} doped waveguides. For an Er(0.2 %):$\mathrm{Sc_2O_3}$ bulk crystal though, laser emission at 1.58 µm has been demonstrated, both for pumping at 975 nm and for in-band pumping at 1536 nm.

A significantly higher gain than for the Er:$(\mathrm{Gd,Lu})_2\mathrm{O}_3$ waveguides was expected for Nd^{3+} doped ones. Therefore, the laser experiments performed with a monocrystalline Nd(0.5 %):$(\mathrm{Gd,Lu})_2\mathrm{O}_3$ rib-channel waveguide were successful. Continuous-wave laser emission at wavelengths of approximately 1075 nm and 1080 nm has been observed upon pumping at 820 nm. Due to light confinement in the extremely small waveguide dimensions and the low output coupling of $1-2\,\%$, the laser threshold was as low as 1 mW of incident pump power. However, a slope efficiency of merely 0.5 % with respect to the incident pump power has been achieved. Hence, the maximum output power for an incident pump power of 410 mW was only 1.8 mW. In order to obtain higher slope efficiencies and output powers, increased output couplings should be investigated. Furthermore, the laser performance can most likely be significantly increased by reducing the waveguide losses. Nevertheless, laser action in a rare-earth doped sesquioxide waveguide has been demonstrated for the first time.

9.2 Outlook

A reduction of the extremely high waveguide losses is crucial for efficient laser operation. Particulate prevention is a critical factor for the fabrication of low loss waveguides by PLD. Several possible solutions, such as non-thermal ablation with femtosecond pulses or a deflection of particulates by gas pulses, are proposed in [Bar00]. Another potential solution is the use of a velocity filter based on a rotating vane [Bar69]. The implementation of such a device in the employed PLD setup is currently in progress. According to [Bar00], the fabrication of thicker waveguides might also be beneficial in order to reduce the parasitic losses. The thicker waveguides investigated in the framework of this thesis, however, exhibited higher losses than the thinner ones. The influence of film thickness on the parasitic losses should thus be further investigated

Since the measured signal enhancement and the propagation losses in the $Er{:}(Gd,Lu)_2O_3$ channel waveguides are of the same order of magnitude, it is very probable that laser action in Er^{3+} doped sesquioxide waveguides can be realized with a reduction of the parasitic losses or an increase of the doping concentration. The investigation of other active ions is also very promising. Indeed, shortly after demonstration of the Nd^{3+} doped waveguide laser, an $Yb{:}(Gd,Lu)_2O_3$ waveguide laser has been realized as well [Kue09c].

While the demonstrated channel waveguide lasers with coated end-facets are not yet integrated optical devices, they indicate the feasibility of such devices with the investigated materials. As pointed out in the introduction, a high frequency stability is required for certain applications. Hence, the fabrication of integrated ring-lasers or lasers with extremely short cavity lengths is promising. The latter could be realized by creating distributed Bragg reflectors (DBR) within the waveguiding structures.

Generally, the degree of possible miniaturization depends on the refractive index difference between film and substrate material. While the refractive index difference between the $(Gd,Lu)_2O_3$ films and the Y_2O_3 substrates is merely 0.04 at the telecommunication wavelength of 1.55 µm, a significantly higher refractive index difference of 0.14 is obtained for Y_2O_3 on α-Al_2O_3. Although polycrystalline, these waveguides possess slightly higher peak cross-sections and slightly smaller linewidths in their emission spectra. Furthermore, sapphire substrates are commercially available. Due to the recent improvements of the polishing process, further investigations of sesquioxide-on-sapphire waveguides are with good prospects.

PLD is a flexible method for the deposition of complex materials. However, it might not be suitable for a large scale production. Other deposition techniques should thus also be considered. Nevertheless, for the limited device quantities required in highly specialized fields of application such as space communications, the fabrication capacities attainable with PLD are most probably sufficient.

Integrated optics are well established in many fields of application [Kar91, Sal91] such as data transmission, information processing as well as sensor and measurement technology. Since rare-earth doped sesquioxides are excellent laser materials, their employment in a multitude of present and future integrated optical applications is promising.

A References for Table 3.2

	Sc_2O_3	Y_2O_3	Lu_2O_3	Gd_2O_3	α-Al_2O_3
Space group	[Gme74]	[Gme74]	[Gme74]	[Gme74]	[Web82]
Lattice constants	[Gme74]	[Gme74]	[Gme74]	[Hei05]	[Lut90]
Density	[Gme74]	[Gme74]	[Gme74]	[Gme74]	[Web82]
Density of RE cations	calc.	calc.	calc.	calc.	-
Hardness (Mohs)	[Pet09]	[Pet09]	[Pet09]	[Gme74]	[Bae04]
Melting temperature	[Gme74]	[Gme74]	[Gme74]	[Gme74]	[Web82]
Thermal conductivity	[Pet09]	[Pet09]	[Pet09]		[Bur02]
Thermal expansion	[Gme74]	[Gme74]	[Gme74]	[Gme74]	[Web82]
Maximum phonon energy	[Mix99]	[Mix99]	[Mix99]	[McD66]	[Mix99]
Transparency range	[Pet09]	[Web82]	[Pet09]		[Web82]

Table A.1: References for the values given in Tab. 3.2. The densities of RE cations have been calculated from the lattice constants.

Bibliography

[And96] S. Andrieu and P. Fréchard
What information can be obtained by RHEED applied on polycrystalline films?
Surface Science **360**, 289–296 (1996).

[ATT09] *AT&T, NEC, and Corning Researchers Complete another Record-Breaking Fiber Capacity Test*
AT&T Press Release (May 2009).

[Auz07] F. Auzel and G. Baldacchini
Photon trapping in ruby and lanthanide-doped materials: Recollections and revival
Journal of Luminescence **125**, 25–30 (2007).

[Bae04] S. Bär
Crystalline Rare-Earth-Doped Sesquioxide PLD-Films on α-Alumina - Preparation and Characterization
Ph.D. thesis, Universität Hamburg (2004).

[Bar69] W. P. Barr
The production of low scattering dielectric mirrors using rotating vane particle filtration
Journal of Physics E **2**, 1112–1114 (1969).

[Bar00] S. J. Barrington, T. Bhutta, D. P. Shepherd and R. W. Eason
The effect of particulate density on performance of $Nd{:}Gd_3Ga_5O_{12}$ *waveguide lasers grown by pulsed laser deposition*
Optics Communications **185**, 145–152 (2000).

[Bau58] E. Bauer
Phänomenologische Theorie der Kristallabscheidung an Oberflächen. I
Zeitschrift für Kristallographie **110**, 372–394 (1958).

[Bec88] C. H. Becker and J. B. Pallix
Laser ablation of bulk $YBa_2Cu_3O_{7-\delta}$ *and cluster emission*
Journal of Applied Physics **64**, 5152–5156 (1988).

[Bin86] G. Binnig and C. F. Quate
Atomic Force Microscope
Physical Review Letters **56** (9), 930–933 (1986).

[Bra99] W. Braun
Applied RHEED
Springer Tracts in Modern Physics, Springer (1999).

[Bra03] B. Bransden and C. Joachain
Physics of Atoms and Molecules
Prentice Hall, second edition (2003).

[Bra07] J. D. B. Bradley, F. Ay, K. Wörhoff and M. Pollnau
Fabrication of low-loss channel waveguides in Al_2O_3 *and* Y_2O_3 *layers by inductively coupled plasma reactive ion etching*
Applied Physics B **89**, 311–318 (2007).

[Bur02] P. Burmester
Optisch aktive, kristalline, Selten Erd-dotierte Y_2O_3*-PLD-Schichten auf* α-Al_2O_3
Ph.D. thesis, Universität Hamburg (2002).

[Cha71] I. F. Chang and S. S. Mitra
Long Wavelength Optical Phonons in Mixed Crystals
Advances in Physics **20** (85), 359–404 (1971).

[Che05] S. Chen, Q. Yan, Q. Xu, Z. Fan and J. Liu
Optical waveguide propagation loss measurement using multiple reflections method
Optics Communications **256**, 68–72 (2005).

[Chr94] D. B. Chrisey and G. K. Hubler
Pulsed Laser Deposition of Thin Films
John Wiley & Sons (1994).

[Cla89] W. A. Clarkson and D. C. Hanna
Effects of transverse-mode profile on slope efficiency and relaxation oscillations in a longitudinally-pumped laser
Journal of Modern Optics **36** (4), 483–498 (1989).

[Cos08] G. A. Costa et al.
Phase stability study of the pseudobinary system Gd_2O_3-Nd_2O_3 $(T \leq 1350°C)$
Journal of Thermal Analysis and Calorimetry **92** (1), 101–104 (2008).

[Cul01] B. D. Cullity and S. R. Stock
Elements of X-Ray Diffraction
Prentice Hall, third edition (2001).

[Dan73] H. G. Danielmeyer, M. Blätte and P. Balmer
Fluorescence Quenching in Nd:YAG
Applied Physics A **1** (5), 269–274 (1973).

[Dav96] K. M. Davis, K. Miura, N. Sugimoto and K. Hirao
Writing waveguides in glass with a femtosecond laser
Optics Letters **21** (21), 1729–1731 (1996).

[Dev54] J. C. De Vos
A New Determination of the Emissivity of Tungsten Ribbon
Physica **20**, 690–714 (1954).

[Dic01] B.-M. Dicks
Optische Verstärker bei 1.06 μm für die Weltraumkommunikation
Ph.D. thesis, Universität Hamburg (2001).

[Die68] G. H. Dieke
Spectra and Energy Levels of Rare Earth Ions in Crystals
Interscience Publishers, Wiley & Sons (1968).

[Die92] J. Dieleman, E. van de Riet and J. C. S. Kools
Laser Ablation Deposition: Mechanism and Application
Japanese Journal of Applied Physics **31**, 1964–1971 (1992).

[Din94] M. Dinand and W. Sohler
Theoretical Modeling of Optical Amplification in Er-Doped Ti:LiNbO$_3$ *Waveguides*
IEEE Journal of Quantum Electronics **30** (5), 1267–1276 (1994).

[Dye91] R. C. Dye, R. E. Muenchausen and N. S. Nogar
Laser ablation of Y_2O_3 *in an oxygen atmosphere*
Chemical Physics Letters **181** (6), 531–536 (1991).

[Eas07] R. Eason
Pulsed Laser Deposition of Thin Films
John Wiley & Sons (2007).

[Ehl05] S. Ehlert
Herstellung und Charakterisierung ultradünner PLD-Sesquioxidschichten auf Quarz
Diploma thesis, Universität Hamburg (2005).

[Ein16] A. Einstein
Strahlungs-Emission und -Absorption nach der Quantentheorie
Deutsche physikalische Gesellschaft, Verhandlungen, XVIII, 318-323 (1916).

[Erl00] R. Erlandsson and P. Apell
Progress in scanning probe microscopy: High resolution force microscopy and spectroscopy
Current Science **78** (12), 1445–1457 (2000).

[Fec07a] M. Fechner, A. Kahn, K. Petermann, H. Scheife and G. Huber
Continuous-wave laser action of an Er:Sc_2O_3 *bulk crystal at 1.58 μm*
CLEO/Europe and IQEC 2007 Conference Digest, (Optical Society of America, 2007), paper CA8_5.

[Fec07b] M. Fechner
Spektroskopie und Laserparameter Er- und Er, Yb-dotierter Sesquioxide bei 1,55 μm
Diploma thesis, Universität Hamburg (2007).

[Fec08] M. Fechner, R. Peters, A. Kahn, K. Petermann, E. Heumann and G. Huber
Efficient in-band-pumped Er:Sc_2O_3-laser at 1.58 μm
Conference on Lasers and Electro-Optics/Quantum Electronics and Laser Science Conference and Photonic Applications Systems Technologies, OSA Technical Digest (CD) (Optical Society of America, 2008), paper CTuAA3.

[Fie91] S. J. Field et al.
Low threshold ion-implanted Nd:YAG channel waveguide laser
Electronics Letters **27** (25), 2375–2376 (1991).

[For99] L. Fornasiero
Nd^{3+}- und Tm^{3+}-dotierte Sesquioxide
Ph.D. thesis, Universität Hamburg (1999).

[Fra49] F. C. Frank and J. H. van der Merwe
One-Dimensional Dislocations. I & II.
Proc. Royal Soc. London. Series A **198** (1053), 205–225 (1949).

[Gab00] R. J. Gaboriaud, F. Pailloux, P. Guerin and F. Paumier
Yttrium oxide thin films, Y_2O_3, grown by ion beam sputtering on Si
J. Phys. D: Appl. Phys. **33**, 2884–2889 (2000).

[Gil96] D. S. Gill, A. A. Anderson, R. W. Eason, T. J. Warburton and D. P. Shepherd
Laser operation of an Nd:$Gd_3Ga_5O_{12}$ thin-film optical waveguide fabricated by pulsed laser deposition
Applied Physics Letters **69** (1), 10–12 (1996).

[Gme74] H. Bergmann
Gmelin Handbuch der Anorganischen Chemie - Seltenerdelemente, Teil C1
Springer-Verlag, 8th edition (1974).

[Gra98] A. J. McGrath, J. Munch, G. Smith and P. Veitch
Injection-seeded, single-frequency, Q-switched erbium:glass laser for remote sensing
Applied Optics **37** (24), 5706–5709 (1998).

[Gri08] C. Grivas and R. W. Eason
Dielectric binary oxide films as waveguide laser media: a review
Journal of Physics: Condensed Matter **20**, 1–8 (2008).

[Gue07a] T. Gün
Charakterisierung von mittels PLD hergestellten epitaktischen Sesquioxid- und YAG-Schichten
Diploma thesis, Universität Hamburg (2007).

[Gue07b] T. Gün, Y. Kuzminykh, K. Petermann and G. Huber
Epitaxial growth by pulsed laser deposition of Er-doped Sc_2O_3 films on sesquioxides monitored in situ by reflection high energy electron diffraction
Applied Physics Letters **91** (083103) (2007).

[Gue08] T. Gün, A. Kahn, B. İleri, K. Petermann and G. Huber
Two-dimensional growth of lattice matched Nd-doped (Gd, Lu)$_2O_3$ *films on* Y_2O_3 *by pulsed laser deposition*
Applied Physics Letters **93** (053108) (2008).

[Guy98] S. Guy et al.
High-Inversion Densities in Nd:YAG: Upconversion and Bleaching
IEEE Journal of Quantum Electronics **34** (5), 900–909 (1998).

[Han07] N.-O. Hansen
Mikroskopische und strukturelle Eigenschaften Selten-Erd-dotierter Sesquioxid-PLD-Schichten
Diploma thesis, Universität Hamburg (2007).

[Hei05] Z. K. Heiba, L. Arda and Y. S. Hascicek
Structure and microstructure characterization of the mixed sesquioxides $(Gd_{1-x}Yb_x)_2O_3$ *and* $(Gd_{1-x}Ho_x)_2O_3$ *prepared by sol–gel process*
Journal of Applied Crystallography **38**, 306–310 (2005).

[Hei09] S. Heinrich
Herstellung und Lasereigenschaften von epitaktisch gewachsenen Seltenerd-dotierten Sesquioxid-Wellenleitern
Diploma thesis, Universität Hamburg (2009).

[Hen89] B. Henderson and G. F. Imbusch
Optical Spectroscopy of Inorganic Solids
Clarendon Press, Oxford, first edition (1989).

[Hen94] M. Henzler and W. Göpel
Oberflächenphysik des Festkörpers
Teubner-Studienbücher, second edition (1994).

[Hoe93] T. H. Hoekstra, P. V. Lambeck, H. Albers and T. J. A. Popma
Sputter-deposited erbium-doped Y_2O_3 *active optical waveguides*
Electronics Letters **29**, 581–583 (1993).

[Hoe94] T. Hoekstra
Erbium-Doped Y_2O_3 *Integrated Optical Amplifiers*
Ph.D. thesis, University of Twente (1994).

[Hol98] C. Holtman
Integration and applications of III-V semiconductor optical amplifiers
Optical Communication, 24th European Conference on Optical Communication **1**, 499–500 (1998).

[Hos64] R. H. Hoskins and B. H. Soffer
Stimulated emission from $Y_2O_3{:}Nd^{3+}$
Applied Physics Letters **4** (1), 22–23 (1964).

[Hun02] R. G. Hunsperger
Integrated Optics - Theory and Technology
Springer Verlag, fifth edition (2002).

[IEE03] American National Standards Institute
IEEE Standard for Letter Designations for Radar-Frequency Bands
IEEE Std 521^{TM}-2002 (2003).

[Ile08] B. İleri
Lattice Matching of Epitaxial, Rare-Earth-doped, Dielectric PLD-Films
Ph.D. thesis, Universität Hamburg (2008).

[Ina76] K. Inada
A new graphical method relating to optical fiber attenuation
Optics Communications **19** (3), 437–439 (1976).

[Jac94] T. J. Jackson and S. B. Palmer
Oxide superconductor and magnetic metal film deposition by pulsed laser ablation: a review
Journal of Physics D: Applied Physics **27**, 1581–1594 (1994).

[Jer05] M. Jerman, Z. Qiao and D. Mergel
Refractive index of thin films of SiO_2, ZrO_2, and HfO_2 as a function of the films' mass density
Applied Optics **44** (15), 3006–3012 (2005).

[Kai02] N. Kaiser
Review of the fundamentals of thin-film growth
Applied Optics **41** (16), 3053–3060 (2002).

[Kam90] A. A. Kaminskii
Laser Crystals - Their Physics and Properties
Springer Verlag, second edition (1990).

[Kar91] W. Karthe and R. Müller
Integrierte Optik
Akademische Verlagsgesellschaft Geest & Portig K.-G, Leipzig, first edition (1991).

[Kec72] D. B. Keck and A. R. Tynes
Spectral Response of Low-Loss Optical Waveguides
Applied Optics **11** (7), 1502–1506 (1972).

[Kei97] B. Keiper
Ionengestützte Laserpulsabscheidung von Oxidschichten für optische Anwendungen
Ph.D. thesis, Technische Universität Chemnitz (1997).

[Kor82] U. Koren et al.
Recent Developments in Monolithic Integration of InGaAsP/InP Optoelectronic Devices
IEEE Journal of Quantum Electronics **QE-18** (10), 1653–1662 (1982).

[Kor89] G. Koren, A. Gupta, R. J. Baseman, M. I. Lutwyche and R. B. Laibowitz
Laser wavelength dependent properties of $YBa_2Cu_3O_{7-\delta}$ thin films deposited by laser ablation
Applied Physics Letters **55**, 2450–2452 (1989).

[Kos99] G. Koster, G. J. H. M. Rijnders, D. H. A. Blank and H. Rogalla
Imposed layer-by-layer growth by pulsed laser interval deposition
Applied Physics Letters **74** (24), 3729–3731 (1999).

[Kue07] H. Kühn, S. T. Fredrich-Thornton, C. Kränkel, R. Peters and K. Petermann
Model for the calculation of radiation trapping and description of the pinhole method
Optics Letters **32** (13), 1908–1910 (2007).

[Kue09a] H. Kühn
Ytterbium-dotierte einkristalline Sesquioxid-Wellenleiterlaser (submitted)
Ph.D. thesis, Universität Hamburg (2009).

[Kue09b] H. Kühn, M. Fechner, A. Kahn, H. Scheife and G. Huber
Energy transfer in crystalline Er^{3+},Yb^3+:Sc_2O_3
Optical Materials **31** (11), 1636–1639 (2009).

[Kue09c] H. Kühn, S. Heinrich, A. Kahn, K. Petermann, J. D. B. Bradley, K. Wörhoff, M. Pollnau and G. Huber
Monocrystalline Yb^{3+}:$(Gd, Lu)_2O_3$ channel waveguide laser at 976.8 nm
Optics Letters **34** (18), 2718–2720 (2009).

[Kuz06] Y. Kuzminykh
Crystalline, Rare-Earth-Doped Sesquioxide and YAG PLD-Films
Ph.D. thesis, Universität Hamburg (2006).

[Lal89] E. Lallier et al.
Laser oscillation of single-mode channel waveguide in $Nd:MgO:LiNbO_3$
Electronics Letters **25** (22), 1491–1492 (1989).

[Lan99] J. Lančok et al.
Structural and optical characterisation of Nd doped $YAlO_3$ films deposited on sapphire substrate by pulsed laser deposition
Thin Solid Films **346**, 284–289 (1999).

[Lee91] D. Lee, S. J. Barnett, A. D. Pitt, M. R. Houlton and G. W. Smith
Characterization of alloy composition in $Ga_{1-x}Al_xAs/GaAs$ structures: comparison of photovoltage, X-ray, SIMS and RHEED techniques
Applied Surface Science **50**, 428–433 (1991).

[Leh86] H. W. Lehmann
Dry etching: concepts, methods and applications in *The physics and fabrication of microstructures and microdevices*, Springer Verlag (1986).

[Liu07] L. Liu and X. Chen
Energy levels, fluorescence lifetime and Judd-Ofelt parameters of Eu^{3+} *in* Gd_2O_3 *nanocrystals*
Nanotechnology **18**, 1–8 (2007).

[Lut90] L. Lutterotti and P. Scardi
Simultaneous Structure and Size-Strain Refinement by the Rietveld Method
Journal of Applied Crystallography **23**, 246–252 (1990).

[Mac07] J. I. Mackenzie
Dielectric Solid-State Planar Waveguide Lasers: A Review
IEEE Journal of Selected Topics in Quantum Electronics **13** (3), 626–637 (2007).

[Mar83] P. J. Martin, H. A. Macleod, R. P. Netterfield, C. G. Pacey and W. G. Sainty
Ion-beam-assisted deposition of thin films
Applied Optics **22** (1), 178–184 (1983).

[McC64] D. E. McCumber
Einstein Relations Connecting Broadband Emission and Absorption Spectra
Physical Review **136** (4A), A954–A957 (1964).

[McC83] L. McCaughan and E. J. Murphy
Influence of Temperature and Initial Titanium Dimensions on Fiber-Ti:$LiNbO_3$ *Waveguide Insertion Loss at* $\lambda = 1.3\,\mu m$
IEEE Journal of Quantum Electronics **QE-19** (2), 131–136 (1983).

[McD66] N. T. McDevitt and A. D. Davidson
Infrared Lattice Spectra of Cubic Rare Earth Oxides in the Region 700 to 50 cm^{-1}
Journal of the Optical Society of America **56** (5), 636–638 (1966).

[Mer07] L. D. Merkle, N. Ter-Gabrielyan and M. Dubinskii
Cross Sections for Room and Low Temperature Operation of Er-Doped Sesquioxide Lasers
Conference on Lasers and Electro-Optics/Quantum Electronics and Laser Science Conference and Photonic Applications Systems Technologies 2007 Technical Digest (Optical Society of America, Washington, DC, 2007), paper CThDD1.

[Mie08] G. Mie
Beiträge zur Optik trüber Medien, speziell kolloidaler Metallösungen
Annalen der Physik **4** (25), 377–445.

[Mil69] S. E. Miller
Integrated optics: an introduction
Bell System Technical Journal **48** (7), 2059–2069 (1969).

[Mix99] E. Mix
Kristallzüchtung, Spektroskopie und Lasereigenschaften Yb-dotierter Sesquioxide
Ph.D. thesis, Universität Hamburg (1999).

[Moe97] P. E.-A. Möbert, E. Heumann, G. Huber and B. H. T. Chai
Green Er^{3+}:$YLiF_4$ upconversion laser at 551 nm with Yb^{3+} codoping: a novel pumping scheme
Optics Letters **22** (18), 1412–1414 (1997).

[Oka83] Y. Okamura, S. Yoshinaka and S. Yamamoto
Measuring mode propagation losses of integrated optical waveguides: a simple method
Applied Optics **22** (23), 3892–3894 (1983).

[Oka85] Y. Okamura, S. Sato and S. Yamamoto
A simple method of measuring propagation properties of integrated optical waveguides: an improvement
Applied Optics **24** (1), 57–60 (1985).

[Oka00] K. Okamoto
Fundamentals of Optical Waveguides
Academic Press (2000).

[Pau30] L. Pauling and M. D. Shappell
The Crystal Structure of Bixbyite and the C-Modification of the Sesquioxides
Zeitschrift für Kristallographie **75**, 128–142 (1930).

[Pet91] F. H. Peters and D. T. Cassidy
Strain and scattering related spectral output of 1.3-μm InGaAsP semiconductor diode lasers
Applied Optics **30** (9), 1036–1041 (1991).

[Pet98] V. Peters
Spektroskopie und Lasereigenschaften erbium- und praseodymdotierter hochschmelzender Oxide
Diploma thesis, Universität Hamburg (1998).

[Pet07] R. Peters, C. Kränkel, K. Petermann and G. Huber
Broadly tunable high-power Yb:Lu_2O_3 thin disk laser with 80% slope efficiency
Optics Express **15** (11), 7075–7082 (2007).

[Pet08] R. Peters, C. Kränkel, K. Petermann and G. Huber
Crystal growth by the heat exchanger method, spectroscopic characterization and laser operation of high-purity Yb:Lu_2O_3
Journal of Crystal Growth **310** (7-9), 1934–1938 (2008).

[Pet09] R. Peters
Ytterbium-dotierte Sesquioxide als hocheffiziente Lasermaterialien
Ph.D. thesis, Universität Hamburg (2009).

[Pin73] D. A. Pinnow, T. C. Rich, F. W. Ostermayer and M. DiDomenico
Fundamental optical attenuation limits in the liquid and glassy state with application to fiber optical waveguide materials
Applied Physics Letters **22** (10), 527–529 (1973).

[Pol96] M. Pollnau
Population Mechanisms in Erbium-Doped Solid-State Lasers
Ph.D. thesis, Universität Hamburg (1996).

[Pol07] M. Pollnau et al.
Ti:Sapphire waveguide lasers
Laser Physics Letters **4** (8), 560–571 (2007).

[Rab04] L. Rabisch
Ultradünne, Eu-dotierte, thermisch aufgedampfte Sesquioxid-Schichten auf α-Al_2O_3-Substraten
Ph.D. thesis, Universität Hamburg (2004).

[Raj02] R. Ramaswami
Optical fiber communication: from transmission to networking
IEEE Communications Magazine, 50th Anniversary Commemorative Issue (2002).

[Reg85] R. Regener and W. Sohler
Loss in Low-Finesse Ti:$LiNbO_3$ Optical Waveguide Resonators
Applied Physics B **36**, 143–147 (1985).

[Ric69] D. K. Rice and L. G. DeShazer
Spectral Broadening of Europium Ions in Glass
Phys. Rev. **186** (2), 387–392 (1969).

[Rij97] G. J. H. M. Rijnders, G. Koster, D. H. A. Blank and H. Rogalla
In situ monitoring during pulsed laser deposition of complex oxides using reflection high energy electron diffraction under high oxygen pressure
Applied Physics Letters **70** (14), 1888–1890 (1997).

[Sae93a] K. L. Saenger
Pulsed Laser Deposition (Part I) - A Review of Process Characteristics and Capabilities
Processing of Advanced Materials **2**, 1–24 (1993).

[Sae93b] K. L. Saenger
Pulsed Laser Deposition (Part II) - A Review of Process Mechanisms
Processing of Advanced Materials **3**, 63–82 (1993).

[Sal91] B. E. A. Saleh and M. C. Teich
Fundamentals of Photonics
Wiley & Sons, Inc. (1991).

[Sch01] H. Scheife
Faseroptischer Verstärker in Selten-Erd-dotiertem Fluoridglas für den sichtbaren Spektralbereich
Ph.D. thesis, Universität Hamburg (2001).

[Sch09] K. Schenk
Untersuchung der Streuverluste und Lasereigenschaften von $Yb{:}Y_2O_3$
Diploma thesis, Universität Hamburg (2009).

[She06] D. Y. Shen, J. K. Sahu and W. A. Clarkson
Highly efficient in-band pumped Er:YAG laser with 60 W of output at 1645 nm
Optics Letters **31** (6), 754–756 (2006).

[Shi90] W. Q. Shi, M. Bass and M. Birnbaum
Effects of energy transfer among Er^{3+} *ions on the fluorescence decay and lasing properties of heavily doped* $Er{:}Y_3Al_5O_{12}$
Journal of the Optical Society of America B **7** (8), 1456–1462 (1990).

[Sie86] A. E. Siegman
Lasers
University Science Books (1986).

[Smi65] H. M. Smith and A. F. Turner
Vacuum Deposited Thin Films Using a Ruby Laser
Applied Optics **4** (1), 147 (1965).

[Sta72] R. D. Standley, W. M. Gibson and J. W. Rodgers
Properties of Ion-Bombarded Fused Quartz for Integrated Optics
Applied Optics **11** (6), 1313–1316 (1972).

[Sto78] J. Stone and C. A. Burrus
$Nd{:}Y_2O_3$ *single-crystal fiber laser: Room-temperature cw operation at 1.07- and 1.35-*μ*m wavelength*
Journal of Applied Physics **49** (4), 2281–2287 (1978).

[Sve98] O. Svelto
Principles of Lasers
Plenum Press, New York, fourth edition (1998).

[Tit93] G. Tittelbach, B. Richter and W. Karthe
Comparison of three transmission methods for integrated optical waveguide propagation loss measurement
Pure Applied Optics **2**, 683–700 (1993).

[Ulr73] R. Ulrich and R. Torge
Measurement of Thin Film Parameters with a Prism Coupler
Applied Optics **12** (12), 2901–2908 (1973).

[Veg21] L. Vegard
Die Konstitution der Mischkristalle und die Raumfüllung der Atome
Zeitschrift für Physik **5**, 17–26 (1921).

[Vie74] D. Viechnicki and F. Schmid
Crystal Growth using the Heat Exchanger Method (HEM)
Journal of Crystal Growth **26**, 162–164 (1974).

[Web68] M. J. Weber
Radiative and Multiphonon Relaxation of Rare-Earth Ions in Y_2O_3
Physical Review **171** (2), 283–291 (1968).

[Web73] H. P. Weber, F. A. Dunn and W. N. Leibolt
Loss Measurements in Thin-Film Optical Waveguides
Applied Optics **12** (4), 755–757 (1973).

[Web74] H. P. Weber, P. F. Liao and B. C. Tofield
Emission Cross Section and Fluorescence Efficiency of Nd-pentaphosphate
IEEE Journal of Quantum Electronics **QE-10** (7), 563–567 (1974).

[Web82] M. J. Weber
Handbook of Laser Science and Technology, Volume 1 - Lasers and Masers
CRC Press, Inc. (1982).

[Wei98] M. Weisser, F. Thoma, B. Menges, U. Langbein and S. Mittler-Neher
Fluorescence in ion exchanged BK7 glass slab waveguides and its use for scattering free loss measurements
Optics Communications **153**, 27–31 (1998).

[Yar76] A. Yariv
Introduction to Optical Electronics
Holt, Rinehart and Winston, second edition (1976).

[Yos95] M. Yoshimoto et al.
Atomic-scale formation of ultrasmooth surfaces on sapphire substrates for high-quality thin-film fabrication
Applied Physics Letters **67** (18), 2615–2617 (1995).

[Zer71] F. Zernike, J. W. Douglas and D. R. Olson
Transmission Measurements in Optical Waveguides Produced by Proton Irradiation of Fused Silica
Journal of the Optical Society of America **61**, 678 (1971).

List of Publications

Publications in Journals

- Y. Kuzminykh, A. Kahn, and G. Huber, *"Nd^{3+} doped Sc_2O_3 waveguiding film produced by pulsed laser deposition,"* Optical Materials **28**, 883-887 (2006)
- A. Kahn, Y. Kuzminykh, H. Scheife, and G. Huber, *"Nondestructive measurement of the propagation losses in active planar waveguides,"* Journal of the Optical Society of America B **24** (7), 1571-1574 (2007)
- T. Gün, A. Kahn, B. İleri, K. Petermann, and G. Huber, *"Two-dimensional growth of lattice matched Nd-doped $(Gd, Lu)_2O_3$ films on Y_2O_3 by pulsed laser deposition,"* Applied Physics Letters **93**, 053108 (2008)
- A. Kahn, H. Kühn, S. Heinrich, K. Petermann, J. D. B. Bradley, K. Wörhoff, M. Pollnau, Y. Kuzminykh, and G. Huber, *"Amplification in epitaxially grown Er:$(Gd, Lu)_2O_3$ waveguides for active integrated optical devices,"* Journal of the Optical Society of America B **25** (11), 1850-1853 (2008)
- A. Kahn, S. Heinrich, H. Kühn, K. Petermann, J. D. B. Bradley, K. Wörhoff, M. Pollnau, and G. Huber, *"Low threshold monocrystalline Nd:$(Gd, Lu)_2O_3$ channel waveguide laser,"* Optics Express **17** (6), 4412-4418 (2009)
- H. Kühn, M. Fechner, A. Kahn, H. Scheife, and G. Huber, *"Energy transfer in crystalline Er^{3+},Yb^{3+}:Sc_2O_3,"* Optical Materials **31** (11), 1636-1639 (2009)
- H. Kühn, S. Heinrich, A. Kahn, K. Petermann, J. D. B. Bradley, K. Wörhoff, M. Pollnau, and G. Huber, *"Monocrystalline Yb^{3+}:$(Gd, Lu)_2O_3$ channel waveguide laser at 976.8 nm,"* Optics Letters **34** (18), 2718-2720 (2009)

International Conference Contributions

Oral Presentations

- Y. Kuzminykh, A. Kahn, and G. Huber, *"Nd^{3+} doped Sc_2O_3 waveguiding film produced by pulsed laser deposition,"* EMRS Spring Meeting, Strasbourg, May 31 – June 3, 2005, paper C-IV02/C-VI02
- M. Fechner, A. Kahn, K. Petermann, H. Scheife, and G. Huber, *"Continuous-wave laser action of an Er:Sc_2O_3 bulk crystal at 1.58 μm,"* CLEO/Europe–IQEC, München, June 10 – 15, 2007, paper CA8-5-WED

- M. Fechner, R. Peters, A. Kahn, K. Petermann, E. Heumann, and G. Huber, *"Efficient in-band-pumped Er:Sc_2O_3-laser at 1.58 μm,"* CLEO/QELS, San Jose, May 4 – 9, 2008, paper CTuAA3
- A. Kahn, T. Gün, B. İleri, H. Kühn, K. Petermann, J. D. B. Bradley, F. Ay, K. Wörhoff, M. Pollnau, Y. Luo, P. Hoffmann, and G. Huber, *"Mono-crystalline Rare Earth Doped (Gd, Lu)$_2O_3$ Waveguiding Films Produced by Pulsed Laser Deposition and Structured by Reactive Ion Etching,"* CLEO/QELS, San Jose, May 4 – 9, 2008, paper CTuS1
- A. Kahn, H. Kühn, S. Heinrich, T. Gün, F. Tellkamp, K. Petermann, J. D. B. Bradley, F. Ay, K. Wörhoff, M. Pollnau, Y. Kuzminykh, Y. Luo, P. Hoffmann, and G. Huber, *"In-band Pumping of Epitaxially Grown Er:(Gd, Lu)$_2O_3$ Waveguides for Active Integrated Optical Devices,"* Europhoton Conference, Paris, August 31 – September 5, 2008, paper THoD.2
- H. Kühn, A. Kahn, S. Heinrich, K. Petermann, and G. Huber, *"Crystalline Sesquioxide Channel Waveguide Lasers Produced by Pulsed Laser Deposition,"* RFGLS, Nizhny Novgorod, May 17 – 22, 2009
- A. Kahn, H. Kühn, S. Heinrich, K. Petermann, G. Huber, J. D. B. Bradley, K. Wörhoff, and M. Pollnau, *"Low Threshold Channel Waveguide Laser in a Monocrystalline Nd:(Gd, Lu)$_2O_3$ Film,"* CLEO/QELS/IQEC, Baltimore, May 31 – June 5, 2009, paper CTuP7
- L. Agazzi, J. D. B. Bradley, F. Ay, A. Kahn, H. Scheife, G. Huber, R. M. de Ridder, K. Wörhoff, and M. Pollnau,*"Energy Migration Governs Upconversion Losses in Er^{3+}-doped Integrated Amplifiers,"* CLEO/Europe–EQEC, München, June 14 – 19, 2009, paper CE.1.3-MON
- N. A. Tolstik, N. V. Kuleshov, S. Heinrich, A. Kahn, G. Huber, E. A. Volkova, and N. I. Leonyuk, *"Er,Yb:$YAl_3(BO_3)_4$ crystalline layers grown by liquid-phase epitaxy,"* CLEO/Europe–EQEC, München, June 14 – 19, 2009, paper CE.4.3-TUE

Poster Presentations

- Y. Kuzminykh, A. Kahn, and G. Huber, *"Nd^{3+} doped Sc_2O_3 waveguiding film produced by pulsed laser deposition,"* EMRS Spring Meeting, Strasbourg, May 31 – June 3, 2005, paper C/PII.26
- A. Kahn, Y. Kuzminykh, H. Scheife, and G. Huber, *"Non-destructive scattering loss measurement in active planar waveguides,"* Europhoton Conference, Pisa, September 10 – 15, 2006, paper TuC6
- J. D. B. Bradley, D. Geskus, T. Blauwendraat, F. Ay, K. Wörhoff, A. Kahn, H. Scheife, K. Petermann, G. Huber, and M. Pollnau, *"Growth, Micro-Structuring, Spectroscopy, and Optical Gain in As-Deposited Al_2O_3:Er Waveguides,"* ASSP, Nara, January 27 – 30, 2008, paper WB10

- K. Wörhoff, J. D. B. Bradley, L. Agazzi, D. Geskus, F. Ay, A. Kahn, H. Scheife, K. Petermann, G. Huber, and M. Pollnau, *"Energy-transfer upconversion in* Al_2O_3*:*Er^{3+} *thin layers,"* IWASOM08, Gdansk, July 13 – 17, 2008, paper 6-O-3
- H. Kühn, M. Fechner, A. Kahn, H. Scheife, and G. Huber, *"Energy transfer processes in crystalline* Er^{3+}*,*Yb^{3+}*:*Sc_2O_3*,"* CLEO/Europe–EQEC, München, June 14 – 19, 2009, paper CE.P.14-MON

National Conference Contributions

Oral Presentations

- Y. Kuzminykh, B. Neubert, S. Bär, A. Kahn, and H. Scheife, *"Optisch aktive Sesquioxidwellenleiter,"* DPG-Frühjahrstagung, Berlin, March 4 – 9, 2005, paper Q66.6
- A. Kahn, Y. Kuzminykh, H. Scheife, and G. Huber, "Verlustmessung an Nd^{3+}-dotierten planaren Wellenleitern," DPG-Frühjahrstagung, Frankfurt, March 13 – 17, 2006, paper Q11.2
- A. Kahn, M. Fechner, N.-O. Hansen, H. Kühn, Y. Kuzminykh, H. Scheife, and G. Huber, *"Spektroskopische Charakterisierung von* Er^{3+}*- und* Er^{3+}*,*Yb^{3+}*-dotierten Sesquioxidschichten für Laseranwendungen,"* DPG-Frühjahrstagung, Düsseldorf, March 19 – 23, 2007, paper Q8.1
- M. Fechner, A. Kahn, H. Scheife, K. Petermann, and G. Huber, *"Lasertätigkeit von* Er^{3+}*:*Sc_2O_3 *bei 1,58 µm Wellenlänge,"* DPG-Frühjahrstagung, Düsseldorf, March 19 – 23, 2007, paper Q3.7
- H. Kühn, M. Fechner, A. Kahn, H. Scheife, and G. Huber, *"Untersuchung von Energietransferprozessen in* Er^{3+}*,*Yb^{3+}*:*Sc_2O_3*,"* DPG-Frühjahrstagung, Hamburg, March 2 – 6, 2009, paper Q8.1
- S. Heinrich, A. Kahn, H. Kühn, K. Petermann, and G. Huber, *"Optische Verstärkung in einkristallinen Er:(Gd, Lu)*$_2O_3$ *Rippenwellenleitern,"* DPG-Frühjahrstagung, Hamburg, March 2 – 6, 2009, paper Q8.5

Poster Presentations

- A. Kahn, B. Neubert, Y. Kuzminykh, L. Rabisch, H. Scheife, and G. Huber, *"Planar garnet and sesquioxide waveguide structures,"* 15. Norddeutscher Lasertag, Hamburg, December 8, 2004
- A. Kahn, Y. Kuzminykh, H. Scheife, and G. Huber, *"Non-destructive scattering loss measurement in active planar waveguides,"* 16. Norddeutscher Lasertag, Hannover, December 6, 2006
- N.-O. Hansen, M. Fechner, H. Kühn, A. Kahn, Y. Kuzminykh, H. Scheife, and G. Huber, *"Kristalline Er- und Er,Yb-dotierte PLD-Sesquioxidschichten,"* 16. Norddeutscher Lasertag, Hannover, December 6, 2006

- S. Heinrich, A. Kahn, H. Kühn, K. Petermann, and G. Huber, *"Verstärkungsmessung in einkristallinen Er:(Gd, Lu)$_2$O$_3$ Streifenwellenleitern,"* 17. Norddeutscher Lasertag, Hannover, December 10, 2008

Seminars and Workshops

- A. Kahn, *"Verlustmessung und Charakterisierung von Nd^{3+}-dotierten planaren Wellenleitern,"* Seminar über Festkörperlaser, Hamburg, November, 2005
- A. Kahn and T. Gün, *"Herstellung und Charakterisierung heteroepitaktischer PLD-Schichten zur Realisierung von Wellenleiterlasern,"* Arbeitskreis-Tagung *Kristalle für Laser und nichtlineare Optik*, Osnabrück, September 29 – 30, 2008
- A. Kahn, *"Sesquioxide Waveguide Lasers I,"* LAS-F, Lintrup, May 5 – 7, 2009
- A. Kahn, *"Herstellung und Charakterisierung von einkristallinen Sesquioxid-Wellenleiterlasern,"* Seminar über Festkörperlaser, Hamburg, October 21, 2009

Other Publications

- A. Kahn, *"Verlustmessung an Nd^{3+} dotierten planaren Wellenleitern und deren Charakterisierung für Laseranwendungen,"* Diploma thesis, November, 2005

Acknowledgement

This thesis is the result of more than three years of research at the *Institute of Laser Physics* in Hamburg. It would not have been possible without the assistance and support of many people.

First, I would like to thank my doctoral thesis supervisor Prof. Dr. Günter Huber for admitting me to the group *Festkörperlaser* and for allowing me to work on such an interesting and diverse research subject. Furthermore, I thank him for his advice, the many scientific discussions, and for dealing with all those project reports.

I also thank Dr. Klaus Petermann for his significant contribution to the organization of group affairs and for a first flying lesson as well as Dr. Hanno Scheife for his notable involvement in the project PI-OXIDE during the first years. Both of them have always been available for advice and extensive scientific discussions.

I would like to dedicate the sesquioxide waveguide laser to Prof. Dr. Ernst Heumann, who has been looking forward to its realization even longer than I have. I thank him for his encouragement after various setbacks in early waveguide laser experiments.

Many thanks to my teammates of the *gain and laser team* Henning Kühn and Sebastian Heinrich for the fruitful collaboration, and to Teoman Gün for his assistance with the RHEED measurements. I thank all of them for some great times inside and outside of the lab as well as during project and conference travels, and for many interesting conversations. Dr. Yury Kuzminykh has also been extremely helpful and a great company during his stay in Hamburg, on travels and during collaboration with the *Ecole Polytechnique Fédérale de Lausanne*. Furthermore, I thank Matthias Fechner and Nils-Owe Hansen for the excellent cooperation in the first project year.

There have been many technical problems, but none of them could withstand the quick and sometimes unorthodox solutions of Friedjof Tellkamp. He has been invaluable, especially by maintaining and improving the PLD setup. Stephan Garbers has also been very helpful whenever quick fabrication or modification of mechanical equipment and high precision were required. Many thanks to both of them for being awesome colleagues and for some great times after work. Furthermore, I would like to thank Robert Fischer for maintaining the technical equipment of the institute and Silke Frömmig for taking care of the administrative work.

For proof-reading large parts or small pieces of this thesis, I thank Jörg Siebenmorgen, Dr. Klaus Petermann, Henning Kühn, Sebastian Heinrich, Teoman Gün, Rigo Peters, Ulrike Wolters, and Matthias Fechner. Furthermore, I thank Ulrike Wolters for the *in-situ* language assistance.

I really enjoyed the outstanding working atmosphere in the group. Thus, I would like to thank all co-workers, especially my current and former office-mates. Several of them have been participating in extremely successful cooperations concerning tea preparation.

There has been a lot of helpful collaboration with other research groups, institutes and companies. Therefore, I would like to express my gratitude to:

… Jonathan D. B. Bradley, Meidert Dijkstra, Dr. Feridun Ay, Dr. Kerstin Wörhoff, and Prof. Dr. Markus Pollnau of the *MESA+ Institute for Nanotechnology of the University of Twente* for structuring of the waveguiding films, sputtering of cover layers, measuring refractive indexes, and prism coupling experiments. I thank them for an extremely successful and close cooperation.

… Dr. Yun Luo, Dr. Yury Kuzminykh, and Dr. Patrik Hoffmann of the *Advanced Photonics Laboratory of the Ecole Polytechnique Fédérale de Lausanne* for their hospitality and for sharing their polishing experience with us. I would also like to thank them for assistance during the OLCR measurements, sputtering of a cover layer as well as for their company during and after frustrating nights and weekends of polishing.

… Dieter Barlösius for coating the waveguide end-facets with reflective mirrors as well as for his patience working without *ion assistance* and for pre-estimating the effects of humidity.

… Christian Krug, Michael Pfeifers, and Prof. Dr. Platte of the *Fachhochschule Wedel* for allowing regular use of their XRD setup.

… Claudia Hagemann and Manfred Spiwek of the *Hamburger Synchrotronstrahlungslabor* for the opportunity to use their lapping equipment.

… the company *Phoenix BV* for providing the project partners with the excellent software *FieldDesigner* free of charge.

I would like to thank Prof. Dr. D. Heitmann and Priv.-Doz. Dr. V. M. Baev for their time and effort as second assessors of this dissertation and my disputation, respectively.

Furthermore, I would like to express my gratitude to the *European Union* for funding within the specific targeted research project *Photonic Integrated Devices in Activated Amorphous and Crystalline Oxides* (PI-OXIDE, contract number 017 501).

Last but not least, I thank my parents Ulrich and Margarete Kahn for all their commitment and support.

Index